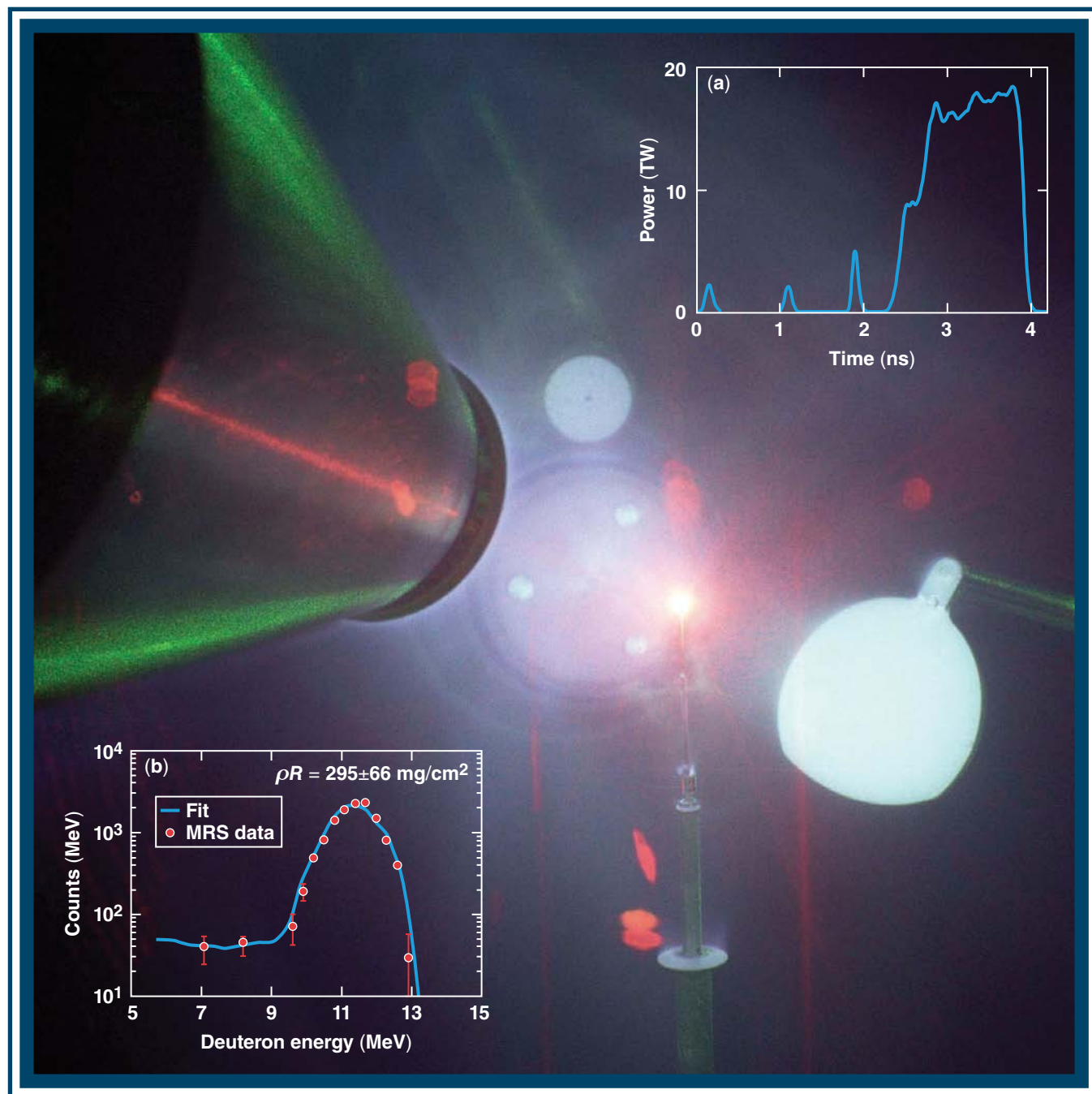


# LLE Review

## Quarterly Report



## About the Cover:

Cryogenic deuterium-tritium capsules have been imploded on the OMEGA Laser System, creating the highest-ever areal densities ( $\rho R \sim 300 \text{ mg/cm}^2$ ) in a cryogenic inertial confinement fusion implosion (see p. 1). The photograph seen on the cover shows the cryogenic target that yielded the highest areal density to date as it was imploded in the OMEGA target chamber. This high areal density was achieved using a triple-picket laser pulse [shown in inset (a)] to drive a stalk-mounted target. The areal density was measured by the magnetic recoil spectrometer (MRS), which is reported on in this issue (p. 33). The white feature to the right of center is the front foil of the MRS diagnostic device. The plot in inset (b) presents raw data collected from the MRS for this implosion. The peak areal density was inferred from this data. The demonstration of high areal density is critical to ignition experiments on the National Ignition Facility.



The photo at the left shows a shadowgraph of the cryogenic target imploded in the cover photo. Analysis of the circular bright band in the shadowgraph provides a measure of the smoothness of the inner surface of the cryogenic-DT layer. Characterization of this layer smoothness is crucial for understanding the hydrodynamic stability of the implosion since target roughness can have a large effect on target performance. The inner surface roughness for this target was approximately  $2\text{-}\mu\text{m}$  root-mean-square in all modes.

This report was prepared as an account of work conducted by the Laboratory for Laser Energetics and sponsored by New York State Energy Research and Development Authority, the University of Rochester, the U.S. Department of Energy, and other agencies. Neither the above named sponsors, nor any of their employees, makes any warranty, expressed or implied, or assumes any legal liability or responsibility for the accuracy, completeness, or usefulness of any information, apparatus, product, or process disclosed, or represents that its use would not infringe privately owned rights. Reference herein to any specific commercial product, process, or service by trade name, mark, manufacturer, or otherwise, does not necessarily constitute or imply its endorsement, recommendation, or favoring by

the United States Government or any agency thereof or any other sponsor. Results reported in the LLE Review should not be taken as necessarily final results as they represent active research. The views and opinions of authors expressed herein do not necessarily state or reflect those of any of the above sponsoring entities.

The work described in this volume includes current research at the Laboratory for Laser Energetics, which is supported by New York State Energy Research and Development Authority, the University of Rochester, the U.S. Department of Energy Office of Inertial Confinement Fusion under Cooperative Agreement No. DE-FC52-08NA28302, and other agencies.

Printed in the United States of America

Available from

National Technical Information Services

U.S. Department of Commerce

5285 Port Royal Road

Springfield, VA 22161

Price codes: Printed Copy A04

Microfiche A01

For questions or comments, contact Kenneth S. Anderson, Editor, Laboratory for Laser Energetics, 250 East River Road, Rochester, NY 14623-1299, (585) 275-9352.

Worldwide-Web Home Page: <http://www.lle.rochester.edu/>

# LLE Review

## Quarterly Report



### Contents

In Brief .....	iii
Demonstration of the Highest Deuterium–Tritium Areal Density Using Triple-Picket Cryogenic Designs on OMEGA .....	1
High-Precision Measurements of the Equation of State of Hydrocarbons at 1 to 10 Mbar Using Laser-Driven Shock Waves .....	6
A Generalized Measurable Ignition Condition for Inertial Confinement Fusion .....	22
<i>In-Situ</i> Detection and Analysis of Laser-Induced Damage on a 1.5-m Multilayer-Dielectric Grating Compressor for High-Energy, Petawatt-Class Laser Systems .....	27
Probing High-Areal-Density ( $\rho R$ ) Cryogenic-DT Implosions Using Down-Scattered Neutron Spectra Measured by the Magnetic Recoil Spectrometer .....	33
Strong-Coupling and Degeneracy Effects in Inertial Confinement Fusion Implosions .....	44
Neutron-Induced Nucleation Inside Bubble Chambers Using Freon 115 as the Active Medium .....	50
Publications and Conference Presentations	



## In Brief

This volume of the LLE Review, covering October–December 2009, features “Demonstration of the Highest Deuterium–Tritium Areal Density Using Triple-Picket Cryogenic Designs on OMEGA” by V. N. Goncharov, T. C. Sangster, T. R. Boehly, S. X. Hu, I. V. Igumenshchev, F. J. Marshall, R. L. McCrory, D. D. Meyerhofer, P. B. Radha, W. Seka, S. Skupsky, and C. Stoeckl. This article (p. 1) reports the performance of triple-picket deuterium–tritium (DT) cryogenic target designs on the OMEGA Laser System. These designs allow for improved control of shock heating in low-adiabat inertial confinement fusion implosions. Areal densities up to 300 mg/cm<sup>2</sup>, the highest ever measured in cryogenic-DT implosions, are inferred in these experiments. Extension of these designs to ignition on the National Ignition Facility is presented.

Additional highlights of research presented in this issue include the following:

- M. A. Barrios, D. G. Hicks, T. R. Boehly, D. E. Fratanduono, and D. D. Meyerhofer (LLE) and J. H. Eggert, P. M. Celliers, and G. W. Collins (LLNL) present measurements of the equations of state (EOS) of polystyrene and polypropylene using laser-driven shock waves with pressures from 1 to 10 Mbar (p. 6). Precision data resulting from the use of  $\alpha$ -quartz as an impedance-matching (IM) standard tightly constrain the EOS of these hydrocarbons, even with the inclusion of systematic errors inherent to IM. The temperature at these high pressures was measured, which, combined with kinematic measurements, provides a complete shock EOS. Both hydrocarbons were observed to reach similar compressions and temperatures as a function of pressure. The materials were observed to transition from transparent insulators to reflecting conductors at pressures of 1 to 2 Mbar.
- P.-Y. Chang, R. Betti, K. S. Anderson, and R. Nora (LLE and FSC); R. L. McCrory (LLE); B. K. Spears, J. Edwards, and J. D. Lindl (LLNL); M. Fatenejad (University of Wisconsin, Madison); and D. Shvarts (Nuclear Research Center Negev) derive a multidimensional, measurable ignition condition for thermonuclear ignition of inertial confinement fusion capsules (p. 22). The ignition criterion accounts for the effects of implosion nonuniformities and depends on three measurable parameters: the neutron-averaged total areal density, the ion temperature, and the yield-over-clean (YOC = ratio of the measured neutron yield to the predicted one-dimensional yield). The YOC measures the implosion uniformity. The criterion can be approximated as  $\chi = \rho R_n^{\text{tot}} (T_n/4.7)^{2.1} \text{YOC}^\mu > 1$  (where  $\rho R$  is in g/cm<sup>2</sup>,  $T$  is in keV, and  $\mu \approx 0.47$  to 0.63) and can be used to assess the performance of cryogenic implosions on the NIF and OMEGA. The validity of this criterion is confirmed by a multicode simulation database. Cryogenic implosions on OMEGA have achieved  $\chi \sim 10^{-2}$ .
- J. Qiao, A. W. Schmid, L. J. Waxer, T. Nguyen, J. Bunkenburg, C. Kingsley, A. Kozlov, and D. Weiner describe a grating-inspection system and a damage-analysis method developed to measure *in-situ* laser-induced damage on a 1.5-m tiled-grating assembly of the OMEGA EP pulse compressor during a 15-ps, 2.2-kJ energy ramp (p. 27). The beam fluence at which significant damage growth occurred was determined. This is the first report on beam fluence versus laser-induced–damage growth of meter-sized multilayer-dielectric-diffraction gratings. This result was correlated to the damage-probability measurement conducted on a small grating sample and is consistent with the fluence corresponding to 100% damage probability.

- J. A. Frenje, D. T. Casey, C. K. Li, F. H. Séguin, and R. D. Petrasso (Plasma Science and Fusion Center, MIT); V. Yu Glebov, P. B. Radha, T. C. Sangster, and D. D. Meyerhofer (LLE); S. P. Hatchett, S. W. Haan, C. J. Cerjan, and O. L. Landen (LLNL); K. A. Fletcher (State University of New York at Geneseo); and R. J. Leeper (Sandia National Laboratories) probe high-areal-density ( $\rho R$ ) cryogenic-DT implosions using down-scattered neutron spectra measured with the magnetic recoil spectrometer (MRS) recently installed and commissioned on OMEGA (p. 33). The  $\rho R$  data obtained with the MRS have been essential for understanding how fuel assembly occurs and for guiding the cryogenic program at LLE to  $\rho R$  values up to  $\sim 300$  mg/cm<sup>2</sup>. Areal-density data obtained from the well-established charged-particle-spectrometry technique were used to authenticate the MRS data, and the  $\rho R$  values inferred from these two techniques are similar, indicating that the MRS technique provides high-fidelity  $\rho R$  data. Recent OMEGA MRS data and Monte Carlo simulations have shown that the MRS at the National Ignition Facility will meet most of the absolute and relative requirements for determining  $\rho R$ , ion temperature ( $T_i$ ), and neutron yield ( $Y_n$ ) in both low-yield, deuterium-lean, H-doped tritium-hydrogen-deuterium implosions and high-yield deuterium-tritium implosions.
- S. X. Hu, V. N. Goncharov, and S. Skupsky (LLE) and B. Militzer (University of California, Berkeley) derive a first-principles equation of state (FPEOS) table for deuterium using the path-integral Monte Carlo method (p. 44). Accurate knowledge about the equation of state (EOS) of deuterium is critical to inertial confinement fusion (ICF). Low-adiabat ICF implosions routinely access strongly coupled and degenerate plasma conditions. The FPEOS table covers typical ICF fuel conditions at densities ranging from 0.002 g/cm<sup>3</sup> to  $\sim 1600$  g/cm<sup>3</sup> and temperatures of 1.35 eV to 5.5 keV. Discrepancies in internal energy and pressure have been found in strongly coupled and degenerate regimes with respect to *SESAME* EOS. Hydrodynamics simulations of cryogenic ICF implosions using the FPEOS table have indicated significant differences in peak density, areal density ( $\rho R$ ), and neutron yield relative to *SESAME* simulations. The FPEOS simulations result in better agreement of compression  $\rho R$  with experiments.
- M. C. Ghilea, D. D. Meyerhofer, and T. C. Sangster present a theoretical model to describe the mechanism of bubble formation for Freon 115 as the active medium in a liquid bubble chamber (p. 50). Neutron imaging is used in inertial confinement fusion (ICF) experiments to measure the core symmetry of imploded targets. Liquid bubble chambers have the potential to obtain higher-resolution images of the targets for a shorter source-target distance than typical scintillator arrays. The bubble-formation model shows that the size of the critical radius for the nucleation process determines the mechanism of bubble formation and the sensitivity of the active medium for the 14.1-MeV incident neutrons resulting from ICF implosions. The bubble-growth mechanism is driven by the excitation of the medium electronic levels and not by electrons ejected from the medium's atoms as happens for the bubble chambers used to detect charged particles. The model accurately predicts the neutron-induced bubble density measured on OMEGA with liquid bubble chambers and gel detectors.

Kenneth S. Anderson  
*Editor*

# Demonstration of the Highest Deuterium–Tritium Areal Density Using Triple-Picket Cryogenic Designs on OMEGA

In inertial confinement fusion (ICF) implosions, a cryogenic shell of deuterium–tritium (DT) fuel is driven inward by means of direct or indirect laser illumination to achieve high compression and burn.<sup>1</sup> Fuel burn proceeds in two stages: First, a lower-density, higher-temperature ( $\sim 10$ -keV) hot spot is formed by PdV work of converging higher-density, lower-temperature shells. Calculations show that to initiate burn, the shell kinetic energy must exceed the threshold value,<sup>2</sup> which depends on the shell implosion velocity  $V_{\text{imp}}$  (peak mass-averaged shell velocity), the in-flight shell adiabat  $\alpha_{\text{if}}$  (ratio of shell pressure to the Fermi-degenerate pressure at the position in peak shell density), and the drive pressure  $p_{\text{d}}$ . Second, as burn propagates through the fuel, shell inertia provides sufficient confinement time to burn a significant fraction of the assembled fuel. This requires fuel areal densities ( $\rho R$ ) at peak compression in excess of  $\sim 0.9$  g/cm<sup>2</sup> (Ref. 1). The peak areal density in a direct-drive implosion depends mainly on  $\alpha_{\text{if}}$  and laser energy  $E_{\text{L}}$  (Ref. 3):

$$\max(\rho R)_{\text{g/cm}^2} = \frac{2.6 E_{\text{L,MJ}}^{1/3}}{\alpha_{\text{if}}^{0.54}}. \quad (1)$$

Therefore, to burn a sufficient fraction of the fuel, the shell adiabat must be  $\alpha_{\text{if}} \leq 7 E_{\text{L,MJ}}^{0.6}$ . While hot-spot formation and burn-initiation physics require laser energy in excess of  $\sim 300$  kJ, which will be available on the National Ignition Facility (NIF),<sup>4</sup> implosions on the OMEGA laser<sup>5</sup> validate the ability of ignition designs to assemble cryogenic fuel with ignition-relevant implosion velocities ( $V_{\text{imp}} > 3 \times 10^7$  cm/s), maintaining the required fuel adiabat. A deviation of the adiabat from the designed value in an implosion can be inferred by comparing the measured and predicted values of  $\rho R$ . The areal density is determined by measuring spectral shapes of reaction products as they interact with the fuel.<sup>6,7</sup> This gives a value  $\langle \rho R \rangle_{\text{n}}$  averaged over reaction time history. The theoretical value of  $\langle \rho R \rangle_{\text{n}}$  has a similar dependence on  $\alpha_{\text{if}}$  and  $E_{\text{L}}$  as in Eq. (1) with a numerical factor of 1.7 instead of 2.6 (Ref. 3). Using this scaling, an OMEGA cryogenic-DT design, hydrodynamically equivalent to an  $\alpha_{\text{if}} = 2$  ignition design on the NIF, is predicted to achieve  $\langle \rho R \rangle_{\text{n}} \sim 300$  mg/cm<sup>2</sup> at a laser

energy  $\sim 25$  to  $30$  kJ and a laser absorption fraction of 60% to 70%, typical for OMEGA-scale targets. Reaching these areal densities on OMEGA, therefore, is a crucial step in validating predictive capabilities of hydrodynamic codes used to design ignition targets on the NIF.

The shell adiabat is determined by heating sources, including shock waves, radiation, and suprathermal electrons. Because of inaccuracies in the models used to design targets, experimental tuning is required to ensure that preheat is at an acceptable level. This article describes direct-drive target designs optimized for experimental shock timing to prevent adiabat degradation caused by excessive shock heating. This is accomplished by combining three intensity pickets with the main drive pulse [triple-picket (TP) design]. The main pulse in this case requires minimal shaping (an intensity step is introduced to control the strength of the main shock). Areal densities up to  $300$  mg/cm<sup>2</sup> are observed in cryogenic-DT implosions on OMEGA using the TP designs driven at peak intensities  $\sim 8 \times 10^{14}$  W/cm<sup>2</sup>.

One of the main challenges in designing hot-spot ignition implosions is to control the generation of strong shocks while accelerating the fuel shell to high implosion velocities. To avoid excessive shock heating, only few-Mbar shocks can be launched into cryogenic fuel at the beginning of an implosion. On the other hand, reaching  $V_{\text{imp}} > 3 \times 10^7$  cm/s without the Rayleigh–Taylor instability<sup>8</sup> disrupting the shell requires drive pressures  $p_{\text{d}}$  in excess of 100 Mbar since the shell’s in-flight aspect ratio  $A_{\text{in}}$  (ratio of shell radius  $R$  to shell thickness) is proportional to  $p_{\text{d}}^{-2/5}$  (Ref. 3) and shells with higher  $A_{\text{in}}$  are more susceptible to perturbation growth during the acceleration phase. Such a pressure increase from a few Mbar to 100 Mbar can be achieved either adiabatically [continuous-pulse (CP) design]<sup>9,10</sup> or by launching a sequence of shocks of increasing strength [multiple-shock (MS) designs].<sup>1,11</sup>

Early cryogenic spherical implosions on OMEGA used the CP designs.<sup>12–15</sup> Both 5- and 10- $\mu\text{m}$ -thick CD shells with cryogenic 95- $\mu\text{m}$ -thick D<sub>2</sub> and 80- $\mu\text{m}$ -thick DT layers were

used in these experiments. Areal densities close to the predicted values ( $\langle \rho R \rangle_n \sim 100$  to  $120$  mg/cm<sup>2</sup>) were achieved in implosions with 5- $\mu$ m shells driven at peak intensities below  $I_{\text{limit}} = 3 \times 10^{14}$  W/cm<sup>2</sup> ( $p_d \sim 50$  Mbar) and a laser pulse contrast ratio (CR) of less than 3.5. When 10- $\mu$ m shells were used,  $\langle \rho R \rangle_n$  values up to 200 mg/cm<sup>2</sup> (80% to 90% of the predicted areal densities) were measured for designs with  $I_{\text{limit}} = 5 \times 10^{14}$  W/cm<sup>2</sup> ( $p_d \sim 75$  Mbar) and a CR < 30 (Ref. 15). The implosion velocity was  $V_{\text{imp}} \simeq 2.2 \times 10^7$  cm/s. Increasing drive intensities above  $I_{\text{limit}}$  resulted in significant deviations of measured and predicted  $\langle \rho R \rangle_n$  (Ref. 14). Shock velocity measured in the CP designs using a velocity interferometry system for any reflector (VISAR)<sup>16</sup> revealed difficulty in reproducing an adiabatic compression wave predicted in simulations.<sup>14,17</sup> Since the effect of steepening a compression wave into a shock, not predicted in simulations, is exacerbated by increasing either peak drive intensity or laser pulse CR, it is impractical to experimentally tune the adiabat in the CP designs to ignition-relevant values.

Initial fuel compression prior to reaching peak drive intensity can be accurately controlled in the MS designs by launching a sequence of shocks using intensity pickets. Here we describe the main features of such designs. First, we assume that  $N$  shocks are launched by narrow pickets (picket duration is much shorter than shock transit time across the shell), and the main shock is launched and supported by the main pulse. Since pressure of an unsupported shock decays in time, the fuel adiabat decreases from the front to the back of the shell. Equation (1) needs to be modified in this case to reflect spatial variation in  $\alpha_{\text{if}}$ . The following supports using only the adiabat at the inner shell surface (“inner adiabat”  $\alpha_{\text{inn}}$ ) to determine areal density.<sup>3</sup> The maximum shell convergence during an implosion is limited by a rarefaction wave, created at the main shock-breakout time, with a tail propagating from the inner part of the shell toward the target center. Since material in a rarefaction moves at the local sound speed with respect to position of the peak shell density, the low-density tail is larger if the inner adiabat is higher. Later, as the main shock reflects from the center and begins interacting with the rarefaction, pressure at the target center starts to build up, initiating shell deceleration. Therefore, the larger the inner adiabat, the larger the rarefaction region, causing the main shell to decelerate farther from the center, thereby reducing the final shell convergence and areal density.

Since the adiabat is proportional to pressure over density to the 5/3rd power, shocks launched by the pickets must raise the inner shell density to a value sufficient to keep the main

shock with  $p_d \sim 100$  Mbar from increasing the inner adiabat above the required value. To maximize this compression, all shocks must coalesce nearly simultaneously in the vapor region, soon after they break out of the shell. This relates the picket amplitudes and timing. Using the adiabat relation with pressure and density  $\rho$  in DT fuel,  $\alpha \simeq p(\text{Mbar})/2.16 \rho^{5/3}$ , the required inner shell compression after the main shock can be written as  $\rho_{\text{main}}/\rho_0 \simeq 40[(p_d/100 \text{ Mbar})/\alpha_{\text{inn}}]^{3/5}$ , where  $\rho_0 = 0.25$  g/cm<sup>3</sup> is the initial shell density. The density at the first shock front is compressed by a factor of  $\sim 4$  if shock pressure  $p_1$  stays above  $\sim 1$  Mbar. Maximizing the density compression by the remaining  $N$  shocks ( $N-1$  shocks from pickets and the main shock) leads, with the help of Hugoniot relations,<sup>18</sup> to a condition on shock-pressure ratio as the shocks reach the inner surface,  $p_{i+1} = p_i(p_d/p_1)^{1/N}$ , where  $i = 1, \dots, N$ . The inner adiabat in this case is

$$\alpha_{\text{inn}} = 46.3 \left( \frac{p_d}{100 \text{ Mbar}} \right) \left[ \frac{(p_d/p_1)^{1/N} + 4}{4(p_d/p_1)^{1/N} + 1} \right]^{5N/3}. \quad (2)$$

Because of radiation preheat and additional heating caused by a secondary compression wave formed at the beginning of shell acceleration, the in-flight adiabat used in Eq. (1) is higher than  $\alpha_{\text{inn}}$  predicted by Eq. (1). In general, for an optimized multiple-picket design, an effective  $\alpha_{\text{inn}}$  is larger by a factor of 2 to 2.5. Therefore, a high-yield, direct-drive NIF design requires that the number  $N$  of pickets be determined by setting  $\alpha_{\text{inn}} \simeq 1$  (which is equivalent to an  $\alpha \simeq 2.5$  CP design) in Eq. (2). This gives a relation between  $N$  and  $p_d$ , which can be approximated by  $p_d(\text{Mbar}) \simeq 6.5 N e^{0.78 N}$ . For  $p_d \sim 100$  Mbar, this gives  $N = 3$ , and pressures of the first three shocks as they break out of the shell are 1, 4.6, and 21 Mbar, respectively.

Next, a simple model is used to gain insight into the shock evolution in a multiple-picket design. A shock wave traveling along the  $x$  axis with a velocity  $U_{\text{sh}}$  is assumed to be strong enough that the flow velocity ahead of the shock can be neglected with respect to post-shock velocity in the laboratory frame of reference. Using the ideal-gas equation-of-state model, the mass density in this case increases by a factor of 4 across the shock front. Gradients in the flow created by unsupported shocks lead to PdV work on a fluid element,  $d_t p \equiv \partial_t p + v \partial_x p = -(5/3)p \partial_x v$ . The spatial gradient in velocity can be expressed in terms of pressure gradient and acceleration in the shock-front frame using Bernoulli’s relation  $v \partial_x v + \partial_x p / \rho = -d_t U_{\text{sh}} - \partial_t v$ . In the strong-shock limit,  $v = -U_{\text{sh}}/4$  and  $U_{\text{sh}} = \sqrt{(4/3)p_{\text{sh}}/\rho_0}$ , leading to  $d_t(p_{\text{sh}} U_{\text{sh}}^5) = -U_{\text{sh}}^6 (\partial_x p)_{\text{sh}}$ , where  $p_{\text{sh}}$  is shock pressure and  $\rho_0$  is density ahead of the shock. This equation can

be simplified by introducing a mass coordinate,  $dm = \rho dx$ , and replacing time with the mass  $m_{\text{sh}}$  overtaken by the shock,  $dm_{\text{sh}} = \rho U_{\text{sh}} dt$ . At the shock front, this gives

$$\frac{d \ln(p_{\text{sh}} U_{\text{sh}}^5)}{dm_{\text{sh}}} = -4 \left( \frac{\partial \ln p}{\partial m} \right)_{\text{sh}}. \quad (3)$$

According to a self-similar solution<sup>19</sup> and simulation results, the pressure behind the unsupported shock changes nearly linearly with mass,  $p \sim m$ . In this case, Eq. (3) gives  $p_{\text{sh}} \sim m_{\text{sh}}^{-1.14} \rho_0^{0.71}$ . The first shock travels through uniform density; therefore, the shock pressure decays as  $p_1 \sim m_{\text{sh}}^{-1.14}$  and the post-shock adiabat varies as  $\alpha_1 \sim m^{-1.14}$ . Compared to the results of a self-similar solution,<sup>19</sup> the error in the power index predicted by this model is within 10%. The density after the shock evolves as  $\rho \sim (p/\alpha_1)^{3/5}$ . Therefore, as the second shock is launched, the density ahead of its front grows as  $\rho_0 \sim m_{\text{sh}}^{1.29}$  and shock pressure decays as  $p_2 \sim m_{\text{sh}}^{-0.22}$ . To generalize, if an  $i + 1$  shock with  $p_{i+1} \sim m_{\text{sh}}^{\delta_{i+1}}$  travels through the flow with an adiabat profile  $\alpha_i \sim m^{-\omega_i}$ , the model gives  $\delta_{i+1} = 0.57 \delta_i + 0.43$  and  $\omega_{i+1} = 0.57 \omega_i + 1.71$  with  $\delta_1 = -\omega_1 = -1.14$ . Therefore, starting with the third shock, the pressure at the unsupported shock front increases as the shock travels through the shell. For the main shock launched after  $N$  decaying shocks and supported by pressure  $p_d$ , Eq. (3) gives (assuming that pressure changes linearly with the mass coordinate)

$$p_{\text{main}} = p_d \left[ 3(\omega_N + 1) \left( m_{\text{sh}} / m^* \right)^{\delta_{N+1}} - 8 \right] / (3\omega_N - 5),$$

where  $m^*$  is a normalization constant that depends on picket duration.

The model shows that the main shock pressure increases as the shock propagates through the shell, significantly exceeding the ablation pressure. To avoid an increase in the inner adiabat caused by this pressure amplification, it is necessary to either increase the number of pickets to 4 or reduce the strength of the main shock by introducing an intensity step at the beginning of the main drive. Since incorporating the fourth picket in the design is very challenging because of the short time separation between the last picket and the main drive, a combination of three pickets and a step pulse is chosen as a baseline for the multiple-picket, low-adiabat designs.

As mentioned earlier, all shocks launched by the pickets and the main drive must coalesce nearly simultaneously in the vapor region of the target, in close proximity to the inner shell surface.

A VISAR measurement in an optimized design should produce, therefore, a decaying velocity of the first shock, followed by a rapid velocity increase, at the coalescence time, up to a value above  $\sim 120 \mu\text{m/ns}$  (see the dotted line in Fig. 121.1). Because of the radiative precursor, the VISAR signal is absorbed in a region ahead of the shock front if  $V_{\text{sh}} > 75 \mu\text{m/ns}$  (Ref. 20). As a result, only the first shock velocity and time of shock coalescence can be measured by the VISAR. Deviations from the predicted strength of any shock can be inferred by observing multiple jumps in the velocity of the leading shock wave. For example, if the third picket is too high, the third shock will prematurely overtake the second and first shocks, resulting in an early velocity jump, as shown in Fig. 121.1. The measurement presented in Fig. 121.1 was performed on OMEGA with a 900- $\mu\text{m}$ -diam, 10- $\mu\text{m}$ -thick CD shell filled with liquid  $\text{D}_2$  and fitted with a VISAR cone.<sup>17</sup> As seen in Fig. 121.1, the two coalescence events, separated by  $\sim 300$  ps, are a signature of mistimed shocks that can be corrected by reducing the intensity of the third picket.

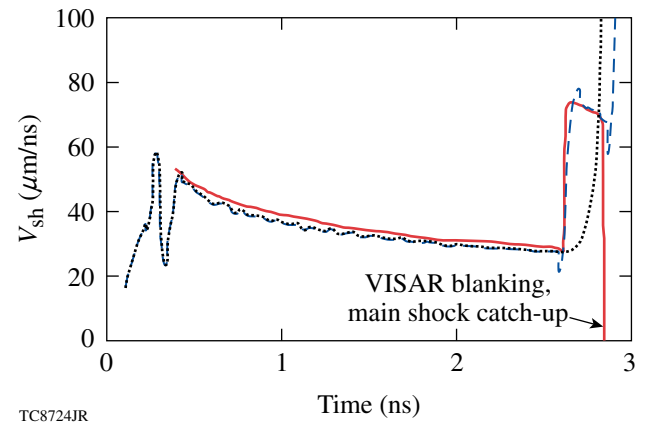


Figure 121.1

Example of leading shock-velocity history measured (red line) and predicted (dashed line) in the TP design with a mistimed third shock. The calculated velocity history for an optimized design is shown by the dotted line.

To verify the shock optimization procedure and validate control of the main shock strength with an intensity step, the TP designs with both square and step main pulses were used on OMEGA to drive targets with a 65- $\mu\text{m}$ -thick cryogenic-DT layer overcoated with a 10- $\mu\text{m}$  CD shell. The pulse shapes shown in Fig. 121.2 had a peak intensity of  $\sim 8 \times 10^{14} \text{ W/cm}^2$ . The laser energy varied from 23 kJ for the square main pulse to 25 kJ for the step main pulse, respectively. The predicted implosion velocity in these designs reached  $V_{\text{imp}} = 3 \times 10^7 \text{ cm/s}$ . A magnetic recoil spectrometer (MRS)<sup>6</sup> was used to infer  $\langle \rho R \rangle_n$ . Two charged-particle spectrometers (CPS's) were also used to

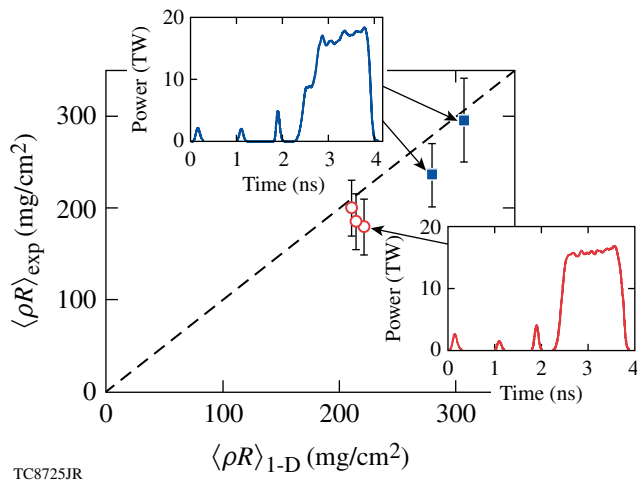


Figure 121.2

Predicted and measured areal densities for triple-picket square (circles) and step (squares) OMEGA designs. The inserts show the pulse shapes used to drive the implosions.

measure the spectral shape of the knock-on deuterons (KOD's), elastically scattered by primary DT neutrons. The shape in the KOD spectrum is insensitive, however, to areal densities above  $\langle \rho R \rangle_n > 180 \text{ mg/cm}^2$  (Ref. 6). These measurements were used to infer the lower limit on  $\langle \rho R \rangle_n$  as well as assess asymmetries developed at different views of an implosion. In Fig. 121.2 the measured areal densities are compared to those calculated using the one-dimensional hydrocode *LILAC*.<sup>21</sup> Good agreement between measurements and calculations validates the accuracy of shock tuning in the TP designs. Also, the observed increase in  $\langle \rho R \rangle_n$  in the step design confirms that the inner adiabat can be accurately controlled by changing step amplitude in the main drive.

Based on the good performance of the TP designs on OMEGA, a new triple-picket, direct-drive-ignition design is proposed for the NIF (Fig. 121.3). Driven at a peak intensity of  $8 \times 10^{14} \text{ W/cm}^2$ , the shell reaches  $V_{\text{imp}} = 3.5$  to  $4 \times 10^7 \text{ cm/s}$ , depending on the thickness of the fuel layer. At a laser energy of 1.5 MJ, this design is predicted to ignite with a gain  $G = 48$ . A stability assessment of the NIF TP design is currently in progress.

In summary, triple-picket designs were used in cryogenic-DT implosions on OMEGA. The highest areal densities ever measured in cryogenic-DT implosions (up to  $300 \text{ mg/cm}^2$ ) were inferred with  $V_{\text{imp}} \sim 3 \times 10^7 \text{ cm/s}$  driven at a peak laser intensity of  $8 \times 10^{14} \text{ W/cm}^2$ . Scaled to the NIF, the TP design is predicted to ignite with a gain  $G = 48$ .

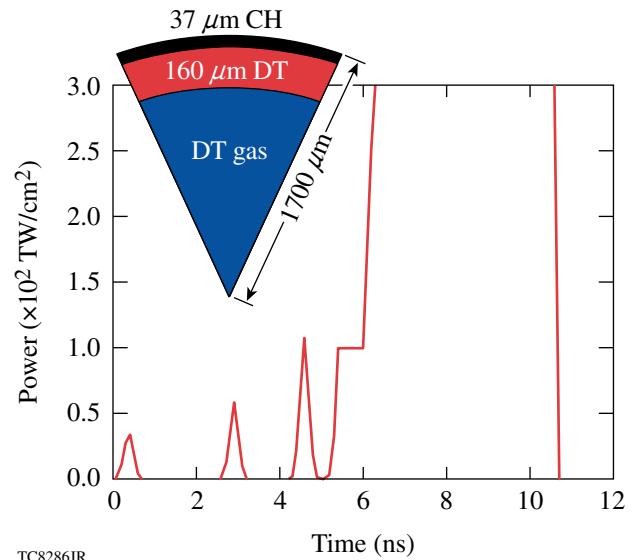


Figure 121.3

Triple-picket, direct-drive design for the NIF.

## ACKNOWLEDGMENT

This work was supported by the U.S. Department of Energy Office (DOE) of Inertial Confinement Fusion under Cooperative Agreement No. DE-FC52-08NA28302, the University of Rochester, and the New York State Energy Research and Development Authority. The support of DOE does not constitute an endorsement by DOE of the views expressed in this article.

## REFERENCES

1. J. D. Lindl, *Inertial Confinement Fusion: The Quest for Ignition and Energy Gain Using Indirect Drive* (Springer-Verlag, New York, 1998).
2. M. C. Herrmann, M. Tabak, and J. D. Lindl, *Phys. Plasmas* **8**, 2296 (2001).
3. C. D. Zhou and R. Betti, *Phys. Plasmas* **14**, 072703 (2007).
4. J. Paisner *et al.*, *Laser Focus World* **30**, 75 (1994).
5. T. R. Boehly, D. L. Brown, R. S. Craxton, R. L. Keck, J. P. Knauer, J. H. Kelly, T. J. Kessler, S. A. Kumpan, S. J. Loucks, S. A. Letzring, F. J. Marshall, R. L. McCrory, S. F. B. Morse, W. Seka, J. M. Soures, and C. P. Verdon, *Opt. Commun.* **133**, 495 (1997).
6. J. A. Frenje, C. K. Li, F. H. Séguin, D. T. Casey, R. D. Petrasso, T. C. Sangster, R. Betti, V. Yu. Glebov, and D. D. Meyerhofer, *Phys. Plasmas* **16**, 042704 (2009).
7. F. H. Séguin, C. K. Li, J. A. Frenje, D. G. Hicks, K. M. Green, S. Kurebayashi, R. D. Petrasso, J. M. Soures, D. D. Meyerhofer, V. Yu. Glebov, P. B. Radha, C. Stoeckl, S. Roberts, C. Sorce, T. C. Sangster, M. D. Cable, K. Fletcher, and S. Padalino, *Phys. Plasmas* **9**, 2725 (2002).
8. S. Chandrasekhar, in *Hydrodynamic and Hydromagnetic Stability*, International Series of Monographs on Physics (Clarendon Press, Oxford, 1961), p. 428.

9. P. W. McKenty, V. N. Goncharov, R. P. J. Town, S. Skupsky, R. Betti, and R. L. McCrory, *Phys. Plasmas* **8**, 2315 (2001).
10. V. N. Goncharov, J. P. Knauer, P. W. McKenty, P. B. Radha, T. C. Sangster, S. Skupsky, R. Betti, R. L. McCrory, and D. D. Meyerhofer, *Phys. Plasmas* **10**, 1906 (2003).
11. J. D. Lindl and W. C. Mead, *Phys. Rev. Lett.* **34**, 1273 (1975).
12. F. J. Marshall, R. S. Craxton, J. A. Delettrez, D. H. Edgell, L. M. Elasky, R. Epstein, V. Yu. Glebov, V. N. Goncharov, D. R. Harding, R. Janezic, R. L. Keck, J. D. Kilkenny, J. P. Knauer, S. J. Loucks, L. D. Lund, R. L. McCrory, P. W. McKenty, D. D. Meyerhofer, P. B. Radha, S. P. Regan, T. C. Sangster, W. Seka, V. A. Smalyuk, J. M. Soures, C. Stoeckl, S. Skupsky, J. A. Frenje, C. K. Li, R. D. Petrasso, and F. H. Séguin, *Phys. Plasmas* **12**, 056302 (2005).
13. T. C. Sangster, R. Betti, R. S. Craxton, J. A. Delettrez, D. H. Edgell, L. M. Elasky, V. Yu. Glebov, V. N. Goncharov, D. R. Harding, D. Jacobs-Perkins, R. Janezic, R. L. Keck, J. P. Knauer, S. J. Loucks, L. D. Lund, F. J. Marshall, R. L. McCrory, P. W. McKenty, D. D. Meyerhofer, P. B. Radha, S. P. Regan, W. Seka, W. T. Shmayda, S. Skupsky, V. A. Smalyuk, J. M. Soures, C. Stoeckl, B. Yaakobi, J. A. Frenje, C. K. Li, R. D. Petrasso, F. H. Séguin, J. D. Moody, J. A. Atherton, B. D. MacGowan, J. D. Kilkenny, T. P. Bernat, and D. S. Montgomery, *Phys. Plasmas* **14**, 058101 (2007).
14. V. A. Smalyuk, R. Betti, T. R. Boehly, R. S. Craxton, J. A. Delettrez, D. H. Edgell, V. Yu. Glebov, V. N. Goncharov, D. R. Harding, S. X. Hu, J. P. Knauer, F. J. Marshall, R. L. McCrory, P. W. McKenty, D. D. Meyerhofer, P. B. Radha, S. P. Regan, T. C. Sangster, W. Seka, R. W. Short, D. Shvarts, S. Skupsky, J. M. Soures, C. Stoeckl, B. Yaakobi, J. A. Frenje, C. K. Li, R. D. Petrasso, and F. H. Séguin, *Phys. Plasmas* **16**, 056301 (2009).
15. T. C. Sangster, V. N. Goncharov, P. B. Radha, V. A. Smalyuk, R. Betti, R. S. Craxton, J. A. Delettrez, D. H. Edgell, V. Yu. Glebov, D. R. Harding, D. Jacobs-Perkins, J. P. Knauer, F. J. Marshall, R. L. McCrory, P. W. McKenty, D. D. Meyerhofer, S. P. Regan, W. Seka, R. W. Short, S. Skupsky, J. M. Soures, C. Stoeckl, B. Yaakobi, D. Shvarts, J. A. Frenje, C. K. Li, R. D. Petrasso, and F. H. Séguin, *Phys. Rev. Lett.* **100**, 185006 (2008).
16. L. M. Barker and R. E. Hollenbach, *J. Appl. Phys.* **43**, 4669 (1972).
17. T. R. Boehly, D. H. Munro, P. M. Celliers, R. E. Olson, D. G. Hicks, V. N. Goncharov, G. W. Collins, H. F. Robey, S. X. Hu, J. A. Marozas, T. C. Sangster, O. L. Landen, and D. D. Meyerhofer, *Phys. Plasmas* **16**, 056302 (2009).
18. L. D. Landau and E. M. Lifshitz, *Fluid Mechanics*, 2nd ed., Course of Theoretical Physics, Vol. 6 (Butterworth-Heinemann, Newton, MA, 1987).
19. Ya. B. Zel'dovich and Yu. P. Raizer, in *Physics of Shock Waves and High-Temperature Hydrodynamic Phenomena*, edited by W. D. Hayes and R. F. Probstein (Dover Publications, Mineola, NY, 2002), Vol. II, Chap. XII, pp. 820–848.
20. D. H. Munro *et al.*, *Phys. Plasmas* **8**, 2245 (2001).
21. J. Delettrez, R. Epstein, M. C. Richardson, P. A. Jaanimagi, and B. L. Henke, *Phys. Rev. A* **36**, 3926 (1987).

---

# High-Precision Measurements of the Equation of State of Hydrocarbons at 1 to 10 Mbar Using Laser-Driven Shock Waves

## Introduction

Shock waves are routinely used to study the behavior of materials at high pressure. Recently, laser-driven shock waves provided equation-of-state (EOS) data for a variety of materials used in high-energy-density ( $E/V \geq 10^{11} \text{ J/m}^3$ ) physics experiments at pressures above 1 Mbar (Refs. 1–3). Such data are relevant to inertial confinement fusion (ICF) targets for the National Ignition Facility (NIF), where multiple shock waves are used to provide an approximate isentropic compression of the fusion fuel.<sup>4,5</sup> Understanding how polymer ablators respond to several-Mbar shock waves is critical to optimizing target performance.

Some of the NIF indirect-drive ablators will be made of glow-discharge polymer (GDP) ( $\text{C}_{43}\text{H}_{56}\text{O}$ ) with various levels of germanium doping (Ge-GDP).<sup>6,7</sup> No high-pressure data exist for these materials. Polystyrene (CH) is closest in structure and was considered a coarse indicator for shock-timing simulations of NIF targets involving such ablators. Shocked polystyrene has been studied using gas-gun drivers up to  $\sim 0.5$  Mbar and laser-driven shock waves between  $\sim 7$  to 41 Mbar (Refs. 8–10). Experiments above 1 Mbar (Refs. 8 and 9) had large error bars and appeared to behave noticeably stiffer than the models used to match the low-pressure data. Moreover, there was no verification of material behavior in the pressure range relevant to the NIF multiple-shock compression scheme, where successive shocks produce pressures of around 1 to 10 Mbar.<sup>11</sup> The use of these limited, low-precision data for polystyrene to predict the behavior of NIF Ge-doped ablator materials provides an unacceptable uncertainty.

Ultimately, the goal is to verify and understand the behavior of Ge-GDP at pressures of 1 to 10 Mbar. EOS models for this material will likely be based on existing models for polymers. To this end, we first address the behavior of polystyrene to determine whether this material indeed behaves stiffer than predicted, as suggested by Refs. 8 and 9. Next, the effect of stoichiometry (C-to-H ratio) is studied by measuring the EOS of polypropylene. Having quality EOS data on these two materials will provide a basis on which models of more-complicated

polymers (Ge-GDP) can be based. This article reports the results of precise EOS measurements on polystyrene and polypropylene and compares them to existing data.

Polystyrene and polypropylene ( $\text{CH}_2$ ) are relatively simple organic compounds, composed solely of hydrogen and carbon. Atoms in each polymer molecule are covalently bonded, while attraction between molecules can include Van der Waals forces, dipole interactions, and hydrogen bonds.<sup>12</sup> These hydrocarbons are thought to experience chemical decomposition into phases of diamond-like C and H (Ref. 13) at sufficiently high pressures and temperatures. Several studies have demonstrated this using principal Hugoniot data in the 0.01- to 1-Mbar regime.<sup>13,14</sup> Electrical conductivity measurements<sup>15</sup> in a similar pressure range showed a predictable dependency on the C-to-H ratio in the hydrocarbons. Studying CH and  $\text{CH}_2$  in the high-energy-density regime opens the possibility of observing high-pressure chemistry.

In the present study, laser-driven shock waves were used to produce high-precision impedance-matching (IM) measurements using quartz as a reference material.<sup>1,16–18</sup> This provided  $\sim 1\%$  precision in shock-velocity measurements. Single-shock measurements were performed on CH and  $\text{CH}_2$ , showing that both materials undergo similar compressions between 1 to 10 Mbar, although their behavior in the  $P$ – $\rho$  plane is distinctly different. Measurements of reflectance and brightness temperatures show that these two hydrocarbons behave similarly at high pressures. Additionally, polystyrene's behavior under double-shock compression was measured, and those results were consistent with single-shock results. All measurements are compared with available models and previous works.

In the following sections, experimental conditions including diagnostics and targets are described; the IM technique, including single- and double-shock states, is discussed, with emphasis on improvements that enable one to acquire high-precision data; high-precision velocity measurements and error analysis are discussed in more detail; and, finally, results are presented, followed by concluding remarks.

## Experiment

Experiments were performed on LLE's OMEGA Laser System.<sup>19</sup> Shock pressures of 1 to 10 Mbar were produced by laser energies between 200 J and 1130 J delivered in 2-ns temporally square pulses of 351-nm light. The laser's focal spot was smoothed using distributed phase plates,<sup>20</sup> resulting in nearly uniform irradiation spots with diameters of either 600 or 800  $\mu\text{m}$ . The average laser intensity was between 0.3 and  $1.1 \times 10^{14}$  W/cm<sup>2</sup>.

The targets for the single-shock measurements consisted of 90- $\mu\text{m}$  pushers made of  $z$ -cut  $\alpha$ -quartz with the samples mounted on the rear side. The samples were 50- $\mu\text{m}$ -thick CH and/or CH<sub>2</sub> foils. Impedance measurements were performed at the interface between the quartz and the sample.<sup>21,22</sup> A second set of targets for CH EOS consisted of "anvil" targets, having a second piece of  $z$ -cut  $\alpha$ -quartz glued onto the back of the 50- $\mu\text{m}$  CH sample. For these targets, single-shock measurements were obtained at the first interface (quartz-to-sample), and re-shock measurements were obtained at the second interface (sample-to-quartz), where the shock in the sample reflected off the denser quartz. The glue layers were kept below a few microns. The use of 90- $\mu\text{m}$ -thick pushers minimized preheating of the sample. The laser-produced plasmas that drove these shock waves had temperatures of 1 to 2 keV. The soft- and mid-energy x rays from such plasmas were absorbed in the first half (laser side) of the quartz pusher.

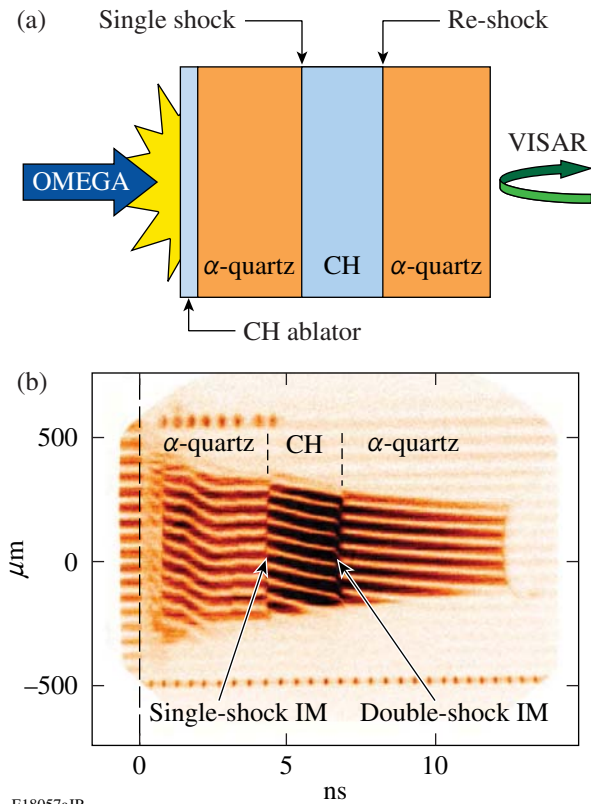
All targets had a 20- $\mu\text{m}$  CH ablator (on the laser side) to absorb the incident laser and reduce the production of x rays that might preheat the samples. To minimize ghost reflections, the free surface of the samples and the quartz anvils had antireflection coatings. Material densities were 2.65 g/cm<sup>3</sup> for quartz, 1.05 g/cm<sup>3</sup> for CH, and 0.90 g/cm<sup>3</sup> for CH<sub>2</sub>. The index of refraction for these materials at the 532-nm probe-laser wavelength was 1.55, 1.59, and 1.49 for quartz, CH, and CH<sub>2</sub>, respectively.

A line-imaging velocity interferometer system for any reflector (VISAR)<sup>23–26</sup> measured shock velocities in the samples. The drive pressures were sufficient to produce optically reflective shock fronts in both the quartz and the polymer samples (see **Optical and Thermal Measurements**, p. 16). This resulted in direct, time-resolved measurements of the shock velocity in both the pusher and the samples. Two VISAR's with different velocity sensitivities were used to discern the  $2\pi$  phase-shift ambiguity that occurs when the shock velocity instantaneously jumps at material interfaces. Etalons of 18-mm and 7-mm thickness were used to produce uncorrected velocity

sensitivities of 2.732 and 6.906  $\mu\text{m}/\text{ns}/\text{fringe}$ , respectively. The indices of refraction determined the VISAR sensitivity in each material. The VISAR data were analyzed with a fast Fourier transform (FFT) method that determines fringe position to  $\sim 5\%$  of a fringe. Since the shock speeds used in these experiments typically cause approximately five fringe shifts, velocities are measured to  $\sim 1\%$  precision (lower shock speeds produce slightly larger velocity errors). Shock-front reflectivity information is encoded in the fringe pattern and can be obtained by measuring its amplitude after applying the FFT. Since the drive pressures are high enough to cause metallic-like states in the materials, the probe-laser reflection occurs within the skin depth ( $\sim 100$  nm or less)<sup>23</sup> of the metalized fluid; this, along with the steep shock front, produces a highly reflective surface. The probe laser for VISAR was a  $Q$ -switched, injection-seeded Nd:YAG laser operating at 532 nm with a pulse length of  $\sim 50$  ns at full width at half maximum (FWHM). The reflected probe signal was detected by a ROSS<sup>27</sup> streak camera, one for each VISAR, having either 15- or 9-ns temporal windows. The response time of the diagnostic was dominated by the delay time associated with the etalons—90 or 40 ps.

An absolutely calibrated streaked optical pyrometer (SOP)<sup>28</sup> was used simultaneously with VISAR. The SOP measured the visible and near-infrared self-emission from the shock front as it propagated through the target. Its wavelength-dependent spectral responsivity was determined by the relay optics, diagnostic filtration (long pass filter with a cutoff wavelength of 590 nm), and streak camera photocathode response, defining a red channel from 590 to 900 nm. The device was absolutely calibrated using a NIST-traceable tungsten lamp and power supply.<sup>28</sup> The temporal window of the diagnostic was set to 10 or 20 ns, depending on expected irradiances on target. Using a 500- $\mu\text{m}$  slit and a 10-ns temporal window led to an  $\sim 170$ -ps temporal response time.<sup>28</sup> The SOP provides a temporal history of shock-front temperature. The VISAR and SOP are temporally calibrated so that combining the data provides temperature as a function of velocity and, consequently, temperature as a function of pressure.

The experimental configuration is shown in Fig. 121.4(a). The OMEGA Laser System irradiates the CH ablator on the front of the EOS targets, producing a shock wave that traverses the quartz pusher, sample, and quartz anvil (the quartz anvil was not used for all experiments). The VISAR and SOP view the rear side of the target, and since each of these layers is transparent, they measure the shock velocity and self-emission inside each layer. Figure 121.4(b) shows VISAR data for an anvil target. The horizontal lines are the VISAR fringes whose vertical



E18057aJR

Figure 121.4

(a) Schematic of planar anvil targets used in the experiments. The laser drive irradiates the target from the left, while the VISAR probe beam reflects off the shock from the rear side of the target (right). (b) VISAR streak image, showing continuous track of shock front within standard and sample.

position is proportional to the shock velocity. Before  $t = 0$ , the fringes are horizontal and constant because no shock wave is present. The x rays from the laser-driven plasma (which start at  $t = 0$ ) caused the CH ablator to become opaque. As a result, the VISAR fringes disappear from  $t = 0$  to  $\sim 0.7$  ns. At 0.7 ns the shock wave enters the quartz, where the VISAR detects it. The shock-wave strength decays as it transits the quartz but soon stabilizes as the rarefactions equilibrate the pressure between the target layers and the ablation front driven by the laser. This produces a relatively steady shock from 2 to 4.3 ns.

At 4.3 ns, the shock wave transits the quartz–CH interface and enters the CH, where its velocity changes. This is seen as a jump in the position of the VISAR fringes and an abrupt change in their intensity. The latter is a result of the difference in the reflectivities of the shock waves in quartz and CH. The single-shock IM measurement is made across this interface. At 6.7 ns the shock wave reaches the quartz anvil and the fringe position and intensity change again. The double-shock (re-shock) IM measurements are made at this interface.

Note in Fig. 121.4(b) that the observed quartz–CH interface has a finite temporal width; this is the region where the shock transits the thin glue layer. In addition, the VISAR response time (given by the etalon thickness) is 40 ps and 90 ps. The shock velocities are, therefore, not measured directly at the contact interface between materials. This is accounted for by linearly fitting the shock velocities at least 0.3 ns before and after the interface transition region and extrapolating to the “ideal” interface. This also accounts for any slope present in these velocity profiles.

Compared to previous studies on hydrocarbons in the Mbar range, this study is novel in both the precision (1%) of the velocity measurements and the treatment of the errors in the IM technique: both random and systematic errors are evaluated. The next section describes the IM technique and the error analysis used for this study.

### Impedance-Matching Analysis

#### 1. Single-Shock Experiments

The jump conditions for shock waves are described by the Rankine–Hugoniot relations derived from the conservation of mass, momentum, and energy; they relate pre- and post-shock conditions via particle velocity ( $U_p$ ) and shock velocity ( $U_s$ ),<sup>21,22</sup> as

$$P_1 - P_0 = \rho_0 U_s U_p, \quad (1)$$

$$\rho_1 (U_s - U_p) = \rho_0 U_s, \quad (2)$$

$$E_1 - E_0 = \frac{1}{2} (P_1 + P_0) \left( \frac{1}{\rho_0} - \frac{1}{\rho_1} \right), \quad (3)$$

where subscripts 0 and 1 denote initial and shock conditions in terms of pressure  $P$ , density  $\rho$ , and internal energy  $E$ . The first two equations have four unknowns (given that the initial pressure and density are known) and can be solved by measuring two variables. This solution constitutes a kinematic equation of state and is often defined as  $U_s$  as a function of  $U_p$ . High-pressure shock waves are typically reflecting, allowing one to optically measure the shock velocity, but usually preventing direct optical measurement of the particle velocity. The IM technique is used to infer the particle velocity by referencing the sample under study to a standard material whose equation of state is known.<sup>21,22</sup>

The conservation equations dictate that the pressure and particle velocity are conserved across the contact interface between the standard and the sample. This makes it possible to infer the common particle velocity from the shock velocities in the standard and the sample, as the shock wave enters and exits the contact interface between the materials. This is shown in Fig. 121.5(a) in the pressure–particle velocity ( $P-U_p$ ) plane. A measurement of the shock velocity in the standard provides the initial condition of the shock wave before it interacts with the sample. This state (A) is the intersection of the Rayleigh line ( $P = \rho_0 U_s U_p$ ) and the known Hugoniot for the standard. If the sample has lower impedance than the standard, the standard will undergo isentropic release until its impedance “matches” that of the sample, when the continuity equations are satisfied across the interface between the standard and the sample. This determines the shocked state of the sample [state (B) in Fig. 121.5(a)]. This shocked state is the intersection between the release curve for the standard and the Rayleigh line defined by the measurement of the shock velocity in the sample. By measuring two shock velocities (one in the standard and one in the sample), the particle velocity in the sample can be inferred. The  $U_s$  and  $U_p$  for the sample define the equation of state of the sample. Care must be taken to ensure that the measured shock velocities are those just before and just after the shock wave crosses the interface between the two materials. The shock-wave jump conditions are a consequence of conservation of mass and momentum, which are always satisfied regardless of shock stability. Therefore, shock steadiness is not a requirement for IM with transparent standards since jump conditions for a shock hold for decaying (and increasing) shock waves. If the measurement has sufficient time resolution, the requirement for shock steadiness can be relaxed as long as the variation in velocity can be measured.

The IM technique requires knowledge of the Hugoniot and release behavior of the standard. The precision of the data obtained through the IM technique depends on the accuracy with which the states in the standard are known. The quartz principal Hugoniot was studied in the high-pressure fluid regime (2 to 15 Mbar) using laser-driven shock waves.<sup>1</sup> That study bridged the gap in data between existing gas-gun,<sup>29,30</sup> explosively driven,<sup>31</sup> and nuclear-driven<sup>32</sup> experiments. The laser-driven data were consistent with previous studies having longer characteristic time scales. This indicates that the shock waves equilibrate on time scales shorter than the measurement times in laser experiments. The data show that shocked quartz is solid up to about 1 Mbar; above 1 Mbar shocked quartz melts and becomes reflective. The EOS of quartz is characterized by a piecewise linear  $U_s-U_p$  relationship of the general form  $U_s = a_0 + a_1(U_p - \beta)$  as

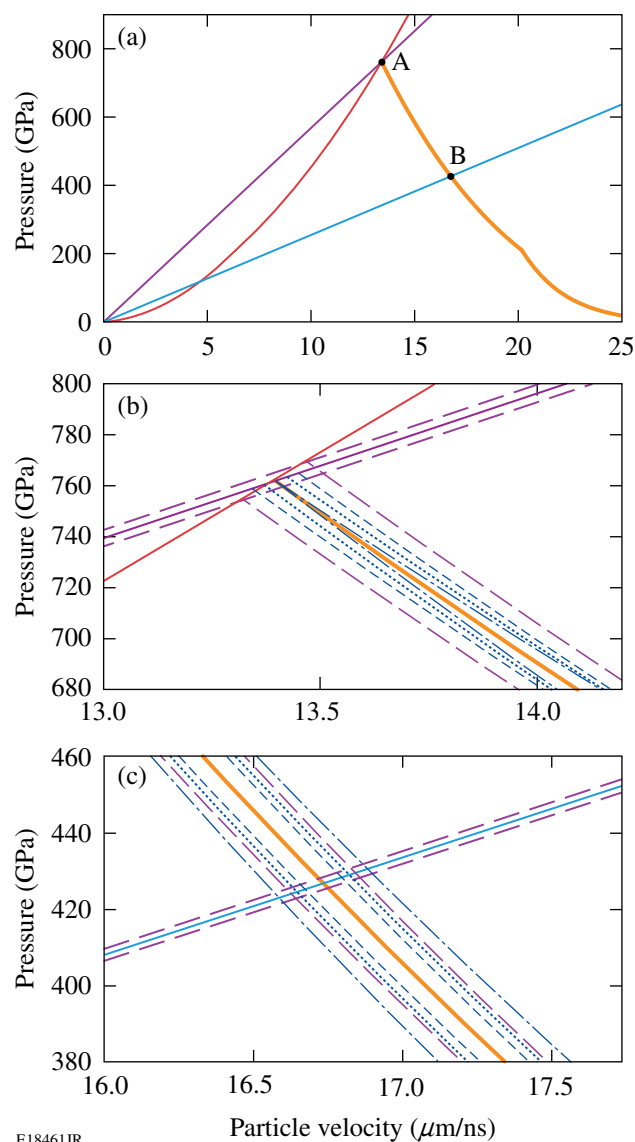


Figure 121.5 Sample IM construct with inclusion of errors for a 7.6-Mbar shock propagating from quartz to CH. Total errors are found by taking the quadrature sum of random and systematic uncertainties. (a) General IM diagram. Rayleigh lines for quartz and CH are shown as purple and light blue lines, respectively, while red and orange solid curves correspond to the principal Hugoniot and release of quartz. (b) Errors associated with quartz’s initial shock state and release variation from nominal. Systematic contributions are shown in dark blue and random contributions are shown in purple. Error in quartz’s Rayleigh line is shown by purple dashed lines. This causes a random variation propagated as an offset release curve, shown as purple dashed lines. Systematic variations from nominal release are shown as dark blue dashed–dotted, dashed, and small dashed curves, corresponding to  $\delta\Gamma$ ,  $\delta a_0$ , and  $\delta a_1$ , respectively. (c) Final variations from a nominal ( $U_p, P$ ) state are depicted by intersections between the nominal CH Rayleigh line and previously mentioned releases caused by random and systematic error contributions. A second random error contribution is found through the intersection between nominal quartz release and the CH Rayleigh line with  $\delta U_{s,CH}$  contribution, shown as a purple dashed line.

$$U_s = (6.914 \pm 0.028) + (1.667 \pm 0.038)(U_p - 3.0244), \quad (4)$$

for  $U_p < 6.358 \mu\text{m/ns}$ ,

$$U_s = (19.501 \pm 0.068) + (1.276 \pm 0.022)(U_p - 11.865), \quad (5)$$

for  $U_p \geq 6.358 \mu\text{m/ns}$ ,

where an orthonormal basis is used so that the resulting errors are uncorrelated.<sup>18</sup> This  $U_s$ - $U_p$  relation was used in this work.<sup>33</sup> The quartz was shocked to 1 to 15 Mbar, producing reflective shock waves that allowed for VISAR measurements of the shock velocity, thereby providing the initial state of the standard for IM.

The quartz's impedance was matched to the sample when its release isentrope intersected the Rayleigh line in the sample. Quartz's release isentropes were calculated using the Mie-Grüneisen formalism as described in previous works.<sup>18,34</sup> In this work's analysis, the reflected experimental Hugoniot was used, resulting in isentropes that follow a piecewise behavior stemming from the description of quartz's principal Hugoniot EOS, as described by Eqs. (4) and (5) [Fig. 121.5(a)]. For strongly shocked quartz in the dense fluid regime, calculations of the Mie-Grüneisen parameter based on solid and porous silica Hugoniot measurements<sup>1,32,35</sup> showed  $\Gamma$  to be nearly constant with a value  $\Gamma = 0.66 \pm 0.1$  (Ref. 18). Inspection of various EOS models for silica in the high-pressure fluid regime led to a constant value  $\Gamma = 0.64 \pm 0.11$  (Ref. 2), consistent with the experimentally derived value. This latter model-based value for  $\Gamma$  and its associated error were used in this work. The value of  $\Gamma$  is the only model-dependent parameter used here.

The total error in the measured  $U_p$ ,  $P$ , and  $\rho$  is the quadrature sum of the random and systematic errors inherent in the IM technique. Random errors originate in the shock-velocity measurements in both the quartz and samples. Systematic uncertainties arise from errors in the EOS of the standard, i.e., the  $a_0$  and  $a_1$  coefficient of quartz's experimentally derived principal Hugoniot, and from the Mie-Grüneisen parameter  $\Gamma$ . The relative contributions of these errors varied over the range of pressures studied.

## 2. Double-Shock Experiments

The above discussion of the IM technique applies to single-shock measurements, i.e., the standard and sample both experience a single shock wave. Multiple shock waves

produce off-Hugoniot states that are pertinent to ICF target designs that employ multiple shock waves to approximate isentropic compression. Double-shock measurements can validate models since they amplify small differences in the principal Hugoniot.<sup>36</sup>

A double-shock measurement was created in these experiments by placing a second slab of quartz behind the samples, creating an "anvil" target. The shock wave traveled through the first layer of quartz into the polymer (where single-shock Hugoniot data were obtained). When the shock wave in the sample reached the second layer of quartz, it was reflected back into the sample. The conservation equations applied at this sample-quartz interface and a second IM measurement provided the  $U_p$  and  $P$  for the double-shocked sample. The important measurements were the shock velocity in the sample just before it impacted the quartz and the velocity of the shock wave just after it entered the quartz. The former provided the initial single-shock state of the CH, and the quartz's shock velocity provided the pressure of the second shock wave (which was conserved between the sample and the quartz).

## High-Precision Velocity Measurements

Since quartz is transparent, its use as a standard<sup>1,16-18</sup> provides high-precision EOS data because instantaneous velocities can be measured before and after the IM point (provided the sample is transparent). Several other studies have demonstrated precise IM measurements using quartz as a standard.<sup>2,37</sup>

The continuity equations are central to the IM technique. As the shock traverses the interface, the materials accelerate, expand, and experience shock, reshock, or release, to equilibrate and satisfy those conditions. The use of a quartz standard and VISAR with high temporal resolution significantly reduces the inaccuracies by providing "instantaneous" measurements. In this study, shock velocities were measured to ~1% precision. Trends in the temporal profile of the observed velocities were linearized over the ~300 ps before and after the quartz-sample interface and extrapolated to that interface. This accounted for both the unsteadiness of the shock and the response time of VISAR (i.e., the etalon delays).

The usefulness of EOS data is determined by the size and validity of the error bars. As the precision of the velocity measurements increases, the effects of systematic errors become increasingly important. The random and systematic errors are rigorously accounted for in this study, and the total uncertainties are found by calculating the quadrature sum of random and systematic errors.

The total uncertainties for  $U_p$ ,  $P$ , and  $\rho$ , each obtained through the IM technique, depend on seven error contributions:  $\delta U_{sQ}$ ,  $\delta U_{sCH_x}$ ,  $\delta a_{0L}$ ,  $\delta a_{0H}$ ,  $\delta a_{1L}$ ,  $\delta a_{1H}$ , and  $\delta \Gamma$ . The first two are random errors, associated with the two shock-velocity measurements. The last five are systematic errors, of which the first four are fitting parameters for the quartz experimental Hugoniot  $U_s = a_0 + a_1(U_p - \beta)$ , where subscripts L and H correspond to fitting parameters to the low ( $U_p < 6.358 \mu\text{m/ns}$ ) and high ( $U_p \geq 6.358 \mu\text{m/ns}$ ) linear fits. The last ( $\delta \Gamma$ ) is used to approximate quartz's release isentrope by assuming a Mie–Grüneisen EOS and having knowledge of quartz's principal Hugoniot.

Figures 121.5(a)–121.5(c) show a graphical description of the IM analysis and the errors encountered. Measurement errors  $\delta U_{sQ}$  produce a random uncertainty in the quartz's initial shocked state, producing multiple possible Rayleigh lines that can intersect the quartz Hugoniot at different points. Systematic errors in the quartz Hugoniot produce uncertainty in this initial state. These are shown as the  $1\sigma$  variation in quartz Hugoniot. Continuing with this formalism, each of these possible states can be the initial condition for the isentropic release of quartz, which has errors associated with  $a_0$ ,  $a_1$ , and  $\Gamma$ . These release curves form a cascade of possible release curves that the standard could follow. Figures 121.5(b) and 121.5(c) indicate the quantitative bounds on the release curves that can be used for an IM solution.

The state of the shocked sample and therefore the final state of the quartz release were determined by the measured shock velocity in the sample. Errors in this measurement,  $\delta U_{sCH_x}$ , produced multiple Rayleigh lines that intersect with the various release curves. Rigorous propagation of these errors provides confidence in the error bars that were assigned to the pressure and particle velocity inferred from the IM technique.

The total uncertainty for the derived IM variables is found by taking the quadrature sum of the error contributions. The predominance of random or systematic uncertainties varies with pressure. At low pressures (lower velocities), random uncertainties dominate because the phase excursion results in fewer fringes and the 5% error in fringe location is more significant. Shock-front reflectivities are lower, resulting in lower VISAR signal levels. At higher pressures, the random uncertainties become smaller. At pressures of  $\sim 9$  Mbar in CH, corresponding to quartz pressures of  $\sim 15$  Mbar, systematic uncertainties are around  $3\times$  larger than random uncertainties. This results from the lower accuracy of the quartz Hugoniot at these higher pressures, making it increasingly difficult to perform precision measurements.

## Kinematic Results

### 1. Polystyrene (CH)

The single-shock results for polystyrene (see Table 121.I) are shown as orange squares in Fig. 121.6, a  $U_s-U_p$  plot that also contains previous results and various models.<sup>38</sup> This study's data were fit with the line  $U_s = (21.029 \pm 0.057) + (1.305 \pm 0.015)(U_p - 14.038)$ , derived using a least-squares fit of the data set with their total error over an orthogonal polynomial basis; this produced uncorrelated errors in the coefficients of the fit. The total error bars for this study are smaller than the random-only errors of other works. The benefit of these smaller errors is demonstrated in Fig. 121.7 showing the various data and models in the  $P-\rho$  plane. The error derived in density scales as  $(\eta-1)$  times the errors in shock velocity, where  $\eta$  is the compression ( $\rho/\rho_0$ ) (Ref. 39). Here the difference in results and models is more apparent.

The data are compared to three *SESAME* models (refer to Figs. 121.6 and 121.7). *SESAME* 7591 and 7592 are similar in the method used to calculate the electronic, nuclear, and 0 K isotherm contributions to the total EOS, where differences arise from certain input parameters used to carry out these calculations. The electronic contribution for both models is calculated via a temperature-dependent Thomas–Fermi–Dirac (TFD) model, with assumption of an average atom, where the exchange parameter is equal to  $2/3$ . The cold curve is obtained from principal Hugoniot measurements and the assumption of a Mie–Grüneisen EOS. At low densities the solution is matched to the Lennard–Jones formula, and at high densities it is matched to calculations obtained through TFD. In addition to the atomic weight (6.510), atomic number (3.5), and initial density, a reference Grüneisen parameter and Debye temperature are required for the cold curve construct. The reference Grüneisen parameter is calculated from experimental values of the specific heat at constant pressure, the isentropic bulk modulus, the thermal expansion coefficient, and the initial density. *SESAME* 7591 adjusts the value of the reference Grüneisen parameter from 0.565 (value used for *SESAME* 7592) to 0.5 in order to reproduce shock EOS data for porous polystyrene. *SESAME* 7591 has higher values for the reference Debye temperature and temperature of melt by  $\sim 16\%$  compared to *SESAME* 7592. The available low-pressure shock data are better predicted by *SESAME* 7592, which closely follows the change in slope in the  $U_s-U_p$  plane between 2 to 4  $\mu\text{m/ns}$  in  $U_p$ . Cohesive energies used in the cold curve calculations are also different between these models: *SESAME* 7591 uses a higher cohesive energy calculated from the heat of vaporization of carbon and the dissociation energy of hydrogen, while for *SESAME* 7592 the cohesive energy was set at

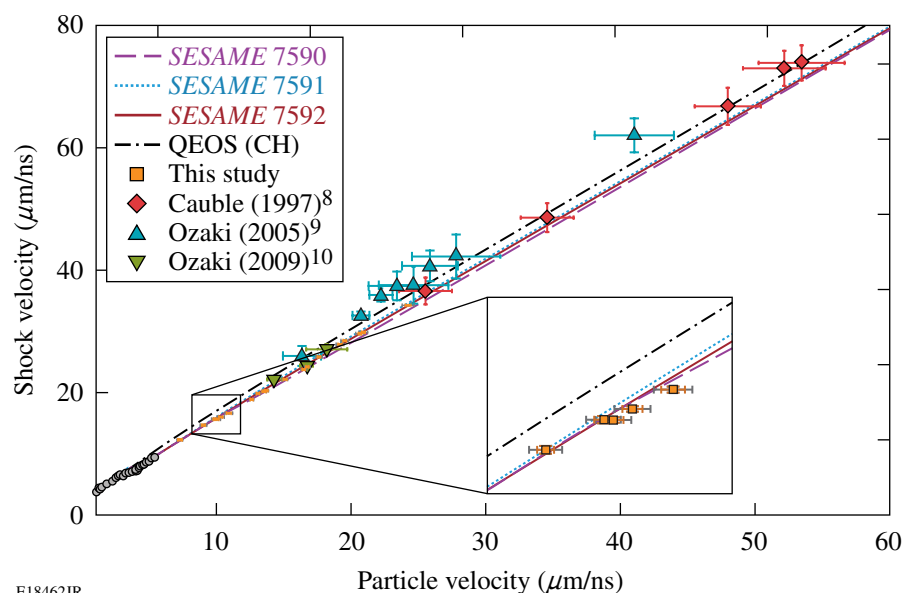


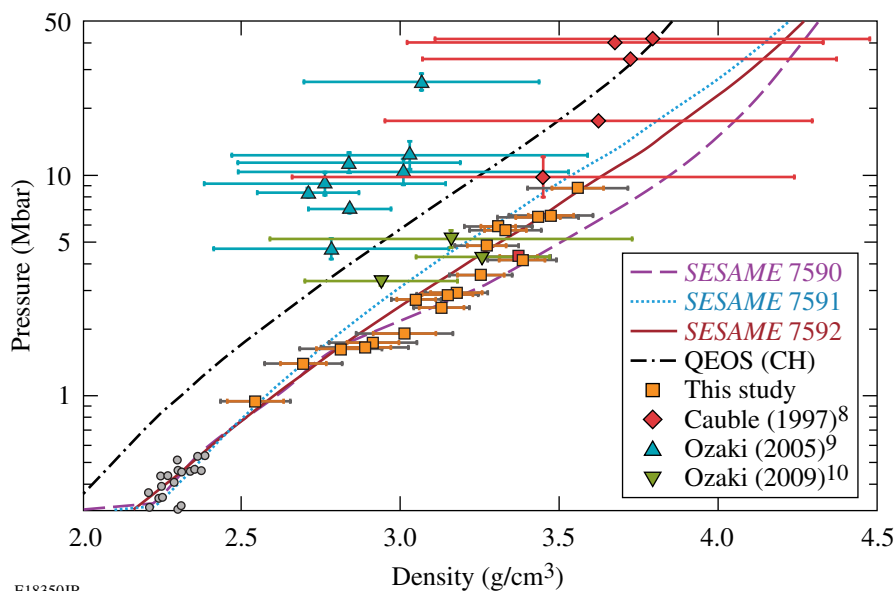
Figure 121.6

Principal Hugoniot data and models for CH in the  $U_s-U_p$  plane. Data for this study were taken on polystyrene ( $C_8H_8$ )<sub>n</sub>, with initial density  $\rho_0 = 1.05$  g/cc, using IM with quartz reference. Random uncertainties are shown as orange error bars and total uncertainty (quadrature sum of random and systematic errors) are shown as gray error bars. Previous gas-gun experiments (gray circles);<sup>30,40-43</sup> absolute measurements on NOVA (red diamonds);<sup>8</sup> and IM experiments on GEKKO using aluminum<sup>9</sup> and quartz<sup>10</sup> reference (cyan and green triangles, respectively). Various SESAME<sup>38</sup> models are shown along with a QEOS model.

E18462JR

Table 121.I: Polystyrene principal Hugoniot results from impedance matching with quartz reference. Measured shock velocity in the quartz and polystyrene,  $U_{sQ}$  and  $U_{sCH}$ , is given with associated random error, arising from measurement limitations.  $U_{pCH}$  (ran,sys),  $P_{CH}$  (ran,sys), and  $\rho_{CH}$  (ran,sys) are the resulting particle velocity, pressure, and density of shocked polystyrene obtained through the IM construct. Random errors enter the analysis through measurement uncertainties in  $U_{sQ}$  and  $U_{sCH}$ , while systematic errors emerge from uncertainties in the principal Hugoniot and release states of quartz.

Shot No.	$U_{sQ}$ ( $\mu\text{m/ns}$ )	$U_{sCH}$ ( $\mu\text{m/ns}$ )	$U_{pCH}$ (ran,sys) ( $\mu\text{m/ns}$ )	$P_{CH}$ (ran,sys) (Mbar)	$\rho_{CH}$ (ran,sys) (g/cc)
52795	11.73±0.19	12.36±0.11	7.26 (0.16, 0.13)	0.94 (0.02, 0.02)	2.54 (0.09, 0.06)
52800	13.68±0.1	14.76±0.12	9.01 (0.12, 0.21)	1.4 (0.02, 0.03)	2.7 (0.07, 0.1)
52793	14.47±0.11	15.74±0.12	9.86 (0.14, 0.22)	1.63 (0.02, 0.04)	2.81 (0.08, 0.1)
52124	14.59±0.12	15.73±0.09	10.01 (0.15, 0.22)	1.65 (0.03, 0.04)	2.89 (0.08, 0.11)
52464	14.85±0.12	16.09±0.09	10.29 (0.15, 0.22)	1.74 (0.03, 0.04)	2.91 (0.08, 0.11)
52628	15.38±0.14	16.72±0.1	10.89 (0.18, 0.22)	1.91 (0.03, 0.04)	3.01 (0.1, 0.11)
52792	17.09±0.09	18.95±0.12	12.6 (0.1, 0.1)	2.51 (0.02, 0.02)	3.13 (0.07, 0.05)
52463	17.63±0.1	19.92±0.1	13.06 (0.11, 0.1)	2.73 (0.03, 0.02)	3.05 (0.06, 0.05)
52631	18.08±0.12	20.27±0.12	13.51 (0.14, 0.11)	2.88 (0.03, 0.02)	3.15 (0.08, 0.05)
52799	18.23±0.12	20.41±0.12	13.66 (0.14, 0.11)	2.93 (0.03, 0.02)	3.18 (0.08, 0.05)
52791	19.72±0.12	22.26±0.1	15.08 (0.14, 0.14)	3.52 (0.03, 0.03)	3.25 (0.07, 0.06)
52634	21.16±0.1	23.87±0.13	16.46 (0.11, 0.17)	4.13 (0.03, 0.04)	3.38 (0.07, 0.08)
52122	21.46±0.09	24.3±0.09	16.73 (0.11, 0.17)	4.27 (0.03, 0.04)	3.37 (0.06, 0.08)
52118	22.45±0.1	25.92±0.12	17.6 (0.12, 0.19)	4.79 (0.04, 0.05)	3.27 (0.06, 0.08)
52121	24.1±0.13	27.98±0.1	19.16 (0.15, 0.23)	5.63 (0.05, 0.07)	3.33 (0.07, 0.09)
52117	24.49±0.11	28.58±0.1	19.51 (0.12, 0.24)	5.86 (0.04, 0.07)	3.31 (0.05, 0.09)
52113	25.64±0.11	29.73±0.16	20.64 (0.13, 0.27)	6.44 (0.05, 0.08)	3.43 (0.07, 0.1)
52633	25.89±0.12	29.94±0.14	20.89 (0.14, 0.27)	6.57 (0.05, 0.09)	3.47 (0.07, 0.11)
52119	29.42±0.18	34.36±0.11	24.22 (0.21, 0.37)	8.74 (0.08, 0.13)	3.56 (0.08, 0.13)



E18350JR

Figure 121.7

Principal Hugoniot data and models for CH in the  $P$ - $\rho$  plane. Data for this study were taken on polystyrene ( $C_8H_8$ )<sub>n</sub>, with initial density  $\rho_0 = 1.05$  g/cc, using IM with quartz reference. Random uncertainties are shown as orange error bars and total uncertainty (quadrature sum of random and systematic errors) are shown as gray error bars. Previous gas-gun experiments (gray circles);<sup>30,40–43</sup> absolute measurements on NOVA (red diamonds);<sup>8</sup> and IM experiments on GEKKO using aluminum<sup>9</sup> and quartz reference<sup>10</sup> (cyan and green triangles, respectively). Various *SESAME*<sup>38</sup> models are shown along with a QEOS model.

15 kcal/mole ( $\sim 4.8$  MJ/kg) in order to reproduce the critical point. The nuclear models calculate the kinetic contribution of atoms and ions in both solid and gas. Lattice vibrational contributions are carried out assuming a Debye–Grüneisen solid; therefore, the reference Grüneisen parameter and Debye temperature are also used in these calculations. At high temperatures or low densities, this nuclear term describes an ideal gas, where ideal mixing is used. These limiting theories are joined by means of interpolation functions.<sup>38,44,45</sup> No detailed information of the construction of *SESAME* 7590 was available.

*SESAME* 7592 appears to best model the present data for polystyrene, although a slight softening with respect to this model is observed between 2 and 4 Mbar. It is thought that at intermediate pressures, the C–H bonds in these polymers undergo chemical decomposition, favoring C–C and H–H bonds. It is possible that the softening at 2 to 4 Mbar indicates these bonds are breaking. This represents an energy sink that could explain the softening.

Previous results by Cauble *et al.*<sup>8</sup> (absolute data) and Ozaki *et al.*<sup>9</sup> (IM with an aluminum standard) show distinctly stiffer behavior than these data and most of the models, as shown in Fig. 121.7. These authors have stated, post publication, that their results likely suffered from x-ray preheating of the samples.<sup>46</sup> The newest data from Ozaki *et al.*<sup>10</sup> used thicker pushers and low- $Z$  ablaters to reduce preheat of the samples. Those experiments also used IM with a quartz standard and show results (green triangles in Fig. 121.7) that are much closer to this work.

In the anvil targets the shocks that reflect off the rear quartz layer produced double-shocked states in CH; these states were measured using the IM at that reflection point (see Table 121.II). The pressure reached in double-shock experiments is highly dependent on the initial state from which it launches, being particularly sensitive to the single-shock density. Because of this dependence, double-shock measurements provide a valuable tool to assess single-shock densities reached in CH. It is difficult to deconvolve measured quantities and model-dependent effects originating from the use of a standard material in the impedance-matching technique; in this aspect, double-shock measurements provide another advantage, where it is possible to separate models and observables, presenting a

Table 121.II: Double-shock states in polystyrene (CH) were probed by using reflected shock waves from anvil targets. Observables, listed below, were used for direct comparison with model behavior.

Shot No.	$U_{sQ}$ ( $\mu\text{m/ns}$ )	$U_{sCH}$ ( $\mu\text{m/ns}$ )
52464	$11.45 \pm 0.16$	$12.25 \pm 0.09$
52792	$13.27 \pm 0.31$	$14.60 \pm 0.09$
52463	$14.14 \pm 0.11$	$15.80 \pm 0.11$
52791	$15.51 \pm 0.10$	$17.45 \pm 0.10$
52122	$17.25 \pm 0.11$	$19.77 \pm 0.09$
52118	$18.77 \pm 0.11$	$21.71 \pm 0.09$
52117	$20.96 \pm 0.11$	$24.65 \pm 0.13$
52113	$23.22 \pm 0.09$	$27.66 \pm 0.11$
52119	$26.25 \pm 0.10$	$31.59 \pm 0.14$

sensitive platform for model comparison. Re-shock results are plotted in Fig. 121.8, showing the experimental observables:  $U_{sQ}$  versus incident  $U_{sCH}$ . Here the associated measurement error bars are quite small. These are compared with double-shock states as predicted by each model. The curves representing each model were produced by performing the IM analysis with each model (using its principal Hugoniot and re-shock curves) and the experimental quartz Hugoniot. The errors produced in this analysis were about the thickness of the lines and stemmed from the experimental errors associated with the quartz fit. The CH shock velocity ( $U_{sCH}$ ) represents the single-shocked state of the CH, and, based on conservation equations, the re-shocked state of CH is derived from quartz's shock velocity  $U_{sQ}$ . Plotting the data in this manner removes any model dependence from the data. Despite the apparent similarity among the models, the small error bars in the data allow one to discriminate between them. This is shown in the inset in Fig. 121.8, an expanded region of the plot near  $26 \mu\text{m/ns}$ . In this type of plot, a model that assumes the material to be more compressible (softer) will display a higher quartz shock velocity for a given CH shock velocity. These re-shock data show behavior similar to the single-shock data, where a slight softening is observed at single-shock pressures from  $\sim 2$  to 4 Mbar. For single-shock pressures outside this range, double-shock data are in agreement with *SESAME 7592*. Such behavior

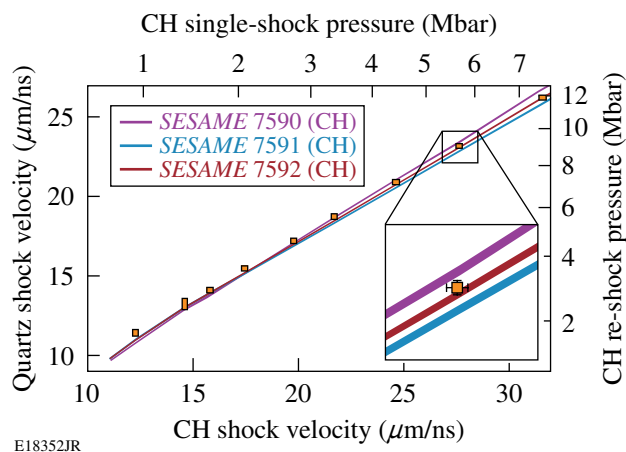


Figure 121.8

Double-shock (re-shock) data for CH using quartz anvil targets. Measured observables are plotted against *SESAME* models,<sup>38</sup> displayed as two quasi-parallel lines, resulting from errors associated with quartz experimental EOS fitting parameters. In this plot, softer models will display higher shock velocities in quartz for a given shock velocity in CH. The data are shown as orange rectangles, where the height and width of each are determined by the associated errors in shock-velocity measurements in CH and quartz, respectively. The data are consistent with the *SESAME 7592* model<sup>38</sup> at high and low pressures, where there is an evident softening of the data from around 2 to 4 Mbar. This shows agreement between single- and double-shock experiments.

is consistent to that observed in single-shock measurements. The measured quantities for CH re-shock experiments can be found in Table 121.II.

Double-shock results can be directly compared to single-shock data by transforming double-shock observables into single-shock quantities in the  $P$ - $\rho$  plane via an inversion method as described by Hicks *et al.* (Ref. 3). This analysis is based on the concept that the double-shock compressibility is better known than the single-shock compressibility—often justified since dissociation along the Hugoniot is the largest source of uncertainty in the models. Such an inversion method uses the Hugoniot equations for the single- and double-shock states and an average of several models (in this case *SESAME* models for polystyrene) to predict the re-shock state through calculation of a model-based averaged adiabatic exponent. By using the double-shock pressure and particle velocity obtained from the measured shock velocity in quartz and quartz's experimental fit, and the shock velocity in the single-shock state, one arrives at a single-shock pressure and density. The results of this analysis (yellow diamonds) are shown in Fig. 121.9, along with the single-shock data. The total uncertainty associated with the inferred single-shock results is represented by black error bars. The total uncertainty is the quadrature sum of systematic uncertainties stemming from the  $1\sigma$  variation in the averaged model-based adiabatic exponent and the errors in the experimental quartz Hugoniot, and random uncertainties stemming from measurement errors in the CH and quartz shock velocity. The inferred principal Hugoniot results are consistent with the single-shock data, also showing a change in compressibility around 4 Mbar. It is important to note that the systematic effects involved in each of these data sets are different, making their agreement significant. In the impedance-matching technique, systematic uncertainties arise from uncertainties in quartz's experimental principal Hugoniot and its release behavior, whereas in the inversion method, systematic effects enter through the experimental quartz Hugoniot and the model-based prediction of the CH re-shock density.

The accuracy of the inversion method was tested by using the model-based-averaged adiabatic exponent and the measurable quantities  $U_{sCH}$  and  $U_{sQ}$ , as predicted by each model. The CH shock velocities used in the analysis spanned a range equivalent to those measured experimentally in the double-shock experiments. The inferred single-shock pressure and density were compared to the pressure and density on the principal Hugoniot, as predicted by each model. Inferred single-shock states were shown to be consistent for all models. For a given pressure, percent differences between density predicted

by models and inferred single-shock density fell between 1%–3%, 1%–2%, and 0.2%–0.3% for *SESAME* 7590, 7591, and 7592, respectively, where differences in density decreased as a function of increasing pressure. This gives confidence that the inversion method leads to accurate results for inferred single-shock conditions.

Quartz is thought to transition from a conducting liquid to a dense plasma at around 4 Mbar. Pressures from 2 to 4 Mbar in

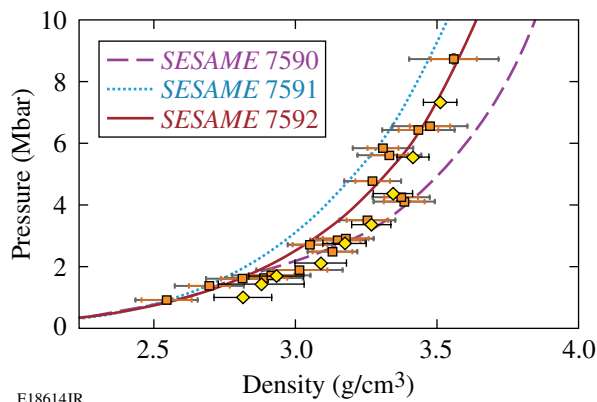


Figure 121.9 Single-shock Hugoniot data for polystyrene as inferred from re-shock (double-shock) data via the inversion method described by Hicks *et al.*<sup>3</sup> are shown as yellow diamonds. Uncertainties are shown as black error bars, which represent the total error (quadrature sum of random and systematic uncertainties). Single-shock IM measurements are also shown (orange squares) along with *SESAME* models.<sup>38</sup> Inferred single-shock data are consistent with single-shock measurements, where both data sets show stiffening of the material starting at 4 Mbar.

CH correspond to pressure from 3.5 to 7 Mbar in quartz. There was concern that the softening in CH was not its true behavior but rather a manifestation of quartz’s rheology. The fact that the double-shock measurements and the inferred single-shock states display similar behavior to that observed in the single-shock data indicates that the softening is not due to a systematic problem with the quartz release. Moreover, results for CH<sub>2</sub> (see **Polypropylene** below), which encounter similar quartz pressures, show no softening. Again, this indicates that the softening observed in CH is its intrinsic high-pressure behavior.

2. Polypropylene (CH<sub>2</sub>)

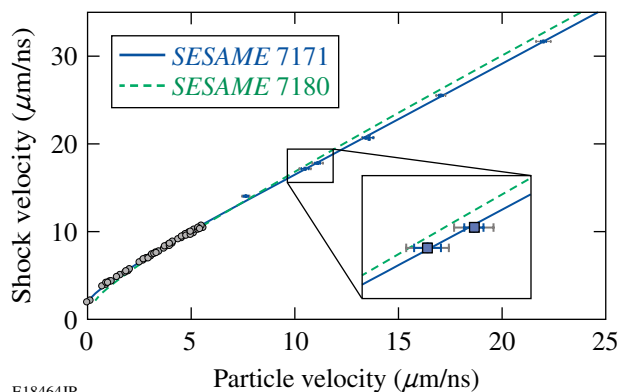
Principal Hugoniot measurements for polypropylene (see Table 121.III) were obtained from 1 to 6 Mbar—the highest published pressure results for this material studied to date. These data have a linear  $U_s-U_p$  relation, shown in Fig. 121.10, described by  $U_s = (20.025 \pm 0.102) + (1.228 \pm 0.025)(U_p - 12.715)$ . A least-squares fitting of the data over an orthogonal polynomial basis was used (using total error) such that the associated errors in the fitting coefficients were uncorrelated. The total uncertainty in the density was between 2.9% and 4.4%. Unlike CH, CH<sub>2</sub> followed a smooth concave trend in the  $P-\rho$  plane, with no pressure-induced softening, as shown in Fig. 121.11. On this plane CH<sub>2</sub> was observed to reach lower density for a given pressure, compared to CH. Compression of both CH and CH<sub>2</sub> (see Fig. 121.12) behaved in a similar manner with increasing pressure; therefore, differences in the  $P-\rho$  plane were mostly due to density variations in their initial states. *SESAME* 7171 and *SESAME* 7180 are models for branched (polymer has other chains or branches stemming from the main chain backbone) and linear (polymer has atoms arranged in a chain-like struc-

Table 121.III: Polypropylene principal Hugoniot results from impedance matching with quartz reference. Measured shock velocity in the quartz and polypropylene,  $U_{sQ}$  and  $U_{sCH_2}$  is given with associated random error arising from measurement limitations.  $U_{pCH_2}$  (ran,sys),  $P_{CH_2}$  (ran,sys), and  $\rho_{CH_2}$  (ran,sys) are the resulting particle velocity, pressure, and density of shocked polypropylene obtained through the IM construct. Random errors enter the analysis through measurement uncertainties in  $U_{sQ}$  and  $U_{sCH_2}$ , while systematic errors emerge from uncertainties in the principal Hugoniot and release states of quartz.

Shot No.	$U_{sQ}$ ( $\mu\text{m/ns}$ )	$U_{sCH_2}$ ( $\mu\text{m/ns}$ )	$U_{pCH_2}$ (ran,sys) ( $\mu\text{m/ns}$ )	$P_{CH_2}$ (ran,sys) (Mbar)	$\rho_{CH_2}$ (ran,sys) (g/cc)
52798	12.14±0.14	14.07±0.11	7.64 (0.12, 0.14)	0.97 (0.02, 0.02)	1.97 (0.04, 0.04)
52797	14.89±0.14	17.2±0.13	10.5 (0.18, 0.22)	1.63 (0.03, 0.03)	2.31 (0.07, 0.08)
52628	15.42±0.1	17.83±0.12	11.11 (0.13, 0.23)	1.78 (0.02, 0.04)	2.38 (0.05, 0.08)
52796	17.65±0.13	20.72±0.1	13.44 (0.16, 0.12)	2.51 (0.03, 0.02)	2.56 (0.06, 0.04)
52631	17.78±0.16	20.74±0.25	13.59 (0.19, 0.12)	2.54 (0.04, 0.02)	2.61 (0.1, 0.05)
52634	21.38±0.1	25.55±0.11	17.05 (0.11, 0.2)	3.92 (0.03, 0.04)	2.71 (0.05, 0.06)
52633	26.42±0.11	31.69±0.12	22 (0.13, 0.33)	6.28 (0.04, 0.09)	2.94 (0.05, 0.1)

ture with no branches) polyethylene (same C-to-H ratio as polypropylene); these models were evaluated at polypropylene's initial density and compared with results.

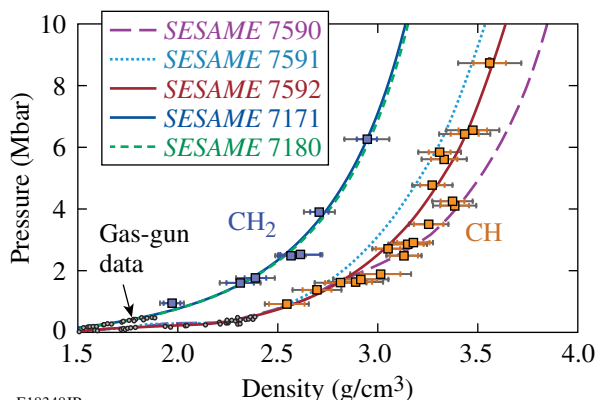
As shown in Figs. 121.10 and 121.11, the CH<sub>2</sub> data are in good agreement with both *SESAME* 7171 and *SESAME* 7180, which predict almost identical behavior in the  $P$ - $\rho$  plane. This



E18464JR

Figure 121.10

Principal Hugoniot data and models for CH<sub>2</sub> in the  $U_s$ - $U_p$  plane. Data for this study were taken on biaxially oriented polypropylene ( $C_3H_6$ )<sub>n</sub> with initial density  $\rho_0 = 0.9$  g/cc, using IM with quartz reference. Random uncertainties are shown as blue error bars and total uncertainties (quadrature sum of random and systematic errors) are shown as gray error bars. Previous gas-gun experiments from Marsh<sup>30</sup> are shown. Data are compared with *SESAME*<sup>38</sup> models for polyethylene ( $C_2H_4$ )<sub>n</sub> evaluated with initial density  $\rho_0 = 0.9$  g/cc.

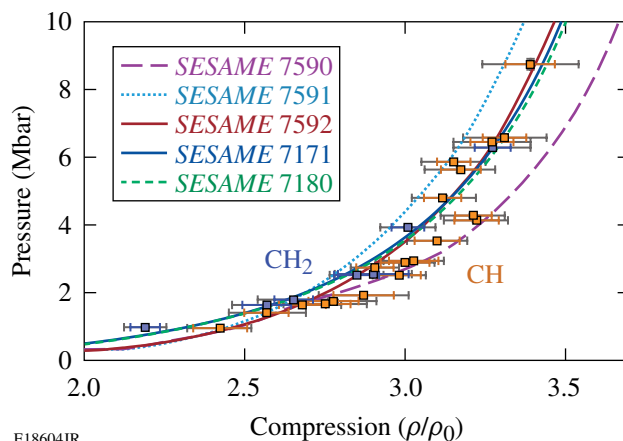


E18348JR

Figure 121.11

Principal Hugoniot data and models for CH<sub>2</sub> and CH in the  $P$ - $\rho$  plane (CH models and error bars as in previous figures). Data for CH<sub>2</sub> were taken on biaxially oriented polypropylene ( $C_3H_6$ )<sub>n</sub>, with initial density  $\rho_0 = 0.9$  g/cc, using IM with quartz reference. Random uncertainties are shown as blue error bars and total uncertainties (quadrature sum of random and systematic errors) are shown as gray error bars. Previous gas-gun experiments from Marsh<sup>30</sup> are shown. Data for CH<sub>2</sub> are compared with *SESAME*<sup>38</sup> models for polyethylene ( $C_2H_4$ )<sub>n</sub>, evaluated with initial density  $\rho_0 = 0.9$  g/cc.

is not entirely surprising since both models make similar physical assumptions with only slightly varying inputs. The electronic contribution was modeled the same way as the *SESAME* models for CH TFD with an exchange constant equal to 2/3. The ground electronic contribution (cold curve) was calculated from shock data and an assumption of a Mie-Grüneisen EOS, where the reference Grüneisen parameter was calculated in the same manner as in the CH *SESAME* models, leading to values 0.561 and 0.739 for *SESAME* 7171 and 7180, respectively. The reference Debye temperature was calculated from the  $U_s$ - $U_p$  intercept, average atomic weight, initial density, and a Poisson ratio of 1/3. The nuclear contribution was obtained via a solid-gas interpolation formula, which is in agreement with the Debye formula at low temperatures or high densities and approaches the ideal gas at high temperatures or low densities. Differences in the models arise from experimental Hugoniot data used to construct the cold curve and parameters derived from other experimental measurements, such as the reference Grüneisen coefficient and Debye temperature, used to compute the lattice vibrational contribution. The cohesive energies were set at 3.35 and 4 MJ/kg for *SESAME* 7171 and 7180, and binding energies resulting from cold-curve calculations differed by ~3%. The atomic number and atomic weight were assumed to be 8/3 and 4.6757, respectively.<sup>47,48</sup>



E18604JR

Figure 121.12

Principal Hugoniot measurements for CH and CH<sub>2</sub> in the  $P$ - $\eta$  plane using quartz as IM reference. Models and error bars as described in previous figures.

## Optical and Thermal Measurements

### 1. Reflectivity

The reflectivity of the observed shocks was determined by the signal level of the probe beam detected by the VISAR streak camera. The incident probe intensity was essentially constant over its pulse duration. That intensity was normalized using the detected levels produced by the  $\alpha$ -quartz pusher, whose

reflectivity as a function of shock velocity is known.<sup>18</sup> This leads to continuous records of reflectivity as a function of time for materials under study. However, the intensity profiles in CH showed an anomalous behavior: the detected intensity increased as the decaying shock transited the sample. This behavior was amplified with increasing pressure. This was the result of a “fogging” in the CH that attenuated the VISAR probe beam. X rays from the laser plasma were absorbed in the sample material, producing free electrons that can absorb light, although insufficient to produce noticeable preheat.<sup>49</sup> As the shock front (which was decaying in strength) moved through the CH, the VISAR probe beam passed through less-absorbing material, causing the streak cameras to register an increase in intensity signal levels, even though the shock was decaying. The anomalous behavior was observed in CH but not observed in CH<sub>2</sub> at low pressures, where the intensity decreased as a function of time, as expected. Anomalous behavior of CH<sub>2</sub> was observed only at the highest-pressure experiment. To account for this, reflectivity data were calculated only at the quartz–CH (CH<sub>2</sub>) interface. Here the quartz signal was attenuated by the same amount as the CH signal, and the normalization to the known quartz reflectivity held. To do this, the intensity returned from the shocked pusher (quartz) and polymer was linearly fit and extrapolated to the contact interface. The reflected intensities and the known reflectivity of quartz (as a function of shock velocity) provided reflectance measurements for the hydrocarbons. For CH, this led to one data point  $R(U_s)$ , translated to  $R(P)$ , having knowledge of the pressure obtained from a corresponding CH shock/velocity value via IM. Continuous  $R(U_s)$  measurements were obtained for CH<sub>2</sub> at low pressures, but for precaution, only reflectivities at the contact interface were used, resulting in one  $R(P)$  data point; this also translates to temperature measurements since they are dependent on measured reflectance. The reflectivity of CH and CH<sub>2</sub> as a function of pressure is shown in Fig. 121.13. Errors in reflectivity varied from 31% at the lowest pressure to 9% at the highest pressure for CH and from 25% to 15% from lowest to highest pressure for CH<sub>2</sub>. At higher pressures, there was a better signal-to-noise ratio since the shocked hydrocarbons became better reflectors. Low-pressure measurements in the hydrocarbons corresponded to pressures of 1 to 2 Mbar in quartz, close to its melt onset. At these pressures, quartz is barely reflective and the reflected intensity measurements are less accurate.

Both CH and CH<sub>2</sub> underwent a drastic increase in reflectivity at around 1 Mbar and saturated at ~40%. This occurred at 2.5 to 3 Mbar for both materials. This behavior—steep reflectivity increase and saturation—is often seen in materials undergoing an insulator–conductor transition.<sup>50–52</sup>

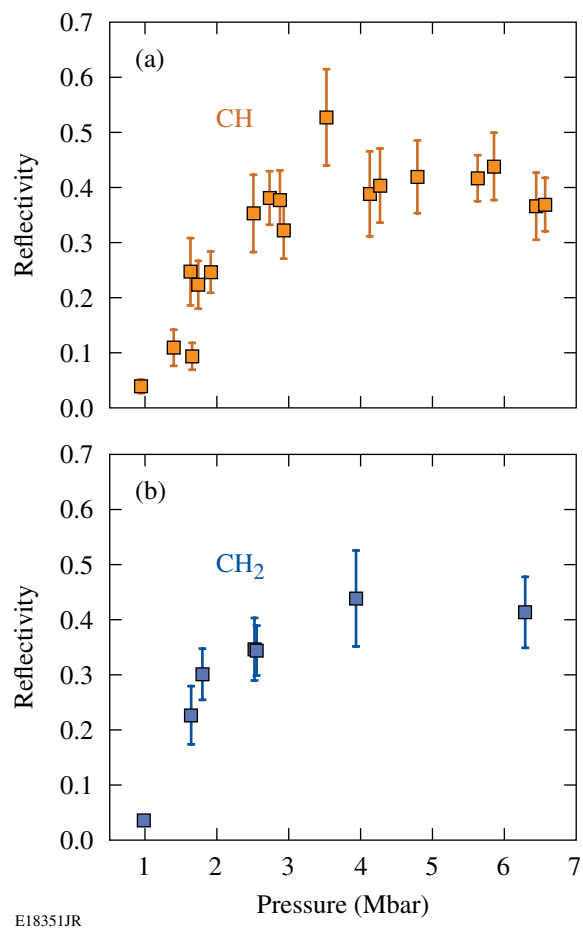


Figure 121.13 Reflectivity measurements from VISAR signal and quartz known reflectivity for (a) polystyrene and (b) polypropylene, where saturation occurs at 40% for both materials.

Polystyrene’s optical properties have been previously studied by Koenig *et al.*<sup>53</sup> with CH shock velocities of 11 to 16  $\mu\text{m/ns}$  (~0.8 to 1.7 Mbar), where they observed steadily increasing reflectivities reaching values up to 50%, well above our measurements. In that same pressure range, we observed smaller reflectivities, <25%. The reflectivity of shocked CH was also measured by Ozaki *et al.*<sup>10</sup> who found reflectivities from 16% to 42% in the CH shock-velocity range of ~22 to 27  $\mu\text{m/ns}$  (~3 to 5 Mbar), in better agreement with our findings.

Discrepancies in reflectivities between studies could arise from differences in diagnostic configurations or from probe-beam stability. Reflectivity measurements in these studies are relative measurements since reflected intensities between a standard material and sample are compared and “normalized” with known reflectivities of the unshocked or shocked standard. If the probe-beam stability is compromised either temporally

or spatially and the analysis does not correct for it, this could yield biased reference reflectivities. In these experiments a reference image of the returned probe intensity is acquired on each shot. These were used to monitor deviations in the incident probe-beam intensity, which were quite small.

## 2. Temperature

The brightness temperatures of the shocks were determined from spectral radiance intensities detected by the SOP with a wavelength range of 590 to 900 nm, with a centroid wavelength of 682 nm (Ref. 28). Recorded SOP intensities were modeled assuming a gray-body Planckian spectrum given by

$$L(\lambda, T) = \varepsilon(\lambda) \frac{2hc^2}{\lambda^5} \frac{1}{e^{hc/\lambda T} - 1},$$

where  $\varepsilon$  is the emissivity,  $h$  is Planck's constant,  $c$  is the speed of light,  $\lambda$  is the radiation wavelength, and  $T$  is the temperature of a Planckian radiator.

The emissivity is given by  $1-R(\lambda)$ , where  $R(\lambda)$  is the reflectivity that is assumed to vary only slightly as a function of wavelength in the optical spectral range, such that  $R(\lambda)$  is the same optical reflectivity measured by VISAR at 532 nm. As described in **Reflectivity** (p. 16), reflectivity values were obtained by linearly fitting the VISAR intensities and extrapolating to the contact interface, avoiding attenuation effects of the VISAR probe beam in polystyrene. Consequently the recorded SOP spectral intensities emitted by the shocked polymer were linearly fit over a time interval of  $\sim 500$  to 600 ps and extrapolated to a time corresponding to that of the contact interface, such that obtained reflectivity measurements could be used for emissivity calculations. This implies that SOP measurements were taken close to the quartz–glue–CH boundary. SOP has a temporal resolution of  $\sim 170$  ps; therefore, the self-emission from the shock front is integrated over this time interval. At material boundaries, the recorded SOP intensity could be the integrated signal from different materials. Large time intervals were chosen to linearly fit the SOP data with this in mind. Material boundaries on SOP records are not easily identified (as on VISAR records); therefore, care was taken to choose/define the beginning of a material region, containing a signal for such material, only after the SOP signal had recovered from observable spectral-intensity changes.

Having observed absorption of the VISAR probe beam in CH (at all pressures) and CH<sub>2</sub> (at the highest pressure only), there was concern that spectral intensities as recorded by SOP

were affected as well. To account for this, the sample temperatures were normalized to the quartz. Quartz reflectivity and temperature as functions of pressure (shock velocity) have been previously studied.<sup>16</sup> Since the quartz and polymer signal in the SOP diagnostic are subject to the same conditions (optical path, camera sensitivity, and resulting spectral response of the diagnostic), one can re-derive the equation for the temperatures in the sample by substituting diagnostic constants with the quartz's observed temperature and emissivity. The resulting sample temperatures are relative temperatures since they are referenced, or normalized, to the quartz's known shock Hugoniot thermal and optical behavior.

Tables 121.IV and 121.V list the brightness and normalized temperatures for CH and CH<sub>2</sub>, respectively. The brightness temperatures are those derived simply from the measured spectral intensity and the SOP calibration. The normalized temperatures use the observed brightness of the quartz shock plus its velocity to provide a normalization that is applied to the CH and CH<sub>2</sub> results. On average, normalized temperatures for CH were  $\sim 1.3\times$  larger than those measured using CH SOP intensities only; for CH<sub>2</sub> that factor was  $\sim 1.1$ . [It should be noted that two shots (52628 and 52631), each simultaneously studying both CH and CH<sub>2</sub>, showed brightness temperatures that were higher than shots at similar conditions. When normalized to quartz, those temperatures had negligible changes. This suggests that for some reason these two shots did not experience fogging in the samples.]

Table 121.IV: Hugoniot temperatures for polystyrene as obtained using reflectivity and SOP spectral intensities for each shot. Relative temperatures, normalized to quartz, show that polystyrene's behavior also affects SOP spectral intensities.

Shot No.	$T$ (eV)	$T_{\text{normalized}}$ (eV)
52795	0.43±0.05	0.51±0.05
52800	0.59±0.03	1.06±0.07
52793	0.70±0.06	0.88±0.10
52464	0.63±0.07	1.01±0.13
52628	1.22±0.06	1.19±0.06
52792	1.05±0.08	1.39±0.17
52631	1.97±0.21	1.95±0.18
52799	1.38±0.09	1.79±0.17
52791	1.75±0.32	2.50±0.57
52634	2.25±0.35	2.84±0.43
52633	4.29±0.52	5.57±0.62

Table 121.V: Hugoniot temperatures for polypropylene as obtained using the reflectivity and SOP spectral intensities for each shot. Relative temperatures, normalized to quartz, were also obtained.

Shot No.	$T$ (eV)	$T_{\text{normalized}}$ (eV)
52798	$0.46 \pm 0.06$	$0.53 \pm 0.05$
52797	$0.70 \pm 0.05$	$0.81 \pm 0.08$
52628	$1.02 \pm 0.06$	$1.05 \pm 0.08$
52796	$0.95 \pm 0.06$	$1.15 \pm 0.11$
52631	$1.44 \pm 0.09$	$1.42 \pm 0.13$
52634	$2.18 \pm 0.40$	$2.42 \pm 0.43$
52633	$3.86 \pm 0.59$	$5.01 \pm 0.81$

Figure 121.14 shows normalized temperatures for polystyrene [orange points in (a)] and polypropylene [blue points in (b)]. Temperature errors were between 5% and 22% for CH and 8% and 18% for CH<sub>2</sub>; these errors stemmed from system calibration and measurements of self-emission and reflectivity in each hydrocarbon. Quartz parameters for normalization were taken from a fit to the data in Ref. 16. The various *SESAME* models available for CH and CH<sub>2</sub> predict similar thermal behavior for both materials: both materials reach comparable temperatures from ~1 to 7 Mbar. The models predict similar shock temperatures that all agree fairly well with measurements over that range. The models are similar enough to each other that the data, with their moderate precision, do not favor any one of the models. CH temperatures at 3 to 5 Mbar by Ozaki *et al.*<sup>10</sup> [green points in Fig. 121.14(a)] are consistent with these data.

## Conclusions

The equation of state was measured for two hydrocarbons at shock pressures of 1 to 10 Mbar. A time-resolved VISAR diagnostic provided precise (~1%) measurement of shock velocity in the transparent standard and sample materials. The use of experimental data for the Hugoniot of the quartz pusher made it possible to determine the systematic errors in the IM technique for the derived quantities. These data are the most-precise measurements of the EOS of hydrocarbons performed at these high pressures ( $\geq 1$  Mbar).

Polystyrene (CH) was observed to compress by 2.5 $\times$  to ~3.5 $\times$  at pressures of 1 to 10 Mbar. This behavior was predicted by the *SESAME* 7592 model. Polystyrene exhibits slightly greater compressibility (compared to *SESAME* 7592) in the 2- to 4-Mbar range. Previous results from other researchers showed much stiffer behavior, most likely due to preheating of those samples.

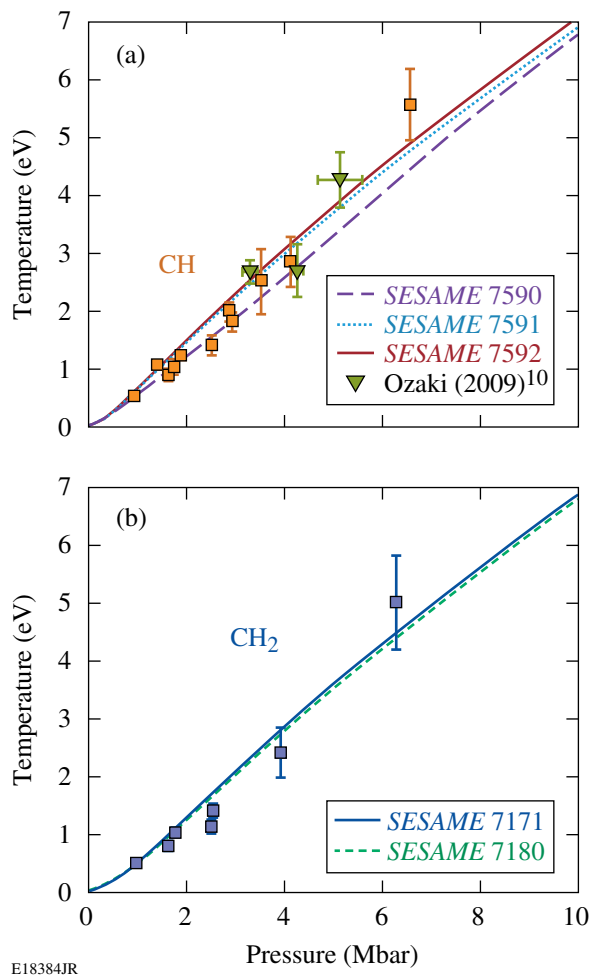


Figure 121.14  
Temperature measurements were calculated from SOP self-emission records, fitted to a gray-body Planckian radiator, where emissivity was obtained from reflectivity measurements from VISAR, and normalized using the known quartz temperature and reflectivity. Both (a) polystyrene and (b) polypropylene reach similar temperatures with increasing pressure.

Polypropylene (CH<sub>2</sub>) was observed to compress by similar amounts over a similar range of pressures. Two *SESAME* models (7171 and 7180) reproduced the behavior well (in this pressure range, the two models for polypropylene were nearly indistinguishable). This agreement for both materials suggests that the effect of the C-to-H ratio is properly accounted for in these models for polystyrene and polypropylene.

Reflectivity measurements indicated that both polystyrene and polypropylene become reflective when shocked to 1 to 2 Mbar. Above 3 Mbar, shock waves in both materials have a reflectivity of ~40%. This behavior is typical of materials that undergo a shock-induced transition from an insulator to a conductor.

The measured intensity of the self-emission from these shocks, normalized to known temperatures in quartz, was used to infer the brightness temperature of shocks in the two materials. Reflectivity measurements were used to infer gray-body brightness temperatures of the shock waves. The results show that both polystyrene and polypropylene are heated to 0.5 to 5 eV by shock pressures of  $\sim 1$  to 6 Mbar. The shock temperatures in each material are well predicted by the *SESAME* models, but the models are so similar that no model is favored. Normalized temperatures showed consistent differences from brightness temperatures, and it was concluded that partial blanking of the SOP diagnostic occurred. This was evident in the CH at all pressures and only at the highest pressure for CH<sub>2</sub>.

These results are significant in that they provide high-precision kinematic and thermal data for two hydrocarbons shocked to 1 to 10 Mbar, providing a complete EOS of those materials. The polystyrene data indicate that this material does not stiffen at high pressures (as suggested by earlier experiments), and the polypropylene data show that the effect of the C-to-H ratio is reasonably predicted by the models. These results are particularly important to the design of ICF targets for the NIF, which will use similar hydrocarbon ablaters that are compressed by multiple shocks in this pressure region. Similarly, the behavior of hydrocarbons shocked to  $\sim 10$  Mbar is important to general studies of high-energy-density physics.

#### ACKNOWLEDGMENT

This work was supported by the U.S. Department of Energy Office of Inertial Confinement Fusion under Cooperative Agreement No. DE-FC52-08NA28302, the University of Rochester, and the New York State Energy Research and Development Authority. The support of DOE does not constitute an endorsement by DOE of the views expressed in this article.

#### REFERENCES

1. D. G. Hicks, T. R. Boehly, P. M. Celliers, J. H. Eggert, E. Vianello, D. D. Meyerhofer, and G. W. Collins, *Phys. Plasmas* **12**, 082702 (2005).
2. D. G. Hicks, T. R. Boehly, P. M. Celliers, D. K. Bradley, J. H. Eggert, R. S. McWilliams, R. Jeanloz, and G. W. Collins, *Phys. Rev. B* **78**, 174102 (2008).
3. D. G. Hicks, T. R. Boehly, P. M. Celliers, J. H. Eggert, S. J. Moon, D. D. Meyerhofer, and G. W. Collins, *Phys. Rev. B* **79**, 014112 (2009).
4. J. D. Lindl *et al.*, *Phys. Plasmas* **11**, 339 (2004).
5. S. W. Haan *et al.*, *Phys. Plasmas* **2**, 2480 (1995).
6. S. W. Haan *et al.*, *Phys. Plasmas* **12**, 056316 (2005).
7. S. W. Haan *et al.*, *Eur. Phys. J. D* **44**, 249 (2007).
8. R. Cauble *et al.*, *Phys. Plasmas* **4**, 1857 (1997).
9. N. Ozaki *et al.*, *Phys. Plasmas* **12**, 124503 (2005).
10. N. Ozaki *et al.*, *Phys. Plasmas* **16**, 062702 (2009).
11. T. R. Boehly, D. H. Munro, P. M. Celliers, R. E. Olson, D. G. Hicks, V. N. Goncharov, G. W. Collins, H. F. Robey, S. X. Hu, J. A. Marozas, T. C. Sangster, O. L. Landen, and D. D. Meyerhofer, *Phys. Plasmas* **16**, 056302 (2009).
12. G. R. Moore and D. E. Kline, *Properties and Processing of Polymers for Engineers* (Prentice-Hall, Englewood Cliffs, NJ, 1984).
13. F. H. Ree, *J. Chem. Phys.* **70**, 974 (1979).
14. W. J. Nellis *et al.*, *J. Chem. Phys.* **80**, 2789 (1984).
15. W. J. Nellis, D. C. Hamilton, and A. C. Mitchell, *J. Chem. Phys.* **115**, 1015 (2001).
16. D. G. Hicks, T. R. Boehly, J. H. Eggert, J. E. Miller, P. M. Celliers, and G. W. Collins, *Phys. Rev. Lett.* **97**, 025502 (2006).
17. T. R. Boehly, J. E. Miller, D. D. Meyerhofer, J. G. Eggert, P. M. Celliers, D. G. Hicks, and G. W. Collins, in *Shock Compression of Conducted Matter—2007*, edited by M. Elert *et al.* (American Institute of Physics, Melville, NY, 2007), Vol. 955, pp. 19–22.
18. S. Brygoo, D. G. Hicks, P. Loubeyre, J. H. Eggert, S. McWilliams, P. M. Celliers, T. R. Boehly, R. Jeanloz, and G. W. Collins, "Development of Melted Quartz as an Impedance-Matching Standard for Strong Laser Shock Measurements," to be published in the *Journal of Applied Physics*.
19. T. R. Boehly, R. S. Craxton, T. H. Hinterman, J. H. Kelly, T. J. Kessler, S. A. Kumpan, S. A. Letzring, R. L. McCrory, S. F. B. Morse, W. Seka, S. Skupsky, J. M. Soures, and C. P. Verdon, *Rev. Sci. Instrum.* **66**, 508 (1995).
20. Y. Lin, T. J. Kessler, and G. N. Lawrence, *Opt. Lett.* **20**, 764 (1995).
21. Ya. B. Zel'dovich and Yu. P. Raizer, in *Physics of Shock Waves and High-Temperature Hydrodynamic Phenomena*, edited by W. D. Hayes and R. F. Probstein (Dover Publications, Mineola, NY, 2002), Vol. I, Chap. I, pp. 1–104.
22. R. P. Drake, *High-Energy-Density Physics: Fundamentals, Inertial Fusion, and Experimental Astrophysics*, Shock Wave and High Pressure Phenomena (Springer, Berlin, 2006).
23. P. M. Celliers, D. K. Bradley, G. W. Collins, D. G. Hicks, T. R. Boehly, and W. J. Armstrong, *Rev. Sci. Instrum.* **75**, 4916 (2004).
24. P. M. Celliers *et al.*, *Appl. Phys. Lett.* **73**, 1320 (1998).
25. L. M. Barker and R. E. Hollenbach, *J. Appl. Phys.* **43**, 4669 (1972).
26. L. M. Barker and K. W. Schuler, *J. Appl. Phys.* **45**, 3692 (1974).

27. P. A. Jaanimagi, R. Boni, D. Butler, S. Ghosh, W. R. Donaldson, and R. L. Keck, in *26th International Congress on High-Speed Photography and Photonics*, edited by D. L. Paisley *et al.* (SPIE, Bellingham, WA, 2005), Vol. 5580, pp. 408–415.
28. J. E. Miller, T. R. Boehly, A. Melchior, D. D. Meyerhofer, P. M. Celliers, J. H. Eggert, D. G. Hicks, C. M. Sorce, J. A. Oertel, and P. M. Emmel, *Rev. Sci. Instrum.* **78**, 034903 (2007).
29. G. A. Lyzenga, T. J. Ahrens, and A. C. Mitchell, *J. Geophys. Res. B* **88**, 2431 (1983).
30. S. P. Marsh, ed. *LASL Shock Hugoniot Data*, Los Alamos Series on Dynamic Material Properties (University of California Press, Berkeley, CA, 1980).
31. R. F. Trunin *et al.*, *Izv. Acad. Sci. USSR Phys. Solid Earth*, **8** (1971).
32. R. F. Trunin, *Phys.-Usp.* **37**, 1123 (1994).
33. Recent work on the Sandia Z Machine by Knudson, first presented at 16th Topical Conference on Shock Compression of Condensed Matter, measured Hugoniot and sound speed of  $\alpha$ -quartz in the 1- to 16-Mbar regime, observing some curvature in  $U_s(U_p)$ . [M. Knudson and M. Desjarlais, presented at the 16th APS Topical Conference on Shock Compression of Condensed Matter, Nashville, TN, 28 June–3 July 2009 (Paper V2.00001); M. Knudson, *Bull. Am. Phys. Soc.* **54**, 134 (2009).] If real, this can cause shifts in the data obtained using  $\alpha$ -quartz as an IM standard, although it does not compromise the precision of the data presented in this article. To resolve this, measurement of the Mie–Grüneisen parameter using laser-driven shock waves is currently underway. The data presented here will be reanalyzed with this new data in a future publication. The percent difference in density between the fit found by Knudson and that used in this study varies with quartz shock velocity, peaking around 19 to 20 km/s (6 to 7 Mbar) at ~6% and decreasing with increasing shock velocity and pressure. This implies that values would be most compromised only in these ranges, and data obtained at higher pressures would be less affected.
34. R. G. McQueen, Los Alamos National Laboratory, Los Alamos, NM, LA-UR-90-1996 (1989).
35. R. F. Trunin, *Shock Compression of Condensed Materials* (Cambridge University Press, Cambridge, England, 1998).
36. A. N. Mostovych *et al.*, *Phys. Plasmas* **8**, 2281 (2001).
37. T. R. Boehly, D. G. Hicks, P. M. Celliers, T. J. B. Collins, R. Earley, J. H. Eggert, D. Jacobs-Perkins, S. J. Moon, E. Vianello, D. D. Meyerhofer, and G. W. Collins, *Phys. Plasmas* **11**, L49 (2004).
38. S. P. Lyon and J. D. Johnson, Los Alamos National Laboratory, Los Alamos, NM, Report LA-CP-98-100 (1998).
39. N. C. Holmes, *Rev. Sci. Instrum.* **62**, 1990 (1991).
40. I. P. Dudoladov *et al.*, *Prikl. Mekh. Tekh. Fiz.* **4**, 148 (1969).
41. R. G. McQueen *et al.*, in *High-Velocity Impact Phenomena*, edited by R. Kinslow (Academic Press, New York, 1970), Chap. VII, Sec. II, pp. 293–417.
42. M. Van Thiel, J. Shaner, and E. Salinas, Lawrence Livermore National Laboratory, Livermore, CA, Report UCRL-50108, Rev. 1 (1977).
43. A. V. Bushman *et al.*, *JETP Lett.* **82**, 895 (1996).
44. J. Abdallah, Jr., Los Alamos National Laboratory, Los Alamos, NM, Report LA-10244-M, NTIS Order No. DE85001405 (1984). (Copies may be obtained from the National Technical Information Service, Springfield, VA 22161.)
45. G. I. Kerley, Sandia National Laboratory, Albuquerque, NM, Report SAND-88-2291, NTIS Order No. DE91017717 (1991). (Copies may be obtained from the National Technical Information Service, Springfield, VA 22161.)
46. R. Cauble (Lawrence Livermore National Laboratory) and N. Ozaki (Osaka University), private communication (2009).
47. F. Dowell, Los Alamos National Laboratory, Los Alamos, NM, Report LA-9559-MS, NTIS Order No. DE83003896 (1982). (Copies may be obtained from the National Technical Information Service, Springfield, VA 22161.)
48. F. Dowell, Los Alamos National Laboratory, Los Alamos, NM, Report LA-9564-MS, NTIS Order No. DE83004996 (1982). (Copies may be obtained from the National Technical Information Service, Springfield, VA 22161.)
49. W. Theobald, J. E. Miller, T. R. Boehly, E. Vianello, D. D. Meyerhofer, T. C. Sangster, J. Eggert, and P. M. Celliers, *Phys. Plasmas* **13**, 122702 (2006).
50. D. K. Bradley *et al.*, *Phys. Rev. Lett.* **93**, 195506 (2004).
51. P. M. Celliers *et al.*, *Phys. Rev. Lett.* **84**, 5564 (2000).
52. P. M. Celliers *et al.*, *Phys. Plasmas* **11**, L41 (2004).
53. M. Koenig *et al.*, *Phys. Plasmas* **10**, 3026 (2003).

# A Generalized Measurable Ignition Condition for Inertial Confinement Fusion

In inertial confinement fusion (ICF),<sup>1</sup> a shell of cryogenic deuterium and tritium (DT) thermonuclear fuel is accelerated inward by direct laser irradiation or by the x rays produced by heating a high-Z enclosure (hohlraum). At stagnation, the compressed fuel is ignited by a central hot spot surrounded by a cold, dense shell. Ignition occurs when the alpha-particle heating of the hot spot exceeds all the energy losses. To measure progress toward ignition, a metric is needed to assess how an implosion experiment performs with respect to the ignition condition. In a stationary plasma, the ignition condition is given by the Lawson criterion.<sup>2</sup> In ICF, the same ignition condition must be derived in terms of measurable parameters. Different forms of the 1-D ignition condition have been derived,<sup>1,3,4</sup> but none of them can be accurately measured. Measurable parameters of the ICF fuel assembly are the areal density, the ion temperature, and the neutron yield. This article demonstrates that the ICF ignition condition can be written in terms of these measurable parameters. We start from the 1-D ignition model of Ref. 5 and generalize it to multidimensions through a single parameter: the yield-over-clean (YOC). The YOC is the ratio of the measured neutron yield to the predicted 1-D yield. The latter must be calculated consistently with the measured  $\rho R$  and  $T_i$ . The generalized ignition criterion depends on the areal density, the ion temperature, and the YOC. Alternatively, the ignition condition can be written in terms of the areal density, the neutron yield, and the target mass.

This article first deals with the 3-D extension of the dynamic ignition model<sup>5,6</sup> and an analytic ignition condition. The results of hydrodynamic simulations of imploding capsules forming the database used to generate a more-accurate ignition condition will also be shown. A measurable criterion requires the solution of a dynamic ignition model. The analysis starts by modifying the 1-D ignition model [Eq. (15) of Ref. 5] and the following considerations about multidimensional effects: The hot spot is enclosed by a surrounding shell that can be highly distorted by hydrodynamic instabilities. The hot-spot volume  $V_{hs}$  is bounded by Rayleigh–Taylor (RT) bubbles and spikes from the shell. The plasma in the bubbles is cold and does not contribute to the fusion yield. Following the analysis of Ref. 7,

we assume that only the “clean” hot-spot volume  $V_{clean}$  within the RT spikes (Fig. 121.15) is hot enough to induce fusion reactions, and the central temperature is unchanged by the RT evolution as long as the RT spikes do not reach the hot spot’s center. The 1-D ignition model can be extended to 3-D by integrating the alpha-particle energy deposition over the clean hot-spot volume, leading to

$$\frac{d}{d\tau}(\hat{P}\hat{R}^3) = -2\hat{P}\hat{R}^2 \frac{d\hat{R}}{d\tau} + \gamma_\alpha \hat{P}^2 \hat{T}\hat{R}_{clean}^3, \quad (1)$$

$$\frac{d}{d\tau} \left( \frac{\hat{P}\hat{R}^3}{\hat{T}} \right) = \hat{R}\hat{T}^{5/2}, \quad (2)$$

$$\frac{d^2\hat{R}}{d\tau^2} = \hat{P}\hat{R}^2. \quad (3)$$

With respect to the 1-D case, the alpha heating is reduced by the clean volume fraction  $R_{clean}^3/R^3$ , where  $R_{clean}$  and  $R$  are

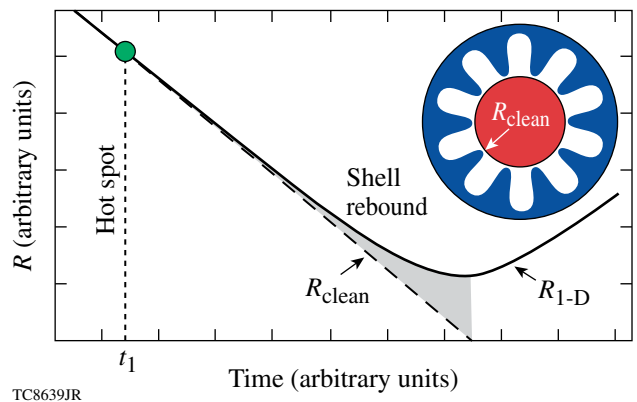


Figure 121.15 Schematic of the free-fall model. Fusion reactions occur only in the clean volume within the Rayleigh–Taylor spikes. The spikes “free-fall” after saturation of the linear growth.

the clean and 1-D radii, respectively. We assume this to be the main effect of the implosion nonuniformities. In Eqs. (1)–(3), the hot-spot radius  $R$ , pressure  $P$ , and central temperature  $T$  are normalized with their stagnation values calculated without including the alpha-particle energy deposition  $R_{\text{stag}}^{\text{no } \alpha}$ ,  $P_{\text{stag}}^{\text{no } \alpha}$ , and  $T_*^{\text{no } \alpha}$  defined later. The dimensionless time  $\tau = tV_i/R_{\text{stag}}^{\text{no } \alpha}$  is a function of the implosion velocity  $V_i$ . Equations (1)–(3) represent the hot-spot energy balance, the temperature equation from the hot-spot mass conservation, and the thin-shell Newton’s law, respectively. For simplicity, we have neglected the radiation losses (included in Ref. 5) in the derivation but retained in the simulation. The expansion [first term on the right-hand side of Eq. (1)] and the heat-conduction losses [right-hand side of Eq. (2)] are retained. This article focuses on the 3-D effects included in the term  $R_{\text{clean}}$  in Eq. (1). The term  $\gamma_\alpha$  governs the ignition conditions and can be written as

$$\gamma_\alpha = \left( \varepsilon_\alpha C_0 P_{\text{stag}}^{\text{no } \alpha} R_{\text{stag}}^{\text{no } \alpha} T_*^{\text{no } \alpha} \right) / (8 V_i), \quad (4)$$

where  $\varepsilon_\alpha$  is the alpha-particle energy (3.5 MeV) and  $C_0 \simeq 2.5 \times 10^{-26} \text{ m}^3 \text{ keV}^{-3} \text{ s}^{-1}$  comes from approximating the volume integral of the fusion rate around a 4- to 15-keV central temperature with a power law  $\sim T^3$ . The initial conditions are defined at the time of peak implosion velocity  $V_i$ :  $P(0) = P_0$ ,  $R(0) = R_0$ ,  $\dot{R}(0) = -V_i$ , and  $T(0) = T_0$ . The stagnation values  $R_{\text{stag}}^{\text{no } \alpha}$ ,  $P_{\text{stag}}^{\text{no } \alpha}$ , and  $T_{\text{stag}}^{\text{no } \alpha}$  are obtained by solving the dimensional form of Eqs. (1)–(3) without alpha-particle–energy deposition ( $\gamma_\alpha = 0$ ) and in the limit of large initial kinetic energy  $\epsilon_0 = (M_{\text{shell}} V_i^2 / 4\pi P_0 R_0^3) \gg 1$ . This leads to the following stagnation values without alphas:

$$P_{\text{stag}}^{\text{no } \alpha} \simeq P_0 \epsilon_0^{5/2}, \quad R_{\text{stag}}^{\text{no } \alpha} \simeq R_0 \epsilon_0^{-1/2}, \quad (5)$$

$$T_*^{\text{no } \alpha} \simeq \left( 1.2 P_{\text{stag}}^{\text{no } \alpha} R_{\text{stag}}^{\text{no } \alpha} V_i / \kappa_0 \right)^{2/7}, \quad (6)$$

where  $T_*^{\text{no } \alpha} \simeq 1.3 T_{\text{stag}}^{\text{no } \alpha}$  and  $\kappa_0 \simeq 3.7 \times 10^{69} \text{ m}^{-1} \text{ s}^{-1} \text{ J}^{-5/2}$  is the coefficient of Spitzer thermal conductivity  $\kappa_{\text{Sp}} \simeq \kappa_0 T^{5/2}$  for  $\ln \Lambda \simeq 5$ . Using the no- $\alpha$  stagnation values, the initial conditions of the dimensionless model are rewritten in the simple form  $\hat{P}(0) = \epsilon_0^{-5/2}$ ,  $\hat{T}(0) = \epsilon_0^{-1/2}$ ,  $\hat{R}(0) = \epsilon_0^{-1/2}$ , and  $\hat{\dot{R}}(0) = -1$ . The ignition model comprises Eqs. (1)–(3) and the initial conditions. Ignition is defined by the critical value of the parameter  $\gamma_\alpha$  in Eq. (1), yielding an explosive singular solution. In the limit of  $\epsilon_0 \rightarrow \infty$ , the critical value of  $\gamma_\alpha$  depends solely on the effect of nonuniformities entering through the clean radius  $R_{\text{clean}}$ . In the absence of nonuniformities (1-D),  $R_{\text{clean}} = R$  and the critical value of  $\gamma_\alpha$  is  $\gamma_\alpha$  (1-D)  $\simeq 1.1$ . As the alpha heating raises the

hot-spot temperature, the RT spikes are ablated by the enhanced heat flux as well as by the alpha particles leaking from the hot spot and depositing their energy onto the spikes.<sup>8</sup> This causes the ablative stabilization of the RT and an enhancement of the clean volume. This effect can be heuristically included by letting the clean radius increase up to the 1-D radius as the hot-spot temperature rises above the no- $\alpha$  value.

The aim of the new ignition model is to identify a measurable parameter describing the effects of hot-spot nonuniformities entering through the time history of the clean radius  $R_{\text{clean}}(\tau)$ . The RT spikes first grow exponentially until reaching a saturation amplitude. After saturation, the spikes free-fall into the hot spot as shown in Fig. 12.15; the acceleration  $g(t) = R''(t)$  determines the linear growth rates  $\gamma_{\text{RT}} = \sqrt{k g(t)}$ , where  $k \sim \ell/R(t)$  is the perturbation wave number. The number of  $e$  foldings of linear growth is

$$n_e = \sqrt{\ell} \hat{n}_e = \int_0^{t_{\text{lin}}} \gamma_{\text{RT}}(t) dt,$$

where  $t_{\text{lin}}$  is the interval of linear growth up to saturation. In the nonlinear free-fall stage, the spikes’ amplitude grows as

$$\Delta R \approx \eta(t_{\text{lin}}) + \int_{t_{\text{lin}}}^t dt' \int_{t_{\text{lin}}}^{t'} g(t'') dt'',$$

where  $\eta(t_{\text{lin}})$  is the linear amplitude at saturation. For simplicity, we assume that the linear growth can be neglected [small  $\eta(t_{\text{lin}})$ ] with respect to the nonlinear growth so that the spike amplitude  $\Delta R$  depends only on  $t_{\text{lin}}$  and  $t$ . This leads to a clean radius  $R_{\text{clean}} = R - \Delta R = R(t_{\text{lin}}) + R'(t_{\text{lin}})(t - t_{\text{lin}})$  for  $t > t_{\text{lin}}$ . Before  $t_{\text{lin}}$ , the clean radius equals the 1-D radius,  $R_{\text{clean}} \simeq R$ . The time  $t_{\text{lin}}$  depends on the amplitude of the inner DT-ice roughness at the end of the acceleration phase. The larger the initial nonuniformity level, the smaller the time  $t_{\text{lin}}$ . We first solve Eqs. (1)–(3) without alpha-particle–energy deposition and compute  $\hat{R}^{\text{no } \alpha}(\tau)$ . Then we use  $\hat{R}^{\text{no } \alpha}$  to determine  $\hat{R}_{\text{clean}}$  using the free-fall model. The most-severe reduction of the clean volume corresponds to  $\tau_{\text{lin}} = 0$ , when the nonlinear RT growth starts from the beginning of the deceleration phase. The number of  $e$  foldings of linear growth is directly proportional to

$$\hat{n}_e^{\text{no } \alpha} \simeq \frac{\pi}{2} + \arctan \left( \sqrt{\epsilon_0} - \frac{\epsilon_0}{\tau_{\text{lin}}} \right). \quad (7)$$

For a given  $\tau_{\text{lin}}$ , we compute  $\hat{n}_e^{\text{no } \alpha}$ ,  $R_{\text{clean}}(\tau, \tau_{\text{lin}})$ , and the yield-over-clean without alphas (YOC<sup>no } \alpha</sup>):

$$\text{YOC}^{\text{no } \alpha} = \frac{\int_0^\infty \hat{p}^2 \hat{T} \hat{R}_{\text{clean}}^3 d\tau}{\int_0^\infty \hat{p}^2 \hat{T} \hat{R}^3 d\tau}, \quad (8)$$

where  $\hat{p}$ ,  $\hat{T}$ , and  $\hat{R}$  are the solutions of Eqs. (1)–(3) without alpha-particle–energy deposition (i.e.,  $\gamma_\alpha = 0$ ). The  $\text{YOC}^{\text{no } \alpha}$  is the ratio of the neutron yield for a reduced clean volume to the 1-D neutron yield for the case without alphas. Both  $\text{YOC}^{\text{no } \alpha}$  and  $\hat{n}_e^{\text{no } \alpha}$  depend on  $\tau_{\text{lin}}$ , and a relation can be numerically derived, yielding the functional relation  $\hat{n}_e^{\text{no } \alpha} = \hat{n}_e^{\text{no } \alpha}(\text{YOC}^{\text{no } \alpha})$ . Since  $\hat{n}_e^{\text{no } \alpha}$  is a measure of the initial nonuniformities,  $\text{YOC}^{\text{no } \alpha}$  can also be used to define the initial nonuniformities' level. For a given value of  $\text{YOC}^{\text{no } \alpha}$ , it is possible to determine the ignition condition, including the effects of nonuniformities, by solving Eqs. (1)–(3) with alpha deposition for the corresponding clean radius  $\hat{R}_{\text{clean}}$  and by varying  $\gamma_\alpha$  to find the critical value for a singular solution. We start by determining the transition time  $\tau_{\text{lin}}$  from linear to nonlinear growth by solving Eqs. (1)–(3) with  $\hat{R}_{\text{clean}} \approx \hat{R}$  (valid in the linear regime) and a given value of  $\gamma_\alpha$ . The resulting radius  $R^\alpha(\tau)$  is used to compute the linear  $e$  foldings:

$$\hat{n}_e^\alpha(\tau_{\text{lin}}) = \int_0^{\tau_{\text{lin}}} \sqrt{R^{\alpha''}/R^\alpha} d\tau. \quad (9)$$

This is used to determine the time  $\tau_{\text{lin}}$  by setting

$$\hat{n}_e^\alpha(\tau_{\text{lin}}) = \hat{n}_e^{\text{no } \alpha}(\text{YOC}^{\text{no } \alpha}),$$

leading to a functional relation  $\tau_{\text{lin}} = \tau_{\text{lin}}(\text{YOC}^{\text{no } \alpha})$ . Using  $\tau_{\text{lin}}$ , the clean radius history follows from

$$\hat{R}_{\text{clean}}^\alpha = \hat{R}^\alpha(\tau_{\text{lin}}) + \hat{R}^{\alpha'}(\tau_{\text{lin}})(\tau - \tau_{\text{lin}}). \quad (10)$$

The effect of nonuniformities on ignition is studied by varying the initial level of nonuniformities through  $\text{YOC}^{\text{no } \alpha}$ , computing  $\tau_{\text{lin}}$ , and finding the critical  $\gamma_\alpha$  in Eq. (1), yielding a singular explosive solution. This leads to the 3-D ignition condition shown in Fig. 121.16, which can be approximated by  $\gamma_\alpha(\text{YOC}^{\text{no } \alpha})^{4/5} > 1.2$ . Using the definition  $\gamma_\alpha$  in Eq. (4) and substituting the energy conservation and the shell mass at stagnation (modified to include the finite shell-thickness effects<sup>5</sup>), one finds that  $\gamma_\alpha \sim (\rho R)^{3/4} T_*^{15/8}$ , leading to the following analytic ignition condition:

$$\chi^{\text{an}} \approx \rho R_{\text{tot}}^{\text{no } \alpha} (T^{\text{no } \alpha} / 4.5)^{5/2} (\text{YOC}^{\text{no } \alpha})^\mu \approx 1, \quad (11)$$

where  $\rho R_{\text{tot}}^{\text{no } \alpha}$  is the total areal density (approximately equal to the shell areal density) in  $\text{g/cm}^2$ ,  $T^{\text{no } \alpha}$  is the peak hot-spot

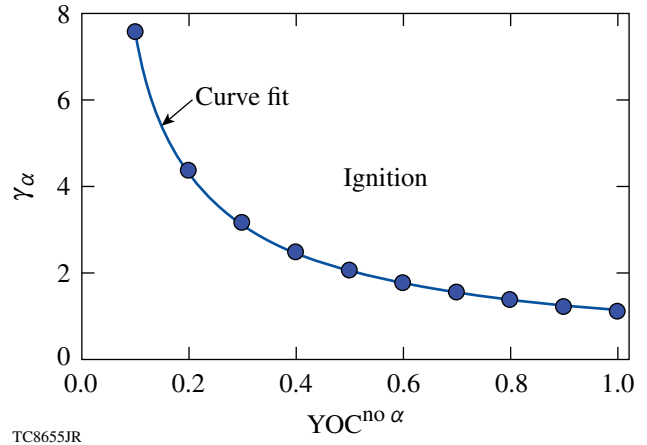
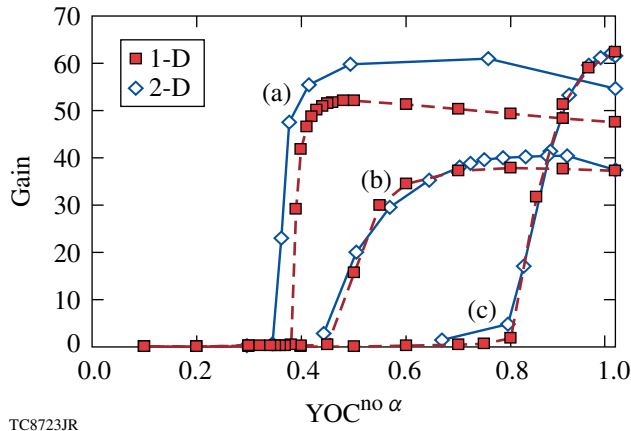


Figure 121.16

The critical parameter  $\gamma_\alpha$  required for a singular solution of Eqs. (1)–(3) versus the YOC. The numerical solution can be fitted by a simple power law  $\gamma_\alpha \approx 1.2/(\text{YOC}^{\text{no } \alpha})^{4/5}$ .

temperature in keV, and  $\mu \approx 1$ . Equation (11) represents a measurable criterion that can be used to assess the 3-D implosion performance, provided the alpha particles do not significantly change the hydrodynamics. This is the case with surrogate deuterium  $\text{D}_2$  and tritium–hydrogen–deuterium (THD) [with a few % of D (Ref. 9)] as well as low-gain (<10%) DT capsules. Obviously, ignited DT capsules do not require an ignition criterion. The effect of nonuniformities enters the ignition condition through a single parameter: the YOC. The accuracy of the generalized ignition condition can be improved by including the effect of the ablative stabilization of the deceleration RT and by tuning the power indices in Eq. (11) through a set of numerical simulations. We have carried out a set of 2-D simulations of ignition targets with varying inner-ice-surface roughness using the code *DRACO*.<sup>10</sup> The initial ice roughness is increased until ignition fails. Each run is repeated without the alpha-particle–energy deposition to determine the no- $\alpha$  neutron yield and the  $\text{YOC}^{\text{no } \alpha}$ . A gain curve is generated by plotting the energy gain (fusion energy yield/laser energy on target) versus the  $\text{YOC}^{\text{no } \alpha}$ . Figure 121.17 shows the gain curves for (a) a 420-kJ direct-drive–ignition target designed to simulate the 1-MJ indirect-drive point design<sup>11</sup> for the National Ignition Facility (NIF),<sup>12</sup> (b) the 1.5-MJ, all-DT direct-drive point design,<sup>13</sup> and (c) the 1-MJ direct-drive wetted-foam design.<sup>14</sup>

To validate the clean volume analysis used in the analytic ignition model, we compare the result of 2-D simulations with the same gain curve obtained from 1-D simulations, where the fusion rate  $\langle \sigma v \rangle$  is reduced by a factor  $\xi$  equal to the  $\text{YOC}^{\text{no } \alpha}$ . Since the alpha-energy deposition depends on the product



TC8723JR

Figure 121.17

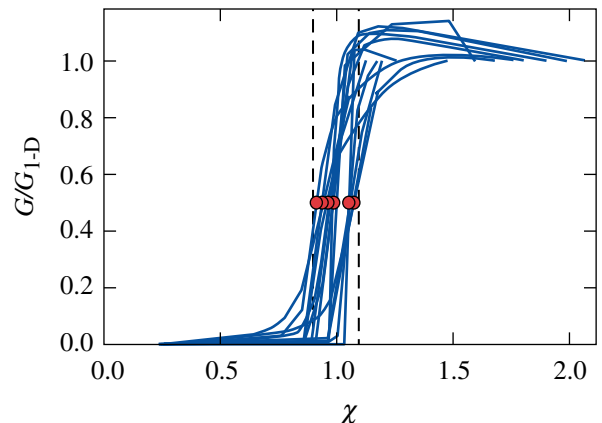
Energy gain versus  $YOC^{no \alpha}$  computed with 1-D (squares) and 2-D (diamonds) simulations. The 2-D simulations use a varying initial ice roughness. The 1-D simulations use a fusion rate reduced by the YOC to mimic the reduction of the clean hot-spot volume. The gain curves are for (a) a 420-kJ direct-drive surrogate of the 1-MJ indirect-drive NIF point design, (b) the 1.5-MJ, all-DT direct-drive point design, and (c) the 1-MJ direct-drive wetted-foam design.

$\langle \sigma v \rangle V_{\text{clean}}$ , reducing  $\langle \sigma v \rangle$  in the 1-D code by the factor  $\xi = YOC^{no \alpha}$  is approximately equivalent to reducing the hot-spot volume by the clean volume fraction. In the 1-D code, the reduction of  $\langle \sigma v \rangle$  takes effect as long as the central hot-spot temperature is below 10 keV. For temperatures above 10 keV, the hot spot is robustly ignited, the RT becomes ablatively stabilized, and  $\xi$  is increased linearly with the temperature until  $\xi = 1$  for  $T > 15$  keV. This effect can also be included in the analytic model by letting  $R_{\text{clean}}$  approach  $R_{1-D}$  [in Eq. (1)] as the temperature exceeds its no- $\alpha$  value. This leads to a reduction of the YOC exponent in Eq. (11) ( $\mu \approx 0.8$ ) and an analytic ignition condition  $\chi^{\text{an}} \approx \rho R_{\text{tot}}^{no \alpha} (T_n^{no \alpha} / 4.5)^{5/2} (YOC^{no \alpha})^{0.8} \approx 1$ . Phasing out the reduction factor  $\xi$  after ignition makes it possible for the 1-D code to correctly predict the burn-wave propagation through the cold shell and the final gain. The results from the modified 1-D code are compared with the 2-D simulations for the three targets above. As shown in Fig. 121.17, the modified 1-D code predicts the “ignition cliff” for critical values of the  $YOC^{no \alpha}$  in agreement with the 2-D simulations. The ignition cliff represents the sharp decrease in gain occurring for a critical value of the YOC. After validating the modified 1-D code with the 2-D simulations, we used the fast 1-D code to generate a database of  $\rho R_n^{no \alpha}$ ,  $T_n^{no \alpha}$ , and  $YOC^{no \alpha}$  for marginally ignited capsules with the ignition YOC varying between 0.3 and 0.8. Marginal ignition is defined as the gain corresponding to the middle point of the ignition cliff ( $\sim$ half the 1-D gain). This is a physical definition of ignition describing the onset of the burn-wave propagation. The 3-D ignition criterion based on a

power law of the three measurable parameters has been derived through the best fit of the simulation results. Figure 121.18 shows the normalized gain curves ( $G/G_{1-D} = \text{gain}/1\text{-D gain}$ ) from the database versus the ignition parameter  $\chi$  representing the “best fit.” The best fit of the ignition criterion  $\chi \approx 1$  yields

$$\chi^{\text{fit}} \equiv \rho R_{\text{tot}(n)}^{no \alpha} (T_n^{no \alpha} / 4.7)^{2.1} (YOC^{no \alpha})^{\mu} \quad (12)$$

with  $\mu \approx 0.63$ . This fit predicts the ignition cliff with a  $\pm 10\%$  error. The subscript  $n$  indicates the spatial and temporal average with the fusion rate (i.e., neutron average) used to approximate the experimental observables. Note that  $T_n^{no \alpha}$  in Eq. (12) is the 1-D temperature. Since the central temperature decreases slightly with increasing nonuniformities (lower YOC), one would expect a weaker dependence on the YOC in Eq. (12) when the 2-D (or the measured) temperature is used. This is shown by the fit from a LASNEX<sup>15</sup> 2-D simulation database of DT and surrogate THD<sup>9</sup> NIF-point-design targets. A fit of the gain curves using the LASNEX database yields an ignition condition like Eq. (12) with  $\mu \approx 0.47$ . The best-performing DT cryogenic implosion on OMEGA<sup>16</sup> to date has achieved an areal density of  $\approx 0.2$  g/cm<sup>2</sup> and a temperature of  $\approx 2$  keV with a YOC of  $\approx 10\%$  (Ref. 17), leading to an ignition parameter  $\chi \sim 10^{-2}$ . Notice that the  $YOC^{no \alpha} \equiv (Y^{\text{ex}} / Y^{1-D})$  requires the 1-D yield ( $Y^{1-D}$ ) as normalization of the experimental yield ( $Y^{\text{ex}}$ ). Since the 1-D yield is a strong function of the temperature, one expects a severe reduction of the temperature dependence in Eq. (12). A fit of the simulation database used in Fig. 121.18



TC8658JR

Figure 121.18

Gain curves from the simulation database. The normalized gain  $G/G_{1-D}$  is plotted versus the ignition parameter  $\chi$ . The ignition cliff is predicted by  $\chi = 1$  with a  $\pm 10\%$  error.

shows that an approximate ignition condition ( $\pm 20\%$  error) for DT targets can be written without the temperature as

$$\rho R_{\text{tot(n)}}^{\text{no } \alpha} \left[ 0.1 Y_{16(\text{no } \alpha)}^{\text{ex}} / M_{\text{sh}}^{\text{mg}} \right]^{0.58} \approx 1, \quad (13)$$

where  $Y_{16}^{\text{ex}}$  is in units of  $10^{16}$  neutrons and  $M_{\text{sh}}$  (in mg) is the portion of the shell mass stagnating at the time of peak neutron rate (bang time). For typical ICF implosions,  $M_{\text{sh}}$  is about half of the unablated shell mass. The latter can be measured or estimated from the simulations with reasonable accuracy. This result is in reasonable agreement with the analysis of Spears *et al.*<sup>9</sup> of the simulated down-scattered neutron spectrum database for the NIF point-design target (fixed  $M_{\text{sh}}$ ). An ignition condition similar to Eq. (12) can be recovered from Eq. (13) by setting  $Y^{\text{ex}} = \text{YOC} \cdot Y^{1\text{-D}}$  and by using the following fit for  $Y^{1\text{-D}}$  of DT targets from a 1-D simulation database:

$$Y_{16(\text{no } \alpha)}^{1\text{-D}} \approx \left( \frac{T_n^{\text{no } \alpha}}{4.7} \right)^{4.7} \left[ \rho R_{\text{tot(n)}}^{\text{no } \alpha} \right]^{0.6} \left( \frac{M_{\text{sh}}^{\text{mg}}}{0.1} \right). \quad (14)$$

The criteria of Eqs. (12) or (13) can be used to assess the performance of cryogenic implosions on the NIF and OMEGA.

#### ACKNOWLEDGMENT

This work has been supported by the U.S. Department of Energy under Cooperative Agreement DE-FC02-04ER54789 and DE-FC52-08NA28302, the University of Rochester, and the New York State Energy Research and Development Authority. The support of DOE does not constitute an endorsement by DOE of the views expressed in this article.

#### REFERENCES

1. S. Atzeni and J. Meyer-ter-Vehn, *The Physics of Inertial Fusion: Beam Plasma Interaction, Hydrodynamics, Hot Dense Matter*, International Series of Monographs on Physics (Clarendon Press, Oxford, 2004); J. D. Lindl, *Phys. Plasmas* **2**, 3933 (1995).
2. J. D. Lawson, *Proc. Phys. Soc. Lond.* **B70**, 6 (1957).
3. M. C. Herrmann, M. Tabak, and J. D. Lindl, *Nucl. Fusion* **41**, 99 (2001).
4. A. Kemp, J. Meyer-ter-Vehn, and S. Atzeni, *Phys. Rev. Lett.* **86**, 3336 (2001).
5. C. D. Zhou and R. Betti, *Phys. Plasmas* **15**, 102707 (2008).
6. J. Garnier and C. Cherfils-Cl  rouin, *Phys. Plasmas* **15**, 102702 (2008).
7. R. Kishony and D. Shvarts, *Phys. Plasmas* **8**, 4925 (2001).
8. A. Schiavi and S. Atzeni, *Phys. Plasmas* **14**, 070701 (2007).
9. B. K. Spears *et al.*, "Prediction of Ignition Implosion Performance Using Measurements of Low-Deuterium Surrogates," to be published in *Physics of Plasmas*.
10. P. B. Radha, T. J. B. Collins, J. A. Delettrez, Y. Elbaz, R. Epstein, V. Yu. Glebov, V. N. Goncharov, R. L. Keck, J. P. Knauer, J. A. Marozas, F. J. Marshall, R. L. McCrory, P. W. McKenty, D. D. Meyerhofer, S. P. Regan, T. C. Sangster, W. Seka, D. Shvarts, S. Skupsky, Y. Srebro, and C. Stoeckl, *Phys. Plasmas* **12**, 056307 (2005).
11. S. W. Haan *et al.*, *Phys. Plasmas* **12**, 056316 (2005).
12. E. I. Moses, *J. Phys., Conf. Ser.* **112**, 012003 (2008).
13. P. W. McKenty, V. N. Goncharov, R. P. J. Town, S. Skupsky, R. Betti, and R. L. McCrory, *Phys. Plasmas* **8**, 2315 (2001).
14. T. J. B. Collins, J. A. Marozas, R. Betti, D. R. Harding, P. W. McKenty, P. B. Radha, S. Skupsky, V. N. Goncharov, J. P. Knauer, and R. L. McCrory, *Phys. Plasmas* **14**, 056308 (2007).
15. G. B. Zimmerman and W. L. Kruer, *Comments Plasma Phys. Control. Fusion* **2**, 51 (1975).
16. T. R. Boehly, D. L. Brown, R. S. Craxton, R. L. Keck, J. P. Knauer, J. H. Kelly, T. J. Kessler, S. A. Kumpan, S. J. Loucks, S. A. Letzring, F. J. Marshall, R. L. McCrory, S. F. B. Morse, W. Seka, J. M. Soures, and C. P. Verdon, *Opt. Commun.* **133**, 495 (1997).
17. T. C. Sangster, V. N. Goncharov, P. B. Radha, V. A. Smalyuk, R. Betti, R. S. Craxton, J. A. Delettrez, D. H. Edgell, V. Yu. Glebov, D. R. Harding, D. Jacobs-Perkins, J. P. Knauer, F. J. Marshall, R. L. McCrory, P. W. McKenty, D. D. Meyerhofer, S. P. Regan, W. Seka, R. W. Short, S. Skupsky, J. M. Soures, C. Stoeckl, B. Yaakobi, D. Shvarts, J. A. Frenje, C. K. Li, R. D. Petrasso, and F. H. S  guin, *Phys. Rev. Lett.* **100**, 185006 (2008).

# In-Situ Detection and Analysis of Laser-Induced Damage on a 1.5-m Multilayer-Dielectric Grating Compressor for High-Energy, Petawatt-Class Laser Systems

## Introduction

Understanding the *in-situ* laser-induced-damage threshold of large-aperture multilayer-dielectric-diffraction (MLD) gratings is paramount for petawatt-class laser facilities to reach design energies.<sup>1–8</sup> Until now, short-pulse damage testing has been performed only on small-scale samples.<sup>9–15</sup> No vacuum-damage test data are available on large-scale MLD gratings, and it has not been proven that one can simply transfer the results of the small samples to full-aperture MLD gratings. This article reports on the performance and findings of a vacuum-compatible grating-inspection system (GIS) that was deployed to detect *in-situ* damages of large-aperture gratings between high-energy shots. The deployment of a GIS makes it possible to operate OMEGA EP<sup>1</sup> safely and effectively because the morphological change of the compressor-grating-surface feature can be monitored in real-time without breaking the vacuum. The following sections (1) describe the mechanism and characterization of the inspection system; (2) introduce the methodology for detecting grating damage and the analysis method for determining the laser-beam fluence causing damage growth; (3) discuss the accuracy of the determined laser-beam fluence; (4) compare the damage-test result of a large-aperture MLD grating to the damage-probability measurement conducted on a small-grating witness sample; and (5) present conclusions.

## Grating-Damage Inspection System

The grating-based pulse compressor of the petawatt-class, short-pulse OMEGA EP laser consists of four sets of tiled-grating assemblies, each measuring 141 cm × 43 cm (Refs. 1 and 16). The line density of the gratings is 1740 lines/mm. The incident and diffraction angles of the laser beam on grating 4 are 61.4° and 72.5°, respectively. During a recent 15-ps, 2.2-kJ energy ramp, it was imperative to monitor the damage growth of the final grating (grating 4) between shots to ensure that damage did not grow to a size that would damage downstream optics. A GIS, illustrated in Fig. 121.19(a), was deployed in the compressor vacuum chamber to detect damage growth on grating 4 during the energy ramp.

The GIS consists of a line-shape illumination generator and an imaging system. The optical layout of the line generator is illustrated in Fig. 121.19(b). A point source from a fiber-based, 1053-nm continuous-wave laser is projected to form a line-shape illumination pattern on the surface of grating 4 using a multi-element lens assembly. An aspheric singlet collimates the light from the fiber and is followed by a half-wave plate used to adjust polarization of the illumination beam. Two spherical lenses focus the light onto a grating surface ~2 m away. The lens pair was designed to provide a  $1/e^2$  spot width of approximately 1 mm at the grating. A negative cylindrical lens located after

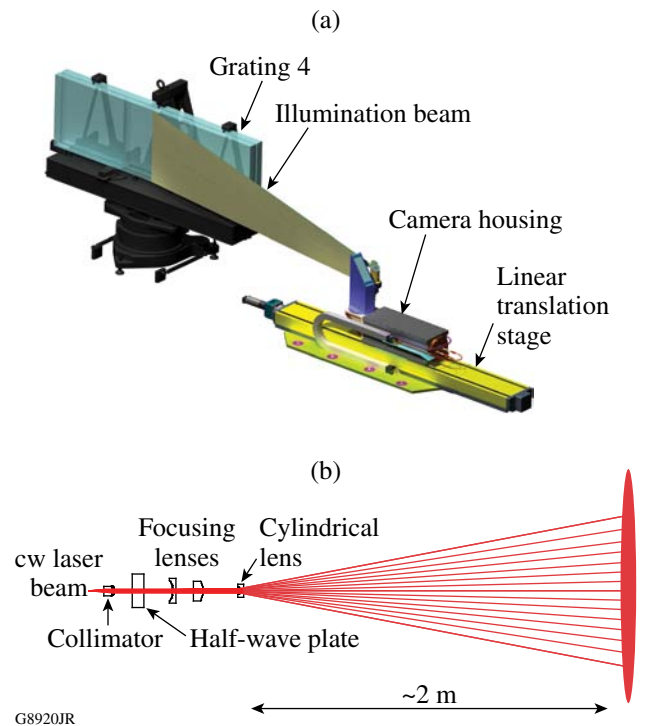


Figure 121.19 (a) The grating-inspection system scans through a 1.5 × 0.43-m large-aperture tiled-grating assembly. (b) Optical layout of the line-shape illumination generator of the grating-damage inspection system.

the spherical lens pair spreads the light in a direction parallel to the grating grooves, perpendicular to the scanning direction. The line length and associated illumination falloff along that direction are determined by the focal length of the cylindrical lens. Successive iterations of the design resulted in a trade-off between illumination uniformity and energy loss from light dispersed past the grating edges. The realized illumination pattern is shown in Fig. 121.20. The line length at 50% and the  $1/e^2$  intensity are 243 mm and 450 mm, respectively. The angle between the illumination beam and grating normal is  $80^\circ$ . This line-shape illumination is scanned across the grating, and light scattered from any features on the surface is imaged to a 10-bit

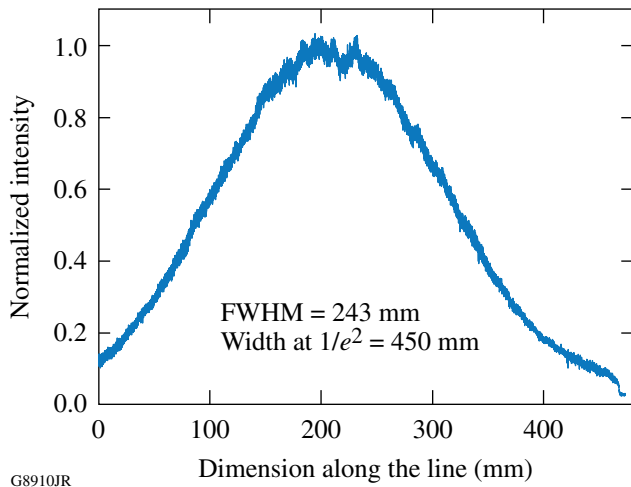


Figure 121.20  
Illumination on the surface of grating 4 exhibits a Gaussian pattern along the groove direction.

charge-coupled device (CCD), having  $8192 \times 1$  pixels with  $7\text{-}\mu\text{m} \times 7\text{-}\mu\text{m}$  pixel size. The CCD is scanned across the grating along with the line-shape generator. The scanned images are then combined to generate a composite two-dimensional (2-D) image of the grating surface. The spatial resolution of a GIS image is limited by the modulation transfer function (MTF) of the imaging system, which was measured to be 0.4 cycle/mm and 1 cycle/mm in horizontal and vertical directions, respectively, at a modulation level of 20%.

**In-Situ Grating-Damage Detection and Damage Analysis**

Before the energy ramp, a reference scan of grating 4 was taken to record any existing features on the grating surface. An on-shot near-field fluence map was measured for each high-energy shot, and a GIS image was obtained after each shot. Six shots delivered the following energies to grating 4: 1.12 kJ, 1.33 kJ, 1.58 kJ, 1.82 kJ, 1.95 kJ, and 2.20 kJ. The corresponding laser-beam peak fluences were  $2.5\text{ J/cm}^2$ ,  $2.7\text{ J/cm}^2$ ,  $3.3\text{ J/cm}^2$ ,  $3.6\text{ J/cm}^2$ ,  $4.0\text{ J/cm}^2$ , and  $4.6\text{ J/cm}^2$ . The nominal pulse width was 15 ps. The near-field imaging system measuring the laser-beam fluence map resides downstream of the grating compressor, as shown in Fig. 121.21(a). During each high-energy shot, 0.7% of the main laser beam was delivered to the short-pulse-diagnostics path (SPDP) through a diagnostic mirror. This sample beam was then down-collimated, further attenuated, and sent to a near-field CCD, imaged to grating 4 for energy and fluence measurement. Figure 121.21(b) shows the scanned image of grating 4 after the 2.2-kJ shot. A majority of the damage features reside in areas ROI 1 and ROI 2 (ROI: region of interest); these two ROI's were chosen for damage analysis. Some of the features on this image were intrinsic to

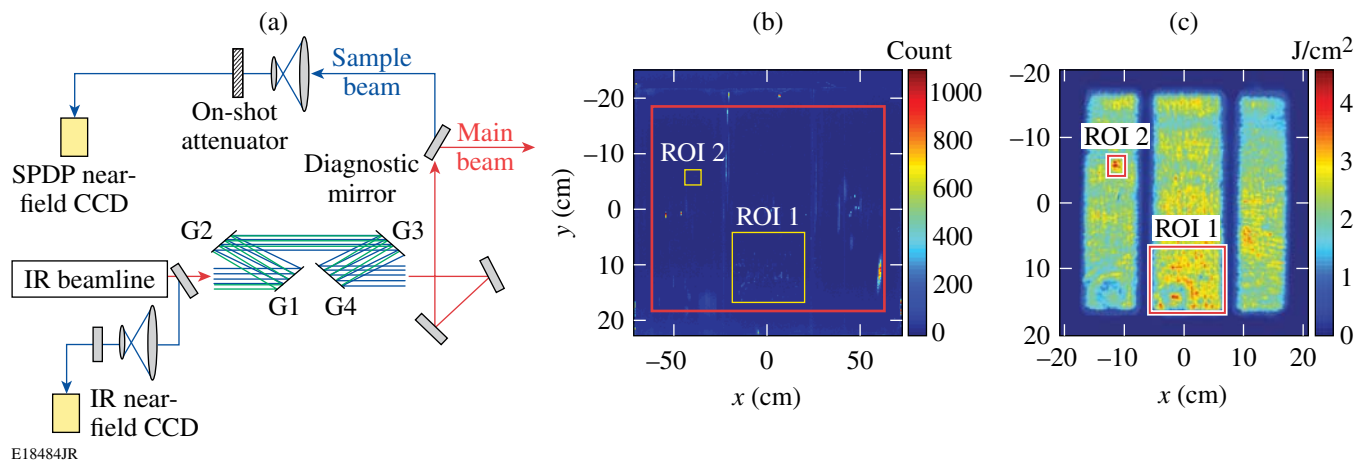


Figure 121.21  
(a) The on-shot laser-fluence measurement path in relation to the grating compressor and the main-beam path; (b) a GIS image after the 2.2-kJ laser shot; (c) a beam-fluence map of the 2.2-kJ laser shot.

the holographic patterning of the gratings, and some existed prior to the energy ramp. Figure 121.21(c) shows the corresponding beam fluence measured on the 2.2-kJ shot. The main beam was shadowed along the gaps of the three individual tiles of grating 4. There is a factor of 0.3 scaling reduction in the  $x$  direction between Figs. 121.21(b) and 121.21(c). This is due to the  $72.5^\circ$  angle between the diagnostic beam and the normal of grating 4. Comparative analysis of the scanned images before and after each shot was used to assess any damage initiation and growth. By spatially registering the scanned image of the grating surface to the fluence map and by correlating the identified feature size and peak beam fluence within a specified ROI for each subsequent shot, the upper fluence limit below which damage growth occurred can be determined.

A scanned image of grating 4 was taken after each high-energy shot. Features in the image were identified using various image-processing techniques: A raw image was filtered

and properly down-sampled based on the MTF limitation of the imaging system of the GIS. For each specified ROI in the image [shown in Fig. 121.21(b)], the corresponding portion of the down-sampled image was binarized for subsequent feature identification. The portion of the image within an ROI having intensity higher than the binarization threshold was identified as a feature. The binarization threshold was determined using the statistical intensity information of the background and the scattering patterns within an ROI. The location and area size of each identified feature were calculated. Although the identified features exhibit various shapes, for ease of comparison between shots, the equivalent diameter of an identified feature was defined as the diameter of a circle that has the same area size as the identified feature. The histogram of the identified features was defined as the number of features at various equivalent diameters. This property was calculated for each ROI after each high-energy shot. The identified features in ROI 1 prior to the energy ramp are illustrated in Fig. 121.22(a). (Note that

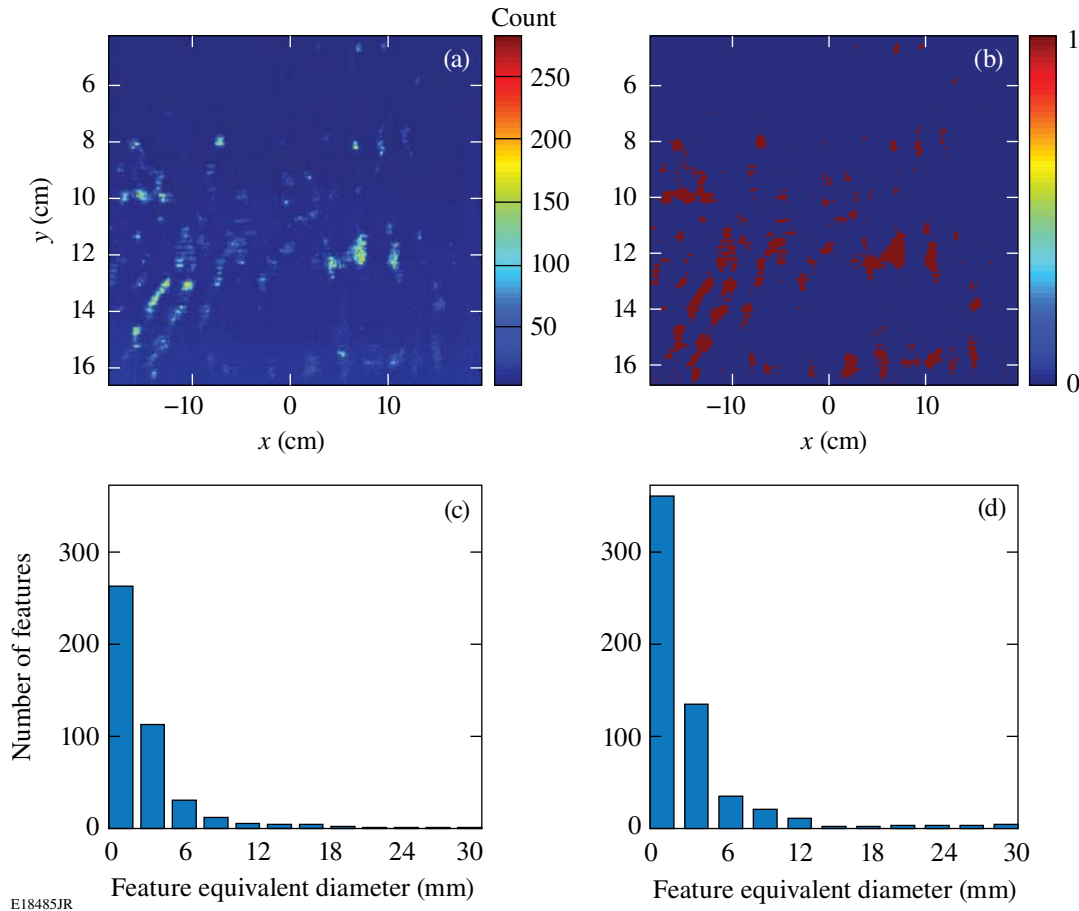


Figure 121.22  
 (a) Detected features in ROI 1 prior to the energy ramp; (b) binarized image of the detected features in ROI 1 prior to the energy ramp; (c) histogram of the detected features after the 1120-J shot; (d) histogram of the detected features after the 2210-J shot.

there are already a significant number of features in this ROI.) Figure 121.22(b) shows the corresponding binarized image of Fig. 121.22(a). Figures 121.22(c) and 121.22(d) illustrate the histograms of the detected features within ROI 1 prior to and after the energy ramp, respectively. Comparing histograms of damage sites of two consecutive shots, one can determine the shot energy that caused significant amounts of damage growth.

Owing to the fact that it is very challenging to register the grating-damage map and the beam-fluence map within high precision, the peak fluence within a ROI was used to estimate the upper limit of the fluence causing damage growth within that area. ROI 2 [also shown in Fig. 121.21(b)], measuring  $23 \text{ mm} \times 24 \text{ mm}$  of grating 4, had no GIS-detectable features before the energy ramp and exhibited significant change after the completion of the energy ramp. This region was chosen to determine the upper limit of the incident fluence causing damage initiation and growth. The binarized scanning image, dimensions scaled to the laser-beam space, and the corresponding fluence map within ROI 2 for 2.2-kJ shot energy are shown in Figs. 121.23(a) and 121.23(b). The growth in damage versus peak fluence in ROI 2 is shown in Fig. 121.23(c). The fluence at which significant growth in damage occurred was determined to be  $3.3 \text{ J/cm}^2$ . This fluence was measured normal to the laser beam ( $72.5^\circ$  relative to the grating normal). The corresponding shot energy was 1.58 kJ. The signal on the streak camera used for pulse measurement was saturated on this shot; therefore, no valid pulse measurement was obtained. Our on-shot pulse-prediction model predicted a narrowed, 12.9-ps (FWHM intensity) pulse due to dispersion induced by nonlinear phase accumulations in the glass amplifiers.<sup>17</sup> A similar analysis performed for ROI 1 showed a consistent result.

### Accuracy of Peak-Fluence Measurement

The spatial resolution of the fluence measurement [Fig. 121.21(c)] was limited by the coherent transfer function (CTF) of the imaging system. The CTF cutoff frequency of the near-field imaging system was measured to be 0.25 cycles/mm. In addition, this imaging system is downstream of grating 4; therefore, the measurement of the beam fluence at a given location could have been affected by damage that existed prior to a particular shot. It is worth verifying that the peak-fluence measurement was not distorted by any damage on the optics of the diagnostics chain. To estimate the accuracy of peak fluence determined for a given ROI, the image from a different on-shot near-field imaging system was used. This system is located just upstream of the grating compressor [illustrated as IR near-field CCD in Fig. 121.21(a)], and its spatial resolution was measured to be  $3\times$  better than the one used to measure

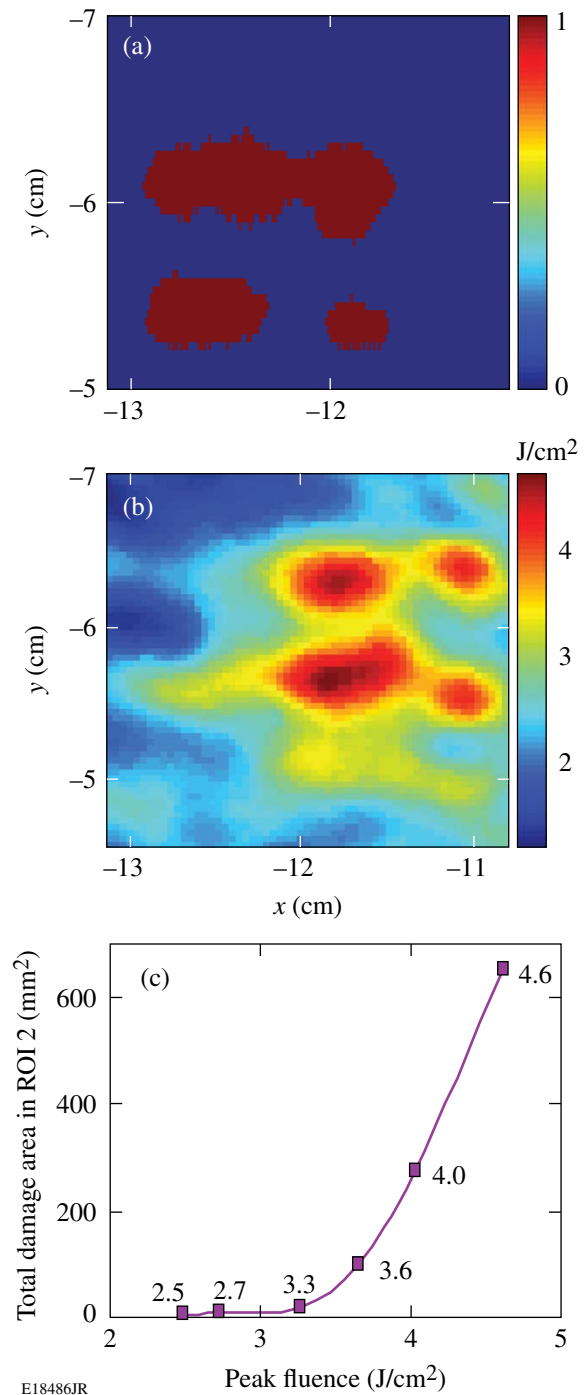


Figure 121.23

(a) Detected features in ROI 2 after the energy ramp; (b) fluence map of ROI 2 of the 2.2-kJ shot; (c) damage size versus beam fluence.

fluence. We then used a propagation model of the compressor, which includes the estimated phase of the beam at the input to the compressor and the phase and intensity effects caused by the compressor, to propagate the fluence map measured at the

input to the compressor to the grating-4 plane. Figure 121.24(a) shows the modeled fluence map for the 2.2-kJ shot. Comparing this fluence map to the measured beam fluence [for ease of comparison, Fig. 121.21(c) is repeated as Fig. 121.24(b)], the measured on-shot peak fluence agrees with the modeled result within 3% and represents the accurate on-shot fluence at grating 4.

**Correlation to the Damage-Test Results Obtained on Small Grating Samples**

Damage probability versus beam fluence was measured in vacuum on a small-scale, 100-mm-diam MLD-grating sample. This piece was the fabrication witness sample of the large-scale gratings deployed on OMEGA EP. Figure 121.25(a) shows the layout of the damage-test setup for sample gratings.

An excitation beam with a pulse width of 11.5 ps (FWHM) for inducing damage and a 1053-nm continuous-wave illumination beam for detecting damage were co-aligned and co-focused to a 420- $\mu\text{m}$  (width at FWHM) focal spot on the grating surface. The incidence angle of the two beams was 61.4° relative to grating normal. The illumination beam was shuttered during the damage excitation process and was turned on afterward for damage detection. The illumination light was scattered by the induced-damage sites and was imaged to a CCD. The resolution of the CCD was 10  $\mu\text{m}$ /pixel. Change in the scattered image was used to determine the initiation of damage. The sample grating was translated along and across the grating-groove directions for damage tests at various locations. For each fluence, ten sites across the grating sample were chosen, and the percentage of sites damaged was used to determine

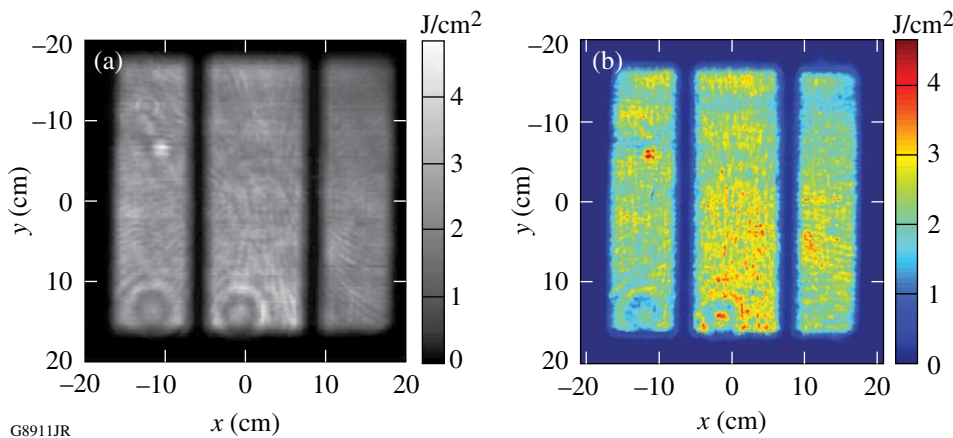


Figure 121.24  
(a) The modeled fluence map using the measured fluence at the input of the compressor; (b) measured-beam-fluence map of the 2.2-kJ laser shot.

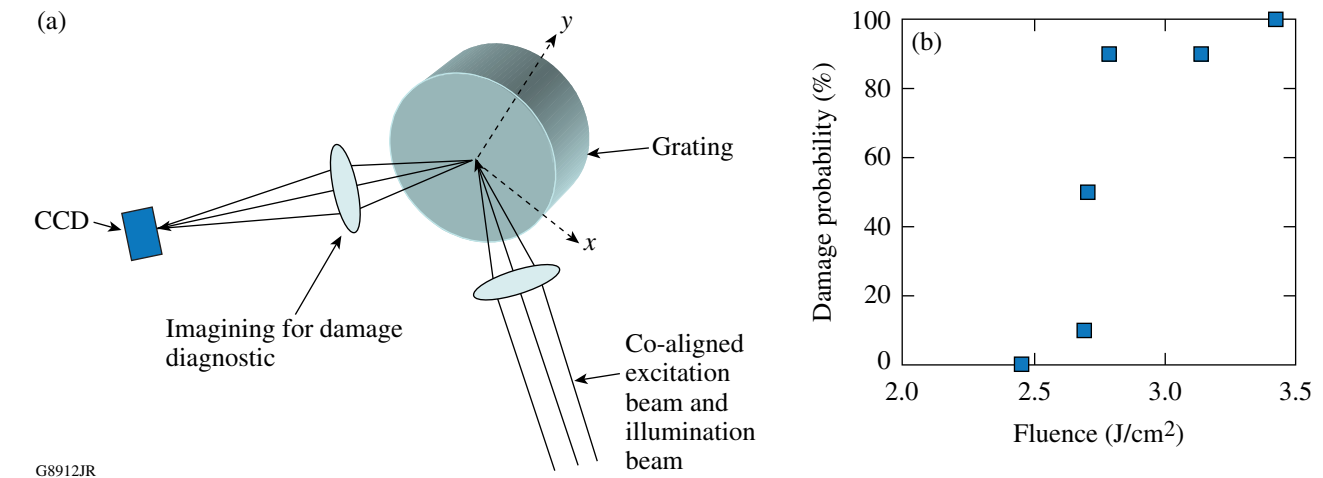


Figure 121.25  
(a) Damage-test setup for damage probability at various beam fluences; (b) damage probability versus beam fluence measured on a 100-mm MLD-grating sample in vacuum.

damage probability. Figure 121.25(b) shows damage probability versus peak beam fluence. To compare with damage-test results of the large-aperture grating, the fluence was scaled to the beam space  $72.5^\circ$  relative to grating normal. As shown in Fig. 121.25(b), all ten sites under test were damaged at a fluence of  $3.4 \text{ J/cm}^2$ . This result is consistent with the determined fluence, where significant growth in damage occurred for a 12.9-ps pulse on large-scale gratings, taking into account that damage threshold scales approximately with the square root of the pulse length.<sup>18</sup> This is the first damage test comparison between a small-sized witness sample and a large-scale grating. More tests will be conducted and results will be reported in a subsequent publication.

### Conclusions

A vacuum-compatible grating-inspection system has been developed to measure the *in-situ* laser-induced damage of a 1.5-m tiled-grating assembly of the OMEGA EP pulse compressor during a 15-ps, 2.2-kJ energy ramp. The grating surface scanning image after each high-energy shot was correlated to the on-shot laser-beam fluence map to determine the relation between damage growth and beam fluence. The upper limit of the fluence at which significant grating-damage growth occurred was determined to be  $3.3 \text{ J/cm}^2$ . This result is consistent with damage-probability measurement conducted on a 100-mm-diam witness-grating sample: the measured peak fluence at which 100% selected sites on the small sample were damaged was  $3.4 \text{ J/cm}^2$ . The deployment of a GIS makes it possible to operate OMEGA EP safely and effectively because the morphological change of the compressor-grating-surface feature can be monitored in real-time without breaking the vacuum. For future work, the damage-probability measurement on a large-scale grating can be conducted using the damage-detection analysis technique described here. The correlation between grating-damage growth, morphological change, and grating diffraction efficiency degradation should be investigated.

### ACKNOWLEDGMENT

We thank Dr. J. H. Kelly for his support on characterizing the coherent transfer functions of the imaging systems for measuring on-shot laser-beam fluence. This work was supported by the U.S. Department of Energy Office of Inertial Confinement Fusion under Cooperative Agreement No. DE-FC52-08NA28302, the University of Rochester, and the New York State Energy Research and Development Authority. The support of DOE does not constitute an endorsement by DOE of the views expressed in this article.

### REFERENCES

1. J. H. Kelly, L. J. Waxer, V. Bagnoud, I. A. Begishev, J. Bromage, B. E. Kruschwitz, T. J. Kessler, S. J. Loucks, D. N. Maywar, R. L. McCrory, D. D. Meyerhofer, S. F. B. Morse, J. B. Oliver, A. L. Rigatti, A. W. Schmid, C. Stoeckl, S. Dalton, L. Folsnsbee, M. J. Guardalben, R. Jungquist, J. Puth, M. J. Shoup III, D. Weiner, and J. D. Zuegel, *J. Phys. IV France* **133**, 75 (2006).
2. C. P. J. Barty *et al.*, *Nucl. Fusion* **44**, S266 (2004).
3. N. Blanchot *et al.*, in *Topical Problems of Nonlinear Wave Physics*, edited by A. M. Sergeev (SPIE, Bellingham, WA, 2006), Vol. 5975, p. 59750C.
4. C. Le Blanc *et al.*, in *Inertial Fusion Sciences and Applications 2003*, edited by B. A. Hammel, D. D. Meyerhofer, J. Meyer-ter-Vehn, and H. Azechi (American Nuclear Society, La Grange Park, IL, 2004), pp. 608–611.
5. C. N. Danson *et al.*, *Nucl. Fusion* **44**, S239 (2004).
6. K. Mima *et al.*, *Fusion Sci. Technol.* **47**, 662 (2005).
7. V. Yanovsky *et al.*, *Opt. Express* **16**, 2109 (2008).
8. M. Martinez *et al.*, in *Laser-Induced Damage in Optical Materials: 2005*, edited by G. J. Exarhos *et al.* (SPIE, Bellingham, WA, 2006), Vol. 5991, p. 59911N.
9. J. A. Britten *et al.*, in *Laser-Induced Damage in Optical Materials: 2003*, edited by G. J. Exarhos *et al.* (SPIE, Bellingham, WA, 2004), Vol. 5273, pp. 1–7.
10. J. A. Britten *et al.*, in *Laser-Induced Damage in Optical Materials: 1995*, edited by H. E. Bennett *et al.* (SPIE, Bellingham, WA, 1996), Vol. 2714, pp. 511–520.
11. A. Reichart *et al.*, in *Laser-Induced Damage in Optical Materials: 2000*, edited by G. J. Exarhos *et al.* (SPIE, Bellingham, WA, 2001), Vol. 4347, pp. 521–527.
12. F. Canova *et al.*, *Opt. Express* **15**, 15324 (2007).
13. W.-J. Kong *et al.*, *Chin. Opt. Lett.* **3**, 181 (2005).
14. A. Cotel *et al.*, presented at the Conference on Lasers and Electro-Optics (CLEO 2005), Baltimore, MD, 22–27 May 2005 (Paper JFB6).
15. J. Neauport *et al.*, *Opt. Express* **15**, 12508 (2007).
16. J. Qiao, A. Kalb, T. Nguyen, J. Bunkenburg, D. Canning, and J. H. Kelly, *Opt. Lett.* **33**, 1684 (2008).
17. Y.-H. Chuang, L. Zheng, and D. D. Meyerhofer, *IEEE J. Quantum Electron.* **29**, 270 (1993).
18. LLE grating-sample test result provided by A. W. Schmid, University of Rochester.

# Probing High-Areal-Density ( $\rho R$ ) Cryogenic-DT Implosions Using Down-Scattered Neutron Spectra Measured by the Magnetic Recoil Spectrometer

## Introduction

Proper assembly of capsule mass, as manifested through the evolution of fuel areal density ( $\rho R$ ),<sup>1-3</sup> is essential for achieving hot-spot ignition planned at the National Ignition Facility (NIF).<sup>4</sup> Experimental information about  $\rho R$  and  $\rho R$  asymmetries, ion temperature ( $T_i$ ), and neutron yield ( $Y_n$ ) is therefore critical to understanding how the fuel is assembled. To obtain this information, a neutron spectrometer—the magnetic recoil spectrometer (MRS)—is being implemented to measure the absolute neutron spectrum in the range of 5 to 30 MeV (Ref. 5). This range covers all essential details of the spectrum, making it possible to determine  $\rho R$ ,  $Y_n$ ,  $T_i$ , and possible nonthermal features in the neutron spectrum, as discussed in Ref. 5. Another MRS has been built and activated on the OMEGA laser<sup>6</sup> for diagnosing energy-scaled, low-adiabat cryogenic deuterium-tritium (DT) implosions.<sup>7</sup> This enables one to experimentally validate the direct-drive-ignition capsule design prior to any experiments at the NIF. Since there are currently no other ways to diagnose  $\rho R$  values larger than  $\sim 200$  mg/cm<sup>2</sup> (Ref. 8), the MRS is now playing an important role on OMEGA.<sup>9,10</sup> The MRS will also play a critical role in guiding the National Ignition Campaign<sup>11</sup> toward the demonstration of thermonuclear ignition and net energy gain.

This article will (1) discuss the principle and design of the MRS on OMEGA and the NIF; (2) present the results from the first measurements of the down-scattered neutron spectrum on OMEGA, from which  $\rho R$  in plastic-capsule implosions and low-adiabat cryogenic-DT implosions have been inferred; (3) discuss the *ab initio* (first-principle) characterization of the MRS and its performance of probing high- $\rho R$  implosions at the NIF; and, finally, (4) present conclusions.

## The Magnetic Recoil Spectrometer (MRS) on OMEGA and the NIF

### 1. MRS Principle

The MRS consists of three main components, as shown in Fig. 121.26: a CH (or CD) foil positioned 10 and 26 cm from the implosion on OMEGA and the NIF, respectively, for producing recoil protons (or deuterons) from incident neutrons; a

focusing magnet, located outside the target chamber on both OMEGA and the NIF, for energy dispersion and focusing of forward-scattered recoil particles onto the focal plane of the spectrometer; and an array of CR-39 detectors, positioned at the focal plane, which records the position of each recoil particle with a detection efficiency of 100% (Ref. 12). The spectrum of the recoil protons (or deuterons) is determined by position at the detector plane and used to infer the absolute neutron spectrum, as discussed in Refs. 5 and 13.

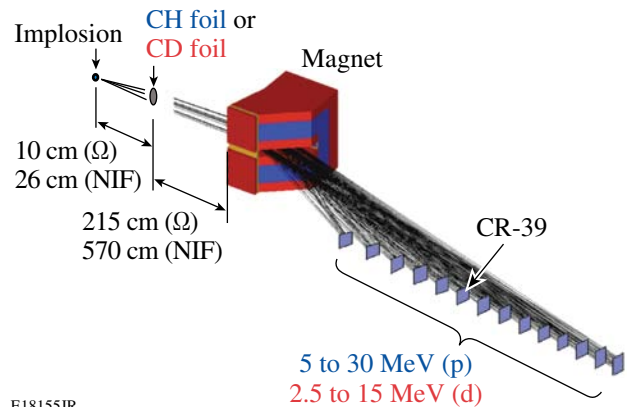


Figure 121.26

A schematic drawing of the MRS, including the CH (or CD) foil, magnet, and CR-39 detector array. The foil is positioned 10 cm and 26 cm from the implosion on OMEGA or the NIF, respectively; the magnet is positioned outside the target chamber on both facilities, i.e., 215 cm from the foil on OMEGA and 570 cm from the foil on the NIF. It is important to the overall design that the same magnet design is used in both the OMEGA MRS and NIF MRS. To detect the forward-scattered recoil protons (or deuterons) when using a CH foil (or CD foil), eleven and nine  $7 \times 5$ -cm<sup>2</sup> CR-39 detectors are positioned at the focal plane in the OMEGA MRS and NIF MRS, respectively. The trajectories shown are for proton energies from 5 to 30 MeV, corresponding to deuteron energies from 2.5 to 15 MeV. The length of the detector plane is 166 cm or 84 cm for the OMEGA MRS or NIF MRS, respectively.

An important strength of the MRS is that the technique can be accurately characterized from first principles (*ab initio*), allowing one to perform quantitative signal and background calculations before the system has been built. An *in-situ* calibration, however, is required to check that the system has been

built and installed according to specification. Since the *ab initio* characterization and *in-situ* calibration of the MRS on OMEGA have been described elsewhere,<sup>5</sup> these efforts will be addressed only briefly in this article. An *ab initio* characterization of the MRS on the NIF is, on the other hand, discussed in detail herein because the system has undergone significant redesign since Ref. 5 was published.

2. MRS Design Considerations

For the MRS to be useful for a wide range of applications on OMEGA and the NIF, it has been designed with the highest-possible detection efficiency ( $\epsilon_{MRS}$ ) for a given energy resolution ( $\Delta E_{MRS}$ ), the largest-possible single-shot dynamic range, and an insensitivity to different types of background. Built-in flexibility has also been included to increase the dynamic range and to more effectively use the MRS for different applications. This is important because a tradeoff between  $\epsilon_{MRS}$  and  $\Delta E_{MRS}$  must be applied depending on yield. For instance, for practical implementation of low-yield applications, such as measurements of down-scattered neutrons from cryogenic-DT implosions on OMEGA and low-yield tritium–hydrogen–deuterium (THD)<sup>14</sup> implosions on the NIF, it is necessary to degrade  $\Delta E_{MRS}$  to increase  $\epsilon_{MRS}$ . For high-yield applications, on the other hand, such as measurements of down-scattered

neutrons from DT implosions on the NIF, the MRS can be configured to operate in a high-resolution/low- $\epsilon_{MRS}$  mode. Several options are available for configuring the MRS: Either a CH or CD foil can be selected to produce recoil protons or deuterons and, therefore, whether the energy range covered for neutrons is 5.0 to 30 MeV or 3.1 to 16.9 MeV. The foil area and foil thickness can be adjusted to change the  $\epsilon_{MRS}$  and  $\Delta E_{MRS}$ . Table 121.VI illustrates the MRS configurations that will be used on the NIF and OMEGA, depending on application. Geant4 (Ref. 15) and a Monte Carlo code were used for the *ab initio* modeling of the MRS (and for assessing its performance when probing high- $\rho R$  implosions at the NIF), when operated in the different configurations shown in Table 121.VI. The results from that modeling at 14 MeV are also shown in Table 121.VI.

The principal sources of background are primary neutrons and neutrons scattered by the chamber wall, diagnostics, and other structures surrounding the MRS. Soft and hard x rays, as well as  $\gamma$  rays, are not an issue since the CR-39 is immune to these types of radiation. Although the CR-39 efficiency for detecting primary neutrons is small<sup>16</sup> ( $\epsilon_{CR-39} \approx 6 \times 10^{-5}$ ), measures are required to reduce the neutron fluence to the required level for successful implementation of the MRS down-scattered

Table 121.VI: Configurations for the MRS on the NIF and OMEGA. Different configurations will be used, depending on application. The OMEGA MRS settings are shown in the parentheses. The low-resolution/high-efficiency mode (Low-Res) will be used when yields are expected to be below  $10^{14}$  (the values in parentheses are for the MRS on OMEGA when diagnosing cryogenic-DT implosions), the medium-resolution/medium-efficiency mode (Med-Res) will be used when yields are expected to be in the range  $10^{14}$  to  $10^{18}$  (the values in the parentheses are for the MRS on OMEGA when diagnosing plastic-capsule implosions), and the high-resolution/low-efficiency mode (High-Res) can be used when yields are expected to be above  $\sim 10^{15}$ . The computed  $\epsilon_{MRS}$  and  $\Delta E_{MRS}$  values at 14 MeV are shown as well. Similar performance is obtained with a CD foil that is about a factor of 2 thinner than the CH foil specified in the table.

	NIF High-Res	NIF (OMEGA) Med-Res	NIF (OMEGA) Low-Res
Yield range	$10^{15}$ to $10^{19}$	$10^{14}$ to $10^{18}$ ( $>10^{13}$ )	$<10^{14}$ ( $>10^{12}$ )
Magnet distance to foil (cm)	570	570 (215)	570 (215)
Magnet aperture area (cm <sup>2</sup> )	20	20 (22)	20 (22)
Foil distance to TCC* (cm)	26	26 (10)	26 (10)
Foil area (cm <sup>2</sup> )	13	13 (10)	13 (10)
CH-foil thickness ( $\mu$ m)	100	250 (250)	550 (550)
$\Delta E_{MRS}$ (FWHM) at 14 MeV (keV)	480	820 (850)	1810 (1830)
$\epsilon_{MRS}$ at 14 MeV	$2 \times 10^{-11}$	$5 \times 10^{-11}$ ( $2 \times 10^{-9}$ )	$10^{-10}$ ( $4 \times 10^{-9}$ )

\*TCC: Target chamber center.

neutron measurements on the NIF (and also on OMEGA as discussed in detail in Ref. 5). This is achieved by adding polyethylene shielding to the MRS as a first step and positioning the CR-39 detector array in the shadow of the NIF target chamber. As the CR-39 detector array is positioned on an off-axis detection plane that is well outside the target chamber, enough space exists to position  $\sim 6000$  lbs of polyethylene shielding around the MRS [see Figs. 121.27(a) and 121.27(b)]. Through neutron-transport simulations using the MCNP code,<sup>17</sup> it was established that the shielding reduces the neutron fluence from  $\sim 10^{-7}$   $\text{cm}^{-2}$  to  $\sim 3 \times 10^{-9}$   $\text{cm}^{-2}$  ( $E_n > 100$  keV) per produced neutron at the CR-39 detector array.<sup>18</sup> Additional reduction of the background (neutron-induced and intrinsic background<sup>19</sup>) is required for successful implementation of the down-scattered neutron measurements for low-yield THD implosions on the NIF (and for cryogenic-DT and plastic-capsule implosions on OMEGA). This is accomplished by the coincidence-counting technique (CCT),<sup>19</sup> which uses the fact that incident signal particles (protons or deuterons) pass straight through the CR-39 material, resulting in front and backside tracks that are correlated. Signal tracks can therefore be distinguished relatively easily from background tracks (neutron-induced and intrinsic tracks) using the CCT since the latter tracks are

generated mainly on one of the surfaces. Applying the CCT to OMEGA MRS data demonstrated orders-of-magnitude signal-to-background ( $S/B$ ) improvement.<sup>19</sup> For high-yield scenarios, such as an ignited case, the standard counting technique (SCT) must instead be applied to the data because the CCT is not effective at high track densities.<sup>19</sup> As a consequence, the  $S/B$  ratio is reduced but compensated by a high signal-to-noise ratio.

### Probing Plastic and Cryogenic-DT Implosions on OMEGA Using Down-Scattered Neutrons

The  $\rho R$  in DT-filled-plastic-capsule implosions on OMEGA has been routinely diagnosed for more than a decade. In these experiments, two magnet-based charged-particle spectrometers (CPS's),<sup>12</sup> shown in Fig. 121.28, have been used to measure the spectrum of knock-on deuterons (KO-D's), elastically scattered by primary DT neutrons, from which fuel  $\rho R$  can be inferred.<sup>20-22</sup> With the implementation of the MRS (Fig. 121.28), spectral measurements of the complementary particle, i.e., the down-scattered neutron, are now possible. From the measured neutron spectrum, the yield ratio between down-scattered neutrons and primary neutrons is determined. This yield ratio, called down-scattered fraction ( $dsf$ ), is to the first order proportional to the fuel  $\rho R$  and probes the com-

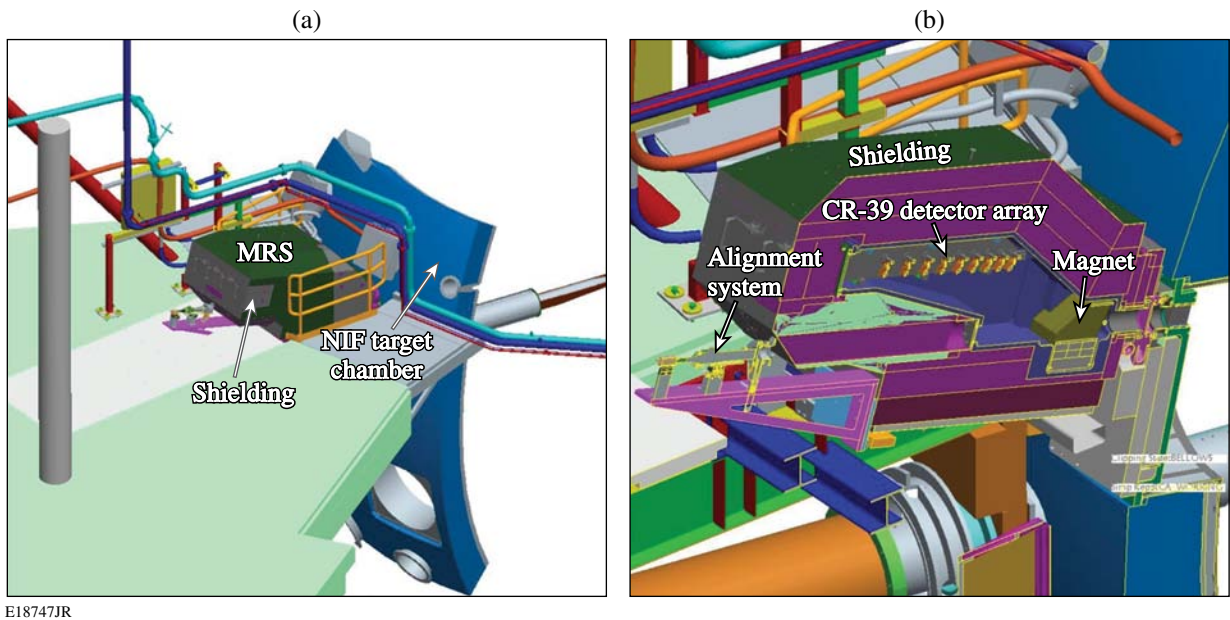
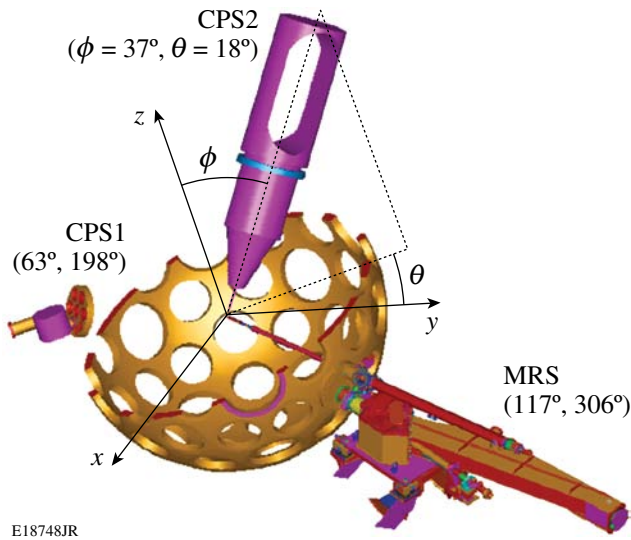


Figure 121.27  
 (a) An engineering drawing of the MRS positioned onto the NIF target chamber at a  $77^\circ$  to  $324^\circ$  line of sight. For maximum suppression of the neutron-induced background, the CR-39 detector array is fully enclosed by  $\sim 6000$  lbs of polyethylene shielding (gray and green) and positioned in the shadow of the 60-cm-thick NIF target chamber (50 cm of concrete and 10 cm of aluminum). (b) A vertical cross cut through the MRS illustrating the various components in the system, i.e., the magnet, CR-39 detector array, alignment system, and shielding. The diagnostic insertion manipulator (DIM) ( $90^\circ$  to  $315^\circ$ ), not shown in these figures, will be used to insert the foil to a distance of 26 cm from the implosion.

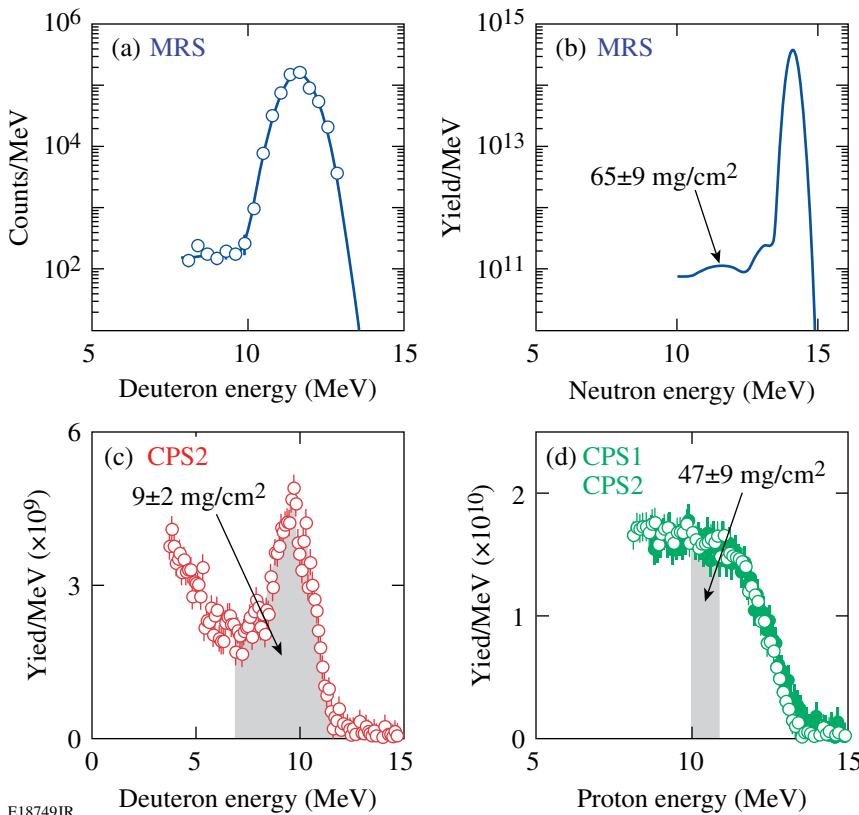


E18748JR

Figure 121.28 MRS, CPS1, and CPS2 on the OMEGA chamber. The MRS is shown here without the 2000-lb shielding that surrounds the diagnostic. The line of sight for each diagnostic is illustrated in terms of the polar angle  $\phi$  and azimuthal angle  $\theta$ . These spectrometers measure the spectra of KO-D's (CPS1 and CPS2) and down-scattered neutrons (MRS), from which fuel  $\rho R$  and  $\rho R$  asymmetries in cryogenic-DT implosions are inferred.

pression performance of an implosion.<sup>5</sup> To more accurately establish the relationship between  $\rho R$  and the measured  $dsf$ , second-order effects, caused by implosion geometry (profiles of primary source and fuel density), were considered as well by using 1-D Monte Carlo and hydro modeling of an implosion. Any geometrical 3-D effects have, on the other hand, not been considered in the modeling. This is a topic for future work.

Measurements of the down-scattered neutron spectrum have been conducted for the first time using the MRS on OMEGA. From the measured  $dsf$  (in the neutron-energy range of 10 to 12 MeV, which corresponds to the deuteron-energy range of about 8 to 10 MeV and  $\sim 7$  to 9 MeV when the MRS is operated in Med-Res and Low-Res modes, respectively),  $\rho R$  values have been inferred for both low- $\rho R$  plastic-capsule implosions and low-adiabat, high- $\rho R$  cryogenic-DT implosions. Data points at neutron energies below 10 MeV were excluded in the analysis since it is comprised primarily by T-T (triton-on-triton) neutrons. The  $\rho R$  data obtained by well-established CPS techniques were used to authenticate the MRS data for these low- $\rho R$  plastic-capsule implosions. This authentication is shown in Figs. 121.29 and 121.30, which illustrate integrated MRS and CPS data for a series of eight CH-capsule implosions



E18749JR

Figure 121.29

Integrated MRS and CPS data obtained for a series of eight CH-capsule implosions producing  $1.6 \times 10^{14}$  primary neutrons (neutron-averaged  $T_i$  was 5.3 keV). In each shot, a capsule with a 15- $\mu\text{m}$ -thick CH shell filled with 15 atm of DT gas was imploded with a 1-ns square pulse delivering  $\sim 23$  kJ of laser energy. (a) The MRS-measured deuteron spectrum and fit to the measured spectrum, which are convolutions of the neutron spectrum and MRS-response function. In these measurements, the MRS was operated with a CD foil in Med-Res mode (see Table 121.VI). From the  $dsf$  value determined from the modeled neutron spectrum, shown in (b), a total  $\rho R$  (fuel + shell) of  $65 \pm 9 \text{ mg/cm}^2$  was inferred. Data points at neutron energies below 10 MeV were excluded in the analysis since they are comprised primarily of T-T neutrons. (c) CPS2 measured spectrum of KO-D's produced in the fuel. From the yield in the high-energy peak<sup>20</sup> (gray), a fuel  $\rho R$  of  $9 \pm 2 \text{ mg/cm}^2$  was inferred. (d) CPS1 and CPS2 measured spectra of knock-on protons (KO-P's) produced in the shell. From the yield in the plateau<sup>20</sup> (gray), a shell  $\rho R$  of  $47 \pm 9 \text{ mg/cm}^2$  was inferred. A total  $\rho R$  of  $56 \pm 10 \text{ mg/cm}^2$  was therefore determined from the CPS1 and CPS2 data. Given that  $\pm 15\%$   $\rho R$  asymmetries are typically observed for this type of implosion, the  $\rho R$  values determined from the MRS and CPS data are in good agreement.

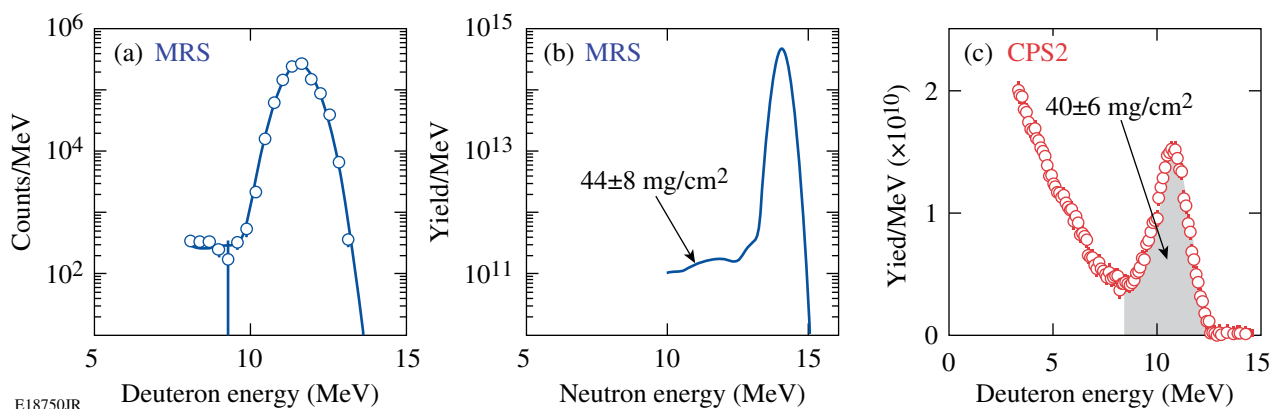


Figure 121.30

Integrated MRS and CPS data obtained for a series of five CD-capsule implosions producing  $2.6 \times 10^{14}$  primary neutrons (neutron-averaged  $T_i$  was 8.0 keV). In each shot, a capsule with a 10- $\mu\text{m}$ -thick CD shell filled with 10 atm of DT gas was imploded with a 1-ns square pulse delivering  $\sim 23$  kJ of laser energy. (a) The MRS-measured deuteron spectrum and fit to the measured spectrum, which are convolutions of the neutron spectrum and MRS-response function. In these measurements, the MRS was operated with a CD foil in Med-Res mode (see Table 121.VI). From the  $dsf$  value determined from the modeled neutron spectrum, shown in (b), a total  $\rho R$  (fuel + shell) of  $44 \pm 8$  mg/cm<sup>2</sup> was inferred. Data points at neutron energies below 10 MeV were excluded in the analysis since they are primarily comprised of T-T neutrons. (c) CPS2 measured spectrum of KO-D's produced in the fuel and shell. From the yield in the high-energy peak<sup>20</sup> (gray), a total  $\rho R$  of  $40 \pm 6$  mg/cm<sup>2</sup> was inferred, which is in excellent agreement with the  $\rho R$  value determined from the MRS.

and a series of five CD-capsule implosions, respectively. As shown by the data, the  $\rho R$  values inferred from the two different techniques are in good agreement, considering the error bars and that  $\pm 15\%$   $\rho R$  asymmetries are typically observed for these types of implosions. These results indicate that the MRS technique provides high-fidelity  $\rho R$  data.

An essential step in achieving high fuel compression and high  $\rho R$  in direct-drive cryogenic-DT implosions on OMEGA is to minimize the shock preheating of the main fuel and therefore maintain the fuel adiabat at the lowest-possible value throughout the pulse. This is achieved by using a multiple-picket laser-drive design,<sup>10</sup> in which the individual picket energies and temporal spacing have been tuned to generate a series of decaying shocks that are designed to coalesce simultaneously with the main drive at the inner surface of the main fuel. Areal density data obtained with the MRS, CPS1, and CPS2 were used to find the multiple-picket laser-drive design that provides maximum compression. From the shape of the CPS-measured KO-D spectrum, the  $\rho R$  is determined for moderate- $\rho R$  cryogenic-DT implosions (up to  $\sim 180$  mg/cm<sup>2</sup>) (Ref. 8). For  $\rho R$  values higher than  $\sim 180$  mg/cm<sup>2</sup>, assessment of the implosion performance relies on the MRS data. Examples of MRS data obtained for three low-adiabat cryogenic-DT implosions are shown in Fig. 121.31. The MRS-measured deuteron spectra and fits to the measured data, which are convolutions of the neutron spectra and MRS-response function, are shown in Fig. 121.31(a). The modeled neutron spectra that give the best fits to the measured data are shown in Fig. 121.31(b). From the

modeled neutron spectra,  $dsf$  values and therefore  $\rho R$  values were determined for these implosions. A  $\rho R$  of  $83 \pm 13$  mg/cm<sup>2</sup> was determined for shot 54926 (imploded with an alpha-3 laser pulse), which is  $\sim 40\%$  of the 1-D value—a result caused by incorrectly tuned pickets in front of the main drive. A  $\rho R$  of  $179 \pm 34$  mg/cm<sup>2</sup> was determined for shot 55231 (imploded with an alpha-3 laser pulse). In this case, the multiple pickets were tuned correctly, resulting in a  $\rho R$  value closer to the 1-D value of 220 mg/cm<sup>2</sup>. For shot 55723, a  $\rho R$  of  $295 \pm 47$  mg/cm<sup>2</sup> was determined (imploded with an alpha-2 laser pulse), which is  $\sim 95\%$  of the 1-D value. Proper shock timing was applied in this case as well. All  $\rho R$  data to date inferred from the CPS systems are shown in Fig. 121.32 as a function of  $\rho R$  data inferred from the MRS. The open data points were obtained when the imploding capsule was centered close to target chamber center (TCC) and had a high-quality ice layer. As expected, these data points are close to the symmetric-implosion line (dashed line). At  $\rho R$  values higher than  $\sim 180$  mg/cm<sup>2</sup> these data points follow the horizontal line at which the CPS technique has saturated (this upper limit depends somewhat on the density and temperature profiles at bang time). In these high- $\rho R$  cases, assessment of the compression performance relies on the MRS data, ice-layer data, and offset data. In addition, the solid data points shown in Fig. 121.32 were obtained when the imploding capsule had a poor ice layer and was significantly offset from TCC. As illustrated by these data points, the poor ice layer and large offset have a detrimental impact on the  $\rho R$  symmetry of an implosion. This is also generally the case when the offset is larger than the hot-spot radius at peak compression.<sup>9</sup>

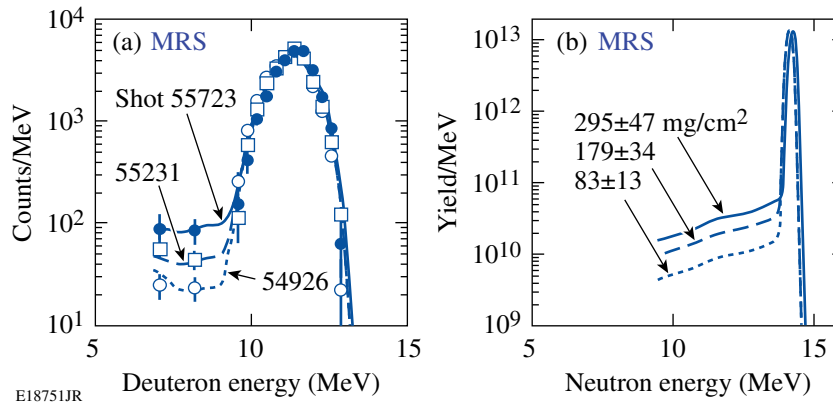


Figure 121.31

MRS data obtained for three low-adiabat cryogenic-DT implosions producing neutron yields in the range of  $2 \times 10^{12}$  to  $4 \times 10^{12}$  (neutron-averaged  $T_i$  was  $\sim 2$  keV for these implosions). (a) MRS-measured deuteron spectra for the three implosions and fits to the measured spectra, which are convolutions of the underlying neutron spectra and the MRS-response function. In these measurements, the MRS was operated with a CD foil in Low-Res mode (see Table 121.VI). From the modeled neutron spectra, shown in (b),  $dsf$  values and, therefore,  $\rho R$ 's were determined for the three implosions. A  $\rho R$  of  $83 \pm 13$  mg/cm<sup>2</sup> was determined for shot 54926 (imploded with an alpha-3 laser pulse), which is  $\sim 40\%$  of the 1-D value—a result of a poorly designed laser drive. A  $\rho R$  of  $179 \pm 34$  mg/cm<sup>2</sup> was determined for shot 55231 (imploded with an alpha-3 laser pulse). In this case, the picket pulses in front of the main laser drive were tuned correctly, resulting in a  $\rho R$  value closer to the 1-D value of 220 mg/cm<sup>2</sup>. For shot 55723, a  $\rho R$  of  $295 \pm 47$  mg/cm<sup>2</sup> was determined (imploded with an alpha-2 laser pulse), which is in agreement with the 1-D  $\rho R$  value considering the error bar. An optimal multiple-picket laser drive was applied in this case as well.

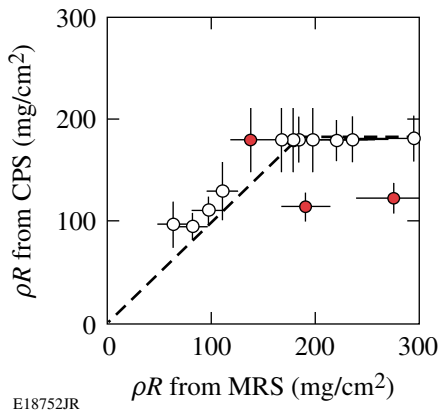


Figure 121.32

The  $\rho R$  inferred from CPS data as a function of  $\rho R$  inferred from MRS data. The open data points were obtained when the imploding capsule had a high-quality ice layer and was centered close to TCC, while the solid points were obtained when the imploding capsule had a poor ice layer and was significantly offset from TCC. As expected, the open data points are close to the symmetric-implosion line (dashed line). At  $\rho R$  values higher than  $\sim 180$  mg/cm<sup>2</sup>, the assessment of the compression performance must rely on MRS data, ice-layer data, and offset data since the CPS technique has saturated. As shown by the solid data points, the poor ice layer and large offset have a detrimental impact on the  $\rho R$  symmetry of an implosion. This is also generally the case when the offset is larger than the hot-spot radius at peak compression.

### Ab initio Characterization of the MRS at the NIF

The performance of a low-yield THD or a high-yield DT implosion at the NIF can be expressed in terms of the ignition threshold factor (ITF),<sup>23</sup> which is a strong function of the

total  $\rho R$ ,  $T_i$ , and  $\rho R$  of the hot spot. Although the ITF is not an accurate representation describing the implosion performance, it provides guidance for how accurately these implosion parameters should be determined at the NIF. From 1-D and 2-D LASNEX<sup>24</sup> simulations it has been concluded that the ITF should be determined to an accuracy better than  $\pm 30\%$ , which puts strong requirements on the  $\rho R$  and  $T_i$  determination. Table 121.VII illustrates one set of requirements that is consistent with the  $\pm 30\%$ -ITF-accuracy requirement for determining  $dsf$ ,  $T_i$ , and  $Y_n$  in THD and DT implosions (in the yield range of  $10^{14}$  to  $10^{19}$ ). Also shown in the table are the expected absolute and relative measurement uncertainties that the MRS will provide for these implosion parameters. These numbers were determined from MRS spectra simulated by a Monte Carlo code that used LASNEX-simulated neutron spectra as input (see Fig. 121.33). From the MRS signal and background levels, the relative uncertainties were computed, as discussed in **Appendix A** (p. 40), where the systematic uncertainties are also derived. As shown by the numbers in Table 121.VII, it is clear that the MRS will meet the requirements for diagnosing both low-yield THD and high-yield DT implosions.

To accurately determine  $dsf$  values from measured MRS spectra, different proton-energy, or deuteron-energy, ranges must be used depending on MRS configuration and type of implosion diagnosed. Table 121.VIII illustrates the proton-energy ranges used for the MRS configured with a CH foil and operated in High-Res, Med-Res, and Low-Res modes.

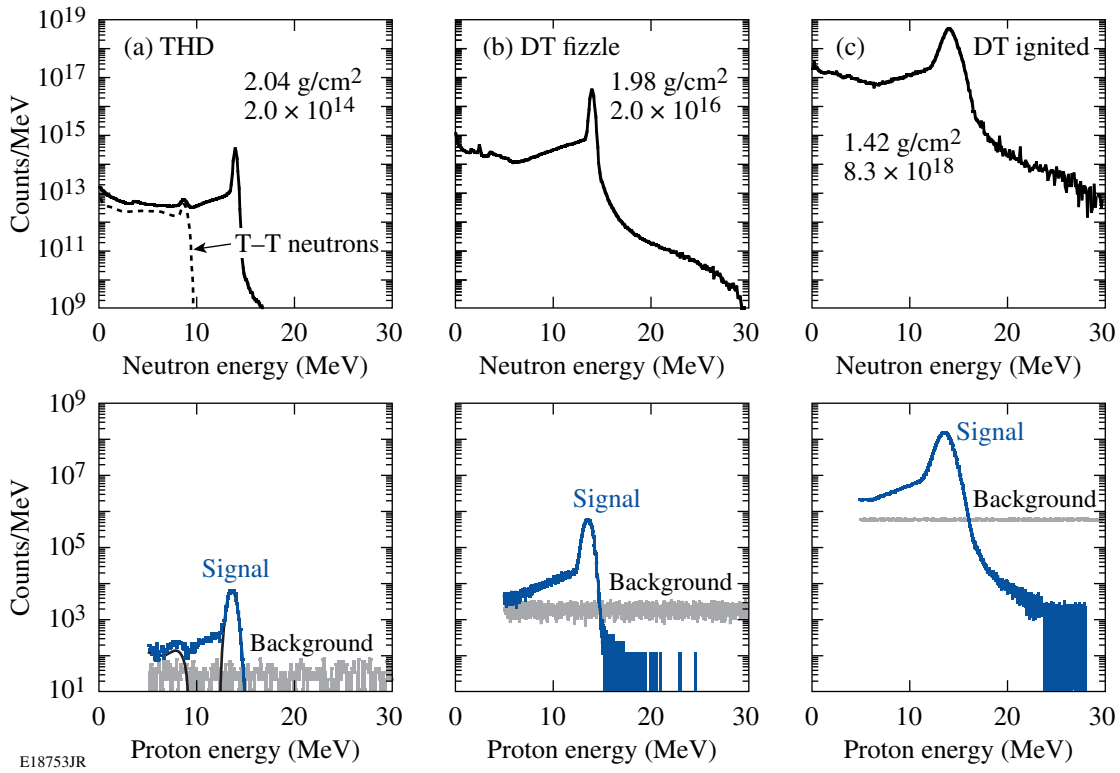


Figure 121.33 A set of LASNEX-simulated neutron spectra and associated MRS signal and background spectra for three NIF implosions: (a) a low-yield THD implosion (the dashed line indicates the T-T neutron spectrum), (b) a fizzle DT implosion, and (c) an ignited DT implosion. The T-T neutron component in the two DT cases is insignificant and, therefore, not shown. The total  $\rho R$  and  $Y_n$  for each implosion are shown in each figure. These spectra were simulated for the MRS configured with a CH foil (Med-Res mode). The CCT, recently developed and now routinely used to analyze OMEGA MRS data, was applied to determine the MRS signal and background spectra for the low-yield THD and fizzle DT implosions. For the ignited case, a standard counting technique (SCT) was applied to the data since the CCT is not effective at high track densities.<sup>19</sup> As shown by the spectra, excellent  $S/B$  is achieved for the  $dsf$ ,  $T_i$ , and  $Y_n$  measurements.

Table 121.VII: Requirements and expected uncertainties for the MRS measuring the down-scattered fraction ( $dsf$ ) (which to the first order depends on  $\rho R$ ),  $T_i$ , and  $Y_n$  produced in THD and DT implosions at the NIF.

		Physics requirements		Expected measurement uncertainties*	
Campaign	Parameter	Absolute	Relative	Absolute (Fig. 121.34; Table 121.IX)	Relative (Fig. 121.34)
THD ( $2 \times 10^{14}$ )	$dsf$	$\pm 7\%$	$\pm 5\%$	$\pm 6\%$	$\pm 4\%$
	$T_i$	$\pm 3\%$	$\pm 3\%$	$\pm 16\%$	$\pm 15\%$
	$Y_n$	$\pm 8\%$	$\pm 2\%$	$\pm 5\%$	$\pm 2\%$
DT ( $2 \times 10^{16}$ )	$dsf$	$\pm 7\%$	$\pm 5\%$	$\pm 3\%$	$\pm 0.5\%$
	$T_i$	$\pm 3\%$	$\pm 3\%$	$\pm 3\%$	$\pm 1\%$
	$Y_n$	$\pm 8\%$	$\pm 2\%$	$\pm 4\%$	$\pm 0.2\%$
DT $10^{17}$ to $10^{19}$	$dsf$	$\pm 7\%$	$\pm 5\%$	$\pm 3\%$	$\pm 0.2\%$
	$T_i$	$\pm 3\%$	$\pm 3\%$	$\pm 3\%$	$\pm 0.3\%$
	$Y_n$	$\pm 8\%$	$\pm 2\%$	$\pm 4\%$	$\pm 0.1\%$

\*The absolute measurement uncertainties are due to both systematic and statistical uncertainties. The relative uncertainties are due only to statistical uncertainties.

Table 121.VIII: Proton-energy ranges for determining the  $dsf$  value from the measured MRS spectra. In the THD case, the T-T neutron spectrum sets a lower limit for the  $dsf$  determination. The primary peak, broadened by the MRS-response function, sets an upper limit for both the THD and DT cases.

	High-Res*	Med-Res*	Low-Res
THD	9.5 to 13.0 MeV	9.4 to 12.5 MeV	9.3 to 11.3 MeV
DT	5.0 to 13.0 MeV	5.0 to 12.5 MeV	5.0 to 11.3 MeV

\*The useful proton-energy range for the  $dsf$  determination is narrower if the implosion ignites. In this case, the energy range is 5 to 11.5 MeV.

These energy ranges were also used to determine the statistical uncertainties for the  $dsf$  values shown in Table 121.VII.

### Summary

For the first time, down-scattered neutron spectra have been measured using the MRS, recently installed and commissioned on OMEGA. From the measured down-scattered neutron spectrum, a  $dsf$  value has been measured from which  $\rho R$  has been inferred for both low- $\rho R$  plastic-capsule implosions and low-adiabat, high- $\rho R$  cryogenic-DT implosions. The  $\rho R$  data obtained from the well-established CPS technique were used to authenticate the MRS data for these low- $\rho R$  plastic-capsule implosions, and results illustrate good agreement between the two techniques. In addition, the  $\rho R$  data obtained from the MRS for the low-adiabat, high- $\rho R$  cryogenic-DT implosions have been essential for understanding how the fuel is assembled and for guiding the cryogenic program at LLE to  $\rho R$  values up to  $\sim 300$  mg/cm<sup>2</sup>.

Recent OMEGA MRS data and Monte Carlo simulations indicate that the MRS on the NIF will meet most of the absolute and relative requirements for determining  $\rho R$ ,  $T_i$ , and  $Y_n$  in both low-yield THD and high-yield DT implosions.

### ACKNOWLEDGMENT

The work described here was supported in part by the U.S. Department of Energy (Grant No. DE-FG03-03SF22691), LLE (No. 412160-001G), LLNL (No. B504974), and GA under DOE (DE-AC52-06NA27279). This work was also supported by the U.S. Department of Energy Office of Inertial Confinement Fusion under Cooperative Agreement No. DE-FC52-08NA28302, the University of Rochester, and the New York State Energy Research and Development Authority. The support of DOE does not constitute an endorsement by DOE of the views expressed in this article.

### Appendix A: Statistical and Systematic Uncertainties for the MRS at the NIF

From the simulated MRS signal and background spectra (three example spectra are shown in Fig. 121.33), it is readily straightforward to calculate the statistical uncertainties for the measured  $dsf$ ,  $T_i$ , and  $Y_n$ . Equation (A1) represents the statisti-

cal uncertainty associated with the  $dsf$  value; Eq. (A2) represents the statistical uncertainty associated with  $T_i$  (Ref. 25); and Eq. (A3) represents the statistical uncertainty associated with  $Y_n$ :

$$\frac{\Delta(dsf)}{dsf} = \frac{\sqrt{S_{ds} + 2B}}{S_{ds}}, \quad (\text{A1})$$

$$\frac{\Delta T_i}{T_i} = \left[ 1 + \left( \frac{\Delta E_{\text{MRS}}}{\Delta E_{\text{D}}} \right)^2 \right] \frac{1}{\sqrt{S_p}}, \quad (\text{A2})$$

$$\frac{\Delta Y_n}{Y_n} = \frac{1}{\sqrt{S_p}}. \quad (\text{A3})$$

Here,  $S_{ds}$  is the integrated down-scattered neutron signal in the selected energy range shown in Table 121.VIII,  $B$  is the total background in this energy range,  $\Delta E_{\text{D}}$  is the width of the Doppler-broadened neutron spectrum, which is to the first order equal to  $177\sqrt{T_i}$  for the DT reaction ( $T_i$  given in keV) (Ref. 26), and  $S_p$  is the integrated primary neutron signal. As shown by Eq. (A3), the yield uncertainty can be expressed in terms of only  $S_p$  because the primary signal is orders of magnitude higher than the background. These equations were applied to simulated MRS spectra for 13 different implosions, which resulted in the statistical uncertainties shown in Fig. 121.34.

For illustration purposes, as well as for calculating systematic uncertainties involved with the MRS, it is useful to express  $\epsilon_{\text{MRS}}$  and  $\Delta E_{\text{MRS}}$  as<sup>5</sup>

$$\epsilon_{\text{MRS}}(E_n) = \frac{\Omega_n}{4\pi} \cdot n_i \cdot t_f \int \frac{d\sigma(E_n)}{d\Omega_{\text{lab}}} d\Omega \quad (\text{A4})$$

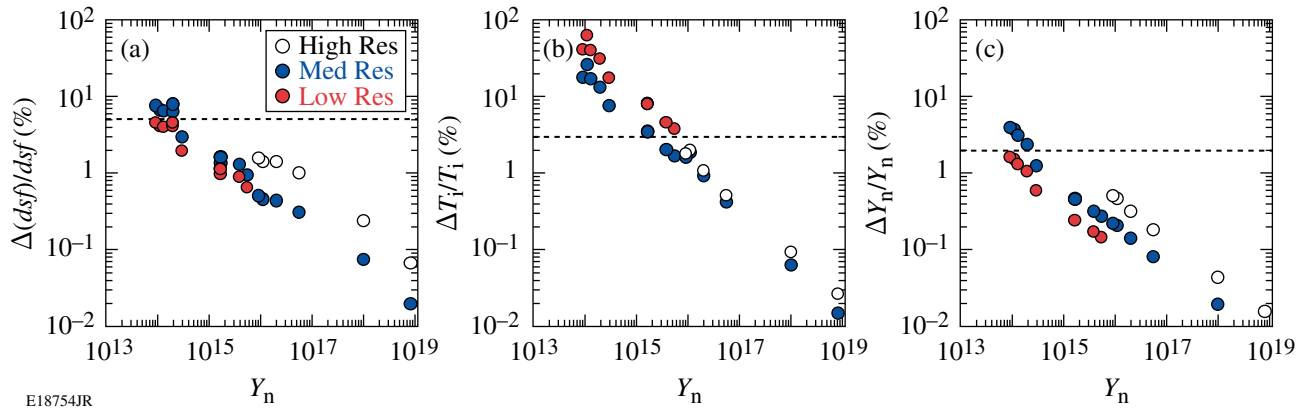


Figure 121.34

Statistical measurement uncertainty for (a)  $dsf$ , (b)  $T_i$ , and (c)  $Y_n$  as a function of neutron yield when the MRS is operating in High-Res, Med-Res, and Low-Res modes. Thirteen implsions were used in these calculations. The relative requirements, illustrated in Table 121.VII, are indicated by the dashed lines.

and

$$\Delta E_{\text{MRS}}(E_n) \approx \sqrt{\Delta E_f^2(E_n) + \Delta E_k^2(E_n) + \Delta E_m^2(E_n)}, \quad (\text{A5})$$

respectively. Here,  $\Omega_n$  is the solid angle subtended by the foil,  $n_i$  is the hydrogen (or deuterium) number density in the foil,  $t_f$  is the thickness of the foil,  $d\sigma(E_n)/d\Omega_{\text{lab}}$  is the differential elastic-scattering cross section in the laboratory frame, “ $\Omega_a$ ” is the solid angle subtended by the aperture in front of the magnet,  $\Delta E_f$  is the energy broadening in the conversion foil,  $\Delta E_k$  is the kinematic energy broadening, and  $\Delta E_s$  is the ion-optical broadening. Since the solid angle subtended by the foil can be expressed in terms of foil area ( $A_f$ ) and foil distance ( $R_f$ ), and the differential elastic cross section integrated over the solid angle subtended by the magnet aperture can be approximated by  $d\sigma/d\Omega_{\text{lab}}(E_n, 0^\circ) \cdot (A_a/R_a^2)$  (where  $A_a$  is the magnet aperture area and  $R_a$  is the magnet-aperture distance to the foil), Eq. (A4) can be rewritten as

$$\varepsilon_{\text{MRS}}(E_n) \approx \frac{A_f}{4\pi R_f^2} \cdot n_i \cdot t_f \cdot \frac{d\sigma(E_n, 0^\circ)}{d\Omega_{\text{lab}}} \cdot \frac{A_a}{R_a^2}. \quad (\text{A6})$$

Using Eq. (A6) and the Brysk formula,<sup>26</sup>  $Y_n$ ,  $dsf$ , and  $T_i$  can now be expressed as

$$Y_n \approx \frac{S_p}{\frac{A_f}{4\pi R_f^2} \cdot n_i \cdot t_f \cdot \frac{d\sigma(E_n, 0^\circ)}{d\Omega_{\text{lab}}} \cdot \frac{A_a}{R_a^2}}, \quad (\text{A7})$$

$$dsf \approx \frac{\frac{d\sigma(p, 0^\circ)}{d\Omega_{\text{lab}}} S_{\text{ds}}}{\frac{d\sigma(ds, 0^\circ)}{d\Omega_{\text{lab}}} S_p}, \quad (\text{A8})$$

and

$$T_i = \frac{1}{177^2} [\Delta E_{\text{meas}}^2 - \Delta E_{\text{MRS}}^2], \quad (\text{A9})$$

respectively. Here,  $p$  and  $ds$  in Eq. (A8) represent the average energy of primary and down-scattered neutrons, respectively, and  $\Delta E_{\text{meas}}$  is the width of the measured primary spectrum. An expression for the systematic uncertainty involved with the  $dsf$ ,  $Y_n$ , and  $T_i$  measurements can now be derived from Eqs. (A7)–(A9), i.e.,

$$\frac{\sigma_{Y_n}}{Y_n} \approx \sqrt{\left(\frac{\sigma_{A_f}}{A_f}\right)^2 + \left(\frac{\sigma_{R_f}}{R_f}\right)^2 + \left(\frac{\sigma_{n_i}}{n_i}\right)^2 + \left(\frac{\sigma_{t_f}}{t_f}\right)^2 + \left[\frac{\sigma_{d\sigma(p, 0^\circ)}}{d\Omega_{\text{lab}}}\right]^2 + \left(\frac{\sigma_{A_a}}{A_a}\right)^2 + 4\left(\frac{\sigma_{R_a}}{R_a}\right)^2}, \quad (\text{A10})$$

Table 121.IX: Systematic uncertainties for the different parameters expressed in Eqs. (A9) and (A10) and their combined contribution to the total error for the different MRS configurations shown in Table 121.VII. These numbers are valid only for the CH foils. The cross-section uncertainties involved with the CD foil are about a factor of 2 higher than the ones involved with the CH foil.

	Absolute	High-Res (%)	Med-Res (%)	Low-Res (%)
Foil area uncertainty	$\pm 0.3 \text{ cm}^2$	$\pm 2.3$	$\pm 2.3$	$\pm 2.3$
Foil distance uncertainty	$\pm 0.1 \text{ cm}$	$\pm 0.4$	$\pm 0.4$	$\pm 0.4$
Number density uncertainty	$\pm 10^{21} \text{ cm}^3$	$\pm 1.3$	$\pm 1.3$	$\pm 1.3$
Foil thickness uncertainty	$\pm 2.0 \text{ mm}$	$\pm 2.0$	$\pm 0.8$	$\pm 0.4$
Cross section uncertainty (p)	$\pm 3 \text{ mb/sr}$	$\pm 1.4$	$\pm 1.4$	$\pm 1.4$
Cross section uncertainty (ds)	$\pm 0.9 \text{ mb/sr}$	$\pm 2.5$	$\pm 2.5$	$\pm 2.5$
Magnet-aperture area uncertainty	$\pm 0.2 \text{ cm}^2$	$\pm 1.0$	$\pm 1.0$	$\pm 1.0$
Response function uncertainty	$\pm 10 \text{ keV}$	$\pm 2.1$	$\pm 1.1$	$\pm 0.6$
Magnet-aperture distance uncertainty	$\pm 0.1 \text{ cm}$	$\pm 0.02$	$\pm 0.02$	$\pm 0.02$
Total uncertainty for $Y_n$		$\pm 4.5$	$\pm 4.1$	$\pm 4.0$
Total uncertainty for $dsf$		$\pm 2.9$	$\pm 2.9$	$\pm 2.9$
Total uncertainty for $T_i$ (at 5 keV)		$\pm 2.9$	$\pm 6.4$	$\pm 13.4$

$$\frac{\sigma_{dsf}}{dsf} \approx \sqrt{\left( \frac{\sigma_{d\sigma(p,0^\circ)}}{d\Omega_{lab}} \right)^2 + \left( \frac{\sigma_{d\sigma(ds,0^\circ)}}{d\Omega_{lab}} \right)^2}, \quad (\text{A11})$$

and

$$\frac{\sigma_{T_i}}{T_i} \simeq \frac{2}{\left( \frac{\Delta E_{meas}}{\Delta E_{MRS}} \right)^2 - 1} \frac{\sigma_{\Delta E_{MRS}}}{\Delta E_{MRS}}, \quad (\text{A12})$$

respectively. As shown by Eq. (A11), the systematic uncertainty for the  $dsf$  value depends only on the uncertainties in the differential elastic-scattering cross sections at the different energies. This is an important feature of the MRS that can be explained by the fact that the systematic uncertainties associated with the MRS geometry are canceled out, i.e., simultaneous measurements of the down-scattered and primary neutrons are exposed to identical geometry-related uncertainties. Table 121.IX illustrates the actual systematic uncertainties for the different parameters expressed in Eqs. (A9)–(A11) and their combined contribution to the total error for the different MRS configurations shown in Table 121.VII.

## REFERENCES

1. S. W. Haan *et al.*, Phys. Plasmas **2**, 2480 (1995).
2. J. D. Lindl, R. L. McCrory, and E. M. Campbell, Phys. Today **45**, 32 (1992).
3. M. D. Rosen, Phys. Plasmas **3**, 1803 (1996).
4. G. H. Miller, E. I. Moses, and C. R. Wuest, Nucl. Fusion **44**, S228 (2004).
5. J. A. Frenje, D. T. Casey, C. K. Li, J. R. Rygg, F. H. Séguin, R. D. Petrasso, V. Yu. Glebov, D. D. Meyerhofer, T. C. Sangster, S. Hatchett, S. Haan, C. Cerjan, O. Landen, M. Moran, P. Song, D. C. Wilson, and R. J. Leeper, Rev. Sci. Instrum. **79**, 10E502 (2008).
6. T. R. Boehly, D. L. Brown, R. S. Craxton, R. L. Keck, J. P. Knauer, J. H. Kelly, T. J. Kessler, S. A. Kumpan, S. J. Loucks, S. A. Letzring, F. J. Marshall, R. L. McCrory, S. F. B. Morse, W. Seka, J. M. Soures, and C. P. Verdon, Opt. Commun. **133**, 495 (1997).
7. R. L. McCrory, D. D. Meyerhofer, R. Betti, R. S. Craxton, J. A. Delettrez, D. H. Edgell, V. Yu. Glebov, V. N. Goncharov, D. R. Harding, D. W. Jacobs-Perkins, J. P. Knauer, F. J. Marshall, P. W. McKenty, P. B. Radha, S. P. Regan, T. C. Sangster, W. Seka, R. W. Short, S. Skupsky, V. A. Smalyuk, J. M. Soures, C. Stoeckl, B. Yaakobi, D. Shvarts, J. A. Frenje, C. K. Li, R. D. Petrasso, and F. H. Séguin, Phys. Plasmas **15**, 055503 (2008).
8. J. A. Frenje, C. K. Li, F. H. Séguin, D. T. Casey, R. D. Petrasso, T. C. Sangster, R. Betti, V. Yu. Glebov, and D. D. Meyerhofer, Phys. Plasmas **16**, 042704 (2009).

9. T. C. Sangster, V. N. Goncharov, R. Betti, T. R. Boehly, D. T. Casey, T. J. B. Collins, R. S. Craxton, J. A. Delettrez, D. H. Edgell, R. Epstein, K. A. Fletcher, J. A. Frenje, V. Yu. Glebov, D. R. Harding, S. X. Hu, I. V. Igumenshchev, J. P. Knauer, S. J. Loucks, C. K. Li, J. A. Marozas, F. J. Marshall, R. L. McCrory, P. W. McKenty, D. D. Meyerhofer, P. M. Nilson, S. P. Padalino, R. D. Petrasso, P. B. Radha, S. P. Regan, F. H. Séguin, W. Seka, R. W. Short, D. Shvarts, S. Skupsky, V. A. Smalyuk, J. M. Soures, C. Stoeckl, W. Theobald, and B. Yaakobi, "Shock-Tuned Cryogenic DT-Implsion Performance on OMEGA," to be published in *Physics of Plasmas*.
10. V. N. Goncharov, T. C. Sangster, T. R. Boehly, S. X. Hu, I. V. Igumenshchev, F. J. Marshall, R. L. McCrory, D. D. Meyerhofer, P. B. Radha, W. Seka, S. Skupsky, C. Stoeckl, D. T. Casey, J. A. Frenje, and R. D. Petrasso, "Multiple-Picket Cryogenic Designs for OMEGA and the NIF," submitted to *Physical Review Letters*.
11. E. I. Moses, in *Current Trends in International Fusion Research: Proceedings of the 7th Symposium Selected Presentations*, edited by E. Panarella and R. Raman (American Institute of Physics, New York, 2009), Vol. 1154, pp. 53–59.
12. F. H. Séguin, J. A. Frenje, C. K. Li, D. G. Hicks, S. Kurebayashi, J. R. Rygg, B.-E. Schwartz, R. D. Petrasso, S. Roberts, J. M. Soures, D. D. Meyerhofer, T. C. Sangster, J. P. Knauer, C. Sorce, V. Yu. Glebov, C. Stoeckl, T. W. Phillips, R. J. Leeper, K. Fletcher, and S. Padalino, *Rev. Sci. Instrum.* **74**, 975 (2003).
13. J. A. Frenje, K. M. Green, D. G. Hicks, C. K. Li, F. H. Séguin, R. D. Petrasso, T. C. Sangster, T. W. Phillips, V. Yu. Glebov, D. D. Meyerhofer, S. Roberts, J. M. Soures, C. Stoeckl, K. Fletcher, S. Padalino, and R. J. Leeper, *Rev. Sci. Instrum.* **72**, 854 (2001).
14. A THD capsule is filled with more deuterium-lean fuel mixtures and H-dopant levels up to 25% (by atom).
15. S. Agostinelli *et al.*, *Nucl. Instrum. Methods Phys. Res. A* **506**, 250 (2003).
16. J. A. Frenje, C. K. Li, F. H. Séguin, S. Kurebayashi, R. D. Petrasso, J. M. Soures, J. Delettrez, V. Yu. Glebov, D. D. Meyerhofer, P. B. Radha, S. Roberts, T. C. Sangster, S. Skupsky, and C. Stoeckl, *Phys. Plasmas* **9**, 4719 (2002).
17. X-5 Monte Carlo Team, *Version 5*, Los Alamos National Laboratory, Los Alamos, NM, Report LA-R-03-1987 (24 April 2003).
18. D. T. Casey, J. A. Frenje, C. K. Li, F. H. Séguin, R. D. Petrasso, V. Yu. Glebov, D. D. Meyerhofer, and T. C. Sangster, "Minimizing Neutron Background for the Magnetic Recoil Spectrometer at OMEGA and the NIF," to be submitted to *Review of Scientific Instruments*.
19. D. T. Casey, J. A. Frenje, C. K. Li, F. H. Séguin, R. D. Petrasso, V. Yu. Glebov, D. D. Meyerhofer, and T. C. Sangster, "The Coincidence Counting Technique for Enhanced Background Rejection in the MRS Data," to be submitted to *Review of Scientific Instruments*.
20. C. K. Li, F. H. Séguin, D. G. Hicks, J. A. Frenje, K. M. Green, S. Kurebayashi, R. D. Petrasso, D. D. Meyerhofer, J. M. Soures, V. Yu. Glebov, R. L. Keck, P. B. Radha, S. Roberts, W. Seka, S. Skupsky, C. Stoeckl, and T. C. Sangster, *Phys. Plasmas* **8**, 4902 (2001).
21. S. Skupsky, R. W. Short, T. Kessler, R. S. Craxton, S. Letzring, and J. M. Soures, *J. Appl. Phys.* **66**, 3456 (1989).
22. S. Kacendar, S. Skupsky, A. Entenberg, L. Goldman, and M. Richardson, *Phys. Rev. Lett.* **49**, 463 (1982).
23. B. K. Spears *et al.*, "Prediction of Ignition Implsion Performance Using Measurements of Low-Deuterium Surrogates," to be published in *Physics of Plasmas*.
24. G. B. Zimmerman and W. L. Kruer, *Comments Plasma Phys. Control. Fusion* **2**, 51 (1975).
25. O. N. Jarvis *et al.*, *Rev. Sci. Instrum.* **57**, 1717 (1986).
26. H. Brysk, *Plasma Phys.* **15**, 611 (1973).

# Strong-Coupling and Degeneracy Effects in Inertial Confinement Fusion Implosions

As one of the potentially viable ways to generate clean energy, inertial confinement fusion (ICF) has been pursued for decades.<sup>1</sup> In “hot-spot” ICF designs, a cryogenic DT capsule is driven to implode either directly by intense laser pulses<sup>2</sup> or indirectly by x rays in a hohlraum.<sup>3</sup> At the stagnation stage, a high-density shell ( $>1000\times$  solid-DT density) is assembled around the hot spot for the fusion burn to propagate, thereby generating a net energy gain. To reach such high compression, the imploding shell must stay on a low adiabat, which is conventionally characterized as  $\alpha$  (the ratio of the fuel pressure to the Fermi-degenerate pressure). Accurate knowledge of the equation of state (EOS) of the DT fuel is essential to ICF designs<sup>1</sup> because the compressibility is determined by the EOS.<sup>4</sup>

Dynamically compressed by shocks and/or adiabatic compression waves driven by laser ablation,<sup>5</sup> the imploding DT

shell undergoes a wide range of plasma conditions at densities from  $\sim 0.1 \text{ g/cm}^3$  up to  $1000 \text{ g/cm}^3$  and temperatures varying from a few electron volts to several hundred electron volts.<sup>1</sup> One may expect such plasmas to enter the strongly coupled and degenerate regimes, where many-body effects become important. Strongly coupled and degenerate plasma conditions are indeed accessed in low-adiabat cryogenic implosions on the OMEGA Laser System<sup>6</sup> as well as at the National Ignition Facility (NIF).<sup>7</sup> Examples from hydrosimulations are shown in Figs. 121.35(a)–121.35(c) for a low-adiabat ( $\alpha \simeq 2.5$ ) cryo-DT implosion on OMEGA and in Figs. 121.35(d)–121.35(f) for a direct-drive-ignition design for the NIF. The laser pulse shapes in panels (a) and (d) are plotted. Our hydrocode simulations show that the predicted density ( $\rho$ ) and temperature ( $T$ ) “paths” of the driven DT shell, which are plotted in the middle panels [(b) and (e)], undergo a variety of drive stages, includ-

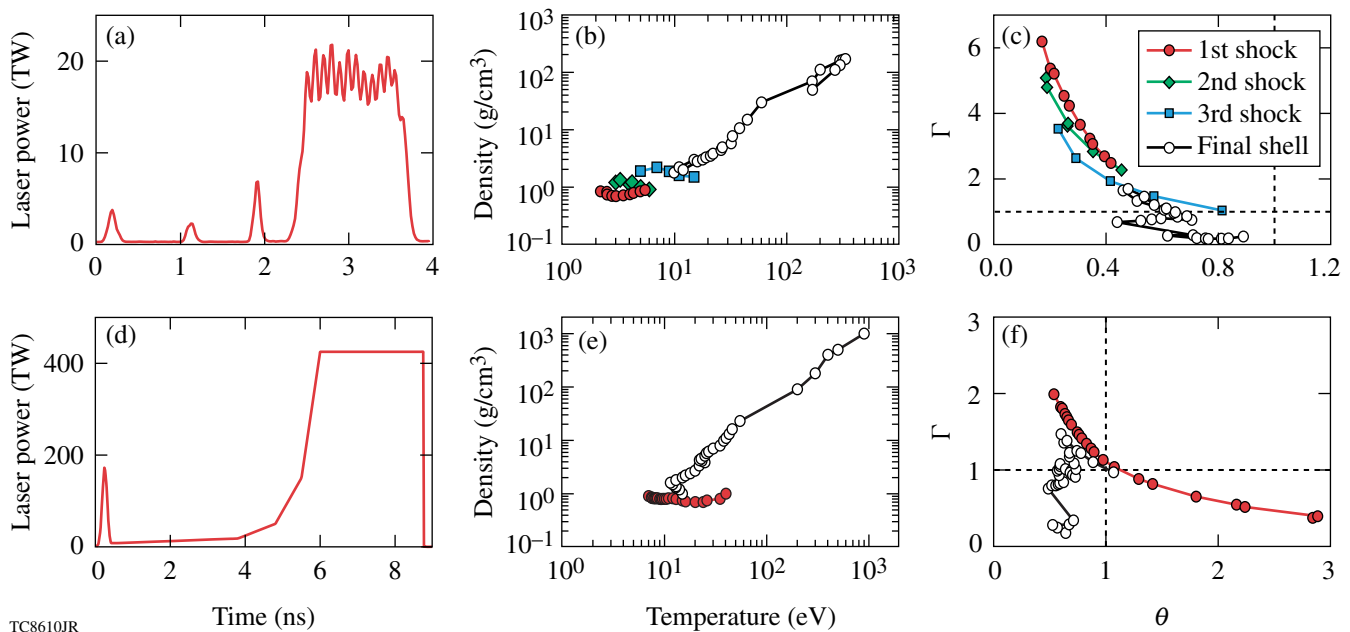


Figure 121.35

[(a)–(c)] A cryogenic-DT implosion on OMEGA; [(d)–(f)] a direct-drive-ignition design for the NIF. In both cases, strongly coupled and degenerate plasma conditions are *indeed* accessed.

ing several shocks and the final push by the main pulse. If we cast the  $\rho$ - $T$  history of the imploding DT shell onto the plane spanned by the coupling parameter  $\Gamma = 1/akT$  (where  $a$  is the Wigner-Seitz radius and  $k$  is the Boltzman constant) and the degeneracy parameter  $\theta = T/T_F$  (where  $T_F$  is the Fermi temperature), we find that the imploding shell indeed undergoes the coupled ( $\Gamma > 1$ ) and degenerate ( $\theta < 1$ ) regimes. It is therefore expected that the effects of strong coupling and degeneracy in such plasmas would affect the compression and fusion yield in low-adiabat ICF implusions.

The effects of strong coupling and degeneracy in ICF plasmas have recently attracted much attention since they may redefine the so-called “1-D physics” of ICF implusions. For example, the essential pieces of physics models used in ICF hydrosimulations, such as the electron-ion energy relaxation rate,<sup>8</sup> the thermal conductivity,<sup>9</sup> and the fusion-reaction rate<sup>10</sup> in coupled and degenerate plasmas, were recently re-examined. In recent experiments, the EOS of liquid deuterium along the principal Hugoniot around 100 to 200 GPa was measured using laser-driven shock waves,<sup>11–16</sup> magnetically driven flyers,<sup>17,18</sup> and convergent explosives.<sup>19,20</sup> Over the years, enormous theoretical efforts have been put forth to better understand the properties of deuterium under high pressure. The widely used *SESAME* EOS table of deuterium was based on the “chemical model” of matter,<sup>21,22</sup> which has adopted the liquid perturbation theory in the molecular/atomic fluid phase for ICF plasma conditions. The first-order expansion was originally used in the *SESAME* model<sup>21</sup> to take only the nearest-neighbor interactions into account, which did not fully account for the effects of strong coupling and many-body degeneracy in nonideal plasmas. *Ab initio* calculations for the deuterium EOS have been performed by using the method of density functional theory-based molecular dynamics (DFT-MD)<sup>23–30</sup> and the path-integral Monte Carlo (PIMC) method.<sup>31–35</sup> The first-principle methods take the strong-coupling and degeneracy effects fully into account, in contrast to using chemical models.<sup>21,22,36–39</sup>

For ICF applications, we are especially concerned about the EOS accuracy along the implosion path in the density-temperature plane, i.e., in the range of  $\rho \sim 0.1$  to 1000 g/cm<sup>3</sup> and  $T \sim 1.0$  to 1000 eV. For these plasma conditions, the DFT-based methods become very expensive because of the large number of electronic orbitals required,<sup>40</sup> while the EOS can be derived efficiently with the PIMC method. This article presents a first-principles equation-of-state (FPEOS) table of deuterium from restricted PIMC calculations.<sup>41</sup> The same method has been successfully applied to compute the deuterium EOS up to a density of  $\rho = 5.388$  g/cm<sup>3</sup> (Refs. 33 and 42) and has been

favorably compared with DFT-MD calculations.<sup>34</sup> We have used free-particle nodes to construct the many-body trial density matrix. The Coulomb interactions enter via a high- $T$  pair-density matrix<sup>43</sup>  $\rho(R, R'; \delta\beta)$ . Using its convolution property, the density matrix  $\rho(R, R'; \beta)$  can be expressed by

$$\rho(R, R'; \beta) = \int dR_1 dR_2 \dots dR_{M-1} \rho(R, R_1; \delta\beta) \times \rho(R_1, R_2; \delta\beta) \dots \rho(R_{M-1}, R'; \delta\beta) \quad (1)$$

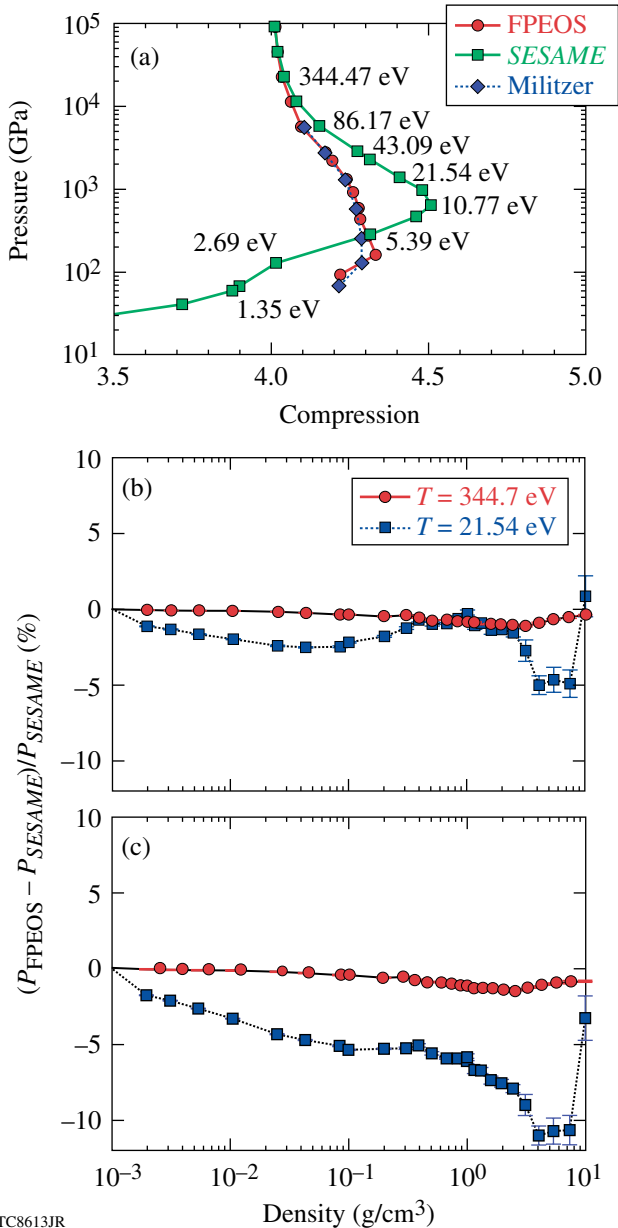
with  $\beta = 1/kT$  and  $\delta\beta = \beta/M$ , where  $M$  is the number of steps along the path in imaginary “time.” Monte Carlo methods are used to efficiently evaluate the multidimensional integration. Thermodynamic properties (associated with operator  $\hat{O}$ ) of plasmas are derived from

$$\langle \hat{O} \rangle = \frac{\int dR dR' \langle R | \hat{O} | R' \rangle \langle R' | \rho(R, R'; \beta) | R \rangle}{\int dR \langle R' | \rho(R, R'; \beta) | R \rangle}. \quad (2)$$

We have performed our PIMC calculations with various numbers of atoms in periodic cubic simulation cells depending on the deuterium-density ranges: 64 atoms for  $\rho < 2.5$  g/cm<sup>3</sup>, 128 atoms for  $2.5 < \rho < 10.5$  g/cm<sup>3</sup>, and 256 atoms for  $\rho > 10.5$  g/cm<sup>3</sup>. The time step  $\delta\beta$  was chosen small enough,  $1/\delta\beta \geq 75 \times kT_F$  to accurately account for interactions and degeneracy effects. Convergence tests have been done for each density range.

In Fig. 121.36(a), we compare the principal Hugoniot between our FPEOS table and the *SESAME* (5263) EOS for different temperatures marked on the curve. It is noted that this version of *SESAME* EOS is still used in ICF designs, although improvements have recently been made by Kerley.<sup>22</sup> We have also plotted the previous Hugoniot calculated using the same PIMC method with 32 atoms and a time step of  $1/\delta\beta = 8 \times 10^6$  K (Refs. 33 and 42). Good agreement is found with these previous PIMC calculations. Current PIMC simulations used 64 atoms and a smaller time step of  $1/\delta\beta = 1.6 \times 10^7$  K. We found that, according to our PIMC calculations, deuterium is slightly softer than the *SESAME* prediction for pressures below  $\sim 2$  Mbar, while it is stiffer in the pressure range of  $\sim 2 < P < 100$  Mbar (the dynamic compression range in ICF). The PIMC-predicted compression of  $\rho/\rho_0 \simeq 4.3$  below  $\sim 2$  Mbar agrees better with DFT-MD calculations<sup>26,28</sup> and EOS measurements using magnetically driven flyers.<sup>17,18</sup> It may also agree with the laser-shock results<sup>15,16</sup> after the quartz standard used in experiments is corrected.<sup>44</sup> To give an interpretation of these discrepancies, in Figs. 121.36(b) and 121.36(c) we have plotted the percentage differences in pressure and energy versus

density, for two temperatures  $T = 344.47$  eV and  $T = 21.54$  eV. The statistical error bars of our PIMC results are also marked. At  $T = 344.47$  eV, both the pressure and energy from PIMC and *SESAME* are within  $\sim 1\%$ . This is expected because plasmas at such high temperatures are classical ( $\Gamma \ll 1$ ,  $\theta \gg 1$ ), where both PIMC and *SESAME* should agree. The PIMC and *SESAME* Hugoniot curves above 344 eV are identical, as shown in



TC8613JR

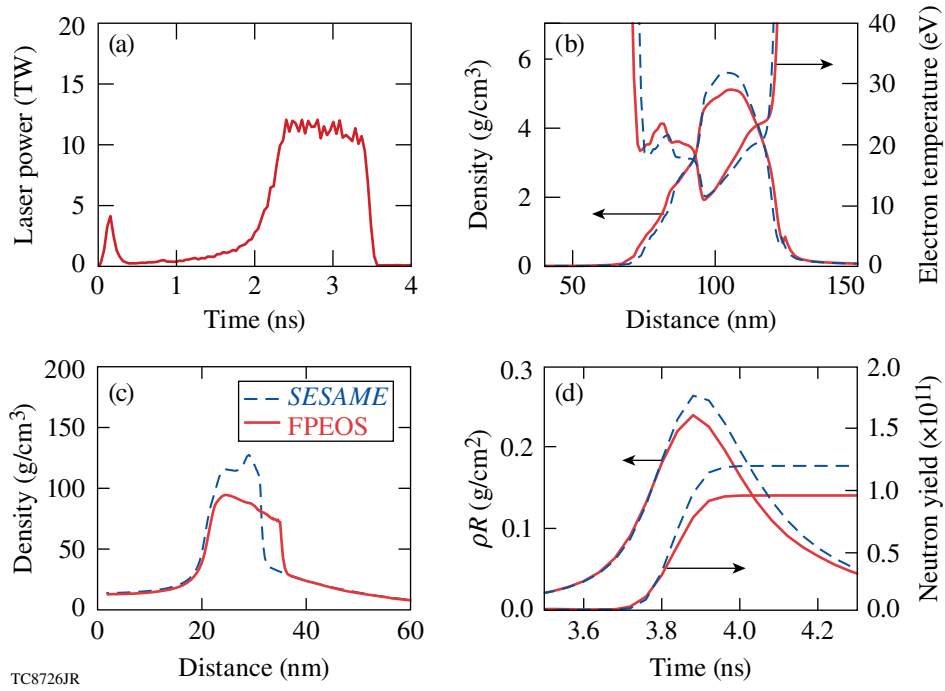
Figure 121.36

(a) The principal Hugoniot for liquid deuterium. The relative deviation in (b) pressure and (c) energy between the FPEOS and *SESAME* as a function of density, for temperatures  $T = 344.7$  eV (red circles) and  $T = 21.54$  eV (blue squares).

Fig. 121.36(a). For a lower temperature of 21.54 eV, however, the energy difference is larger, as indicated in Fig. 121.36(c). For the principal Hugoniot, in the density range of  $\rho = 0.6$  to  $0.8$   $\text{g/cm}^3$ , the internal energy in FPEOS is  $\sim 6\%$  lower than that of *SESAME* (for this comparison, the zero energy has been set to the ground state of an isolated molecule,  $E_0 = -15.886$  eV), even though the pressure is comparable in both within  $\sim 1\%$ . According to the Hugoniot equation [ $E_f - E_0 + (1/2)(P_f + P_0) \times (V_f - V_0) = 0$ ], the final state can be expressed as  $E_f + (1/2) \times P_f V_f \simeq E_0 + (1/2) P_f V_0$  because of  $P_f \gg P_0$ , where  $(P_0, E_0, V_0)$  and  $(P_f, E_f, V_f)$  are the initial and final pressure, energy, and volume of deuterium. Therefore, with the similar value of  $P_f$ , the smaller  $E_f$  predicted by the FPEOS requires larger  $V_f$  to satisfy the Hugoniot equation.<sup>45</sup> Larger  $V_f$  relative to the *SESAME* case means a smaller final density and compression, as seen in Fig. 121.36(a). Such discrepancy was noticed by Kerley<sup>22</sup> in 2003; with some improvements to the ionization equilibrium model adopted in *SESAME*, he succeeded in decreasing the *SESAME* compression to better agree with the first-principle calculations in this high-pressure ( $\sim 10$ -Mbar) regime.<sup>22</sup> The lower internal energy in FPEOS, for  $T < 100$  eV, is attributed to many-body interactions. Figure 121.36(c) indicates that as the density increases, the relative deviation in energy reaches a maximum of  $\sim 11\%$  around  $\rho \sim 4$  to  $5$   $\text{g/cm}^3$  ( $\Gamma \simeq 1.3$  and  $\theta \simeq 0.4$ ) for this isothermal curve at  $T = 21.54$  eV. The *SESAME* model again agrees with PIMC calculations at very high densities (e.g.,  $\rho = 10$   $\text{g/cm}^3$ ), as local screening was correctly accounted for in chemical models.<sup>21,22</sup>

From PIMC calculations, we have derived a first-principles EOS table for deuterium, which covers the typical ICF fuel conditions of  $\rho = 0.002$  to  $1596$   $\text{g/cm}^3$  and  $T = 1.35$  eV to  $5.5$  keV. For each density point, we have performed PIMC calculations including low temperature corresponding to  $\theta = T/T_F \simeq 0.1$ . To comply with the *SESAME* format used in our hydrocodes, we have added the experimentally benchmarked low- $T$  ( $< 1.35$ -eV) *SESAME* points to our FPEOS table, although those points are not actually used in ICF hydrocodes (except for defining the initial state). The high-temperature limit of  $T > 5.5$  keV is obtained by linearly extrapolating (in  $T$ ) the highest PIMC point since ideal plasma conditions are expected at high temperatures.

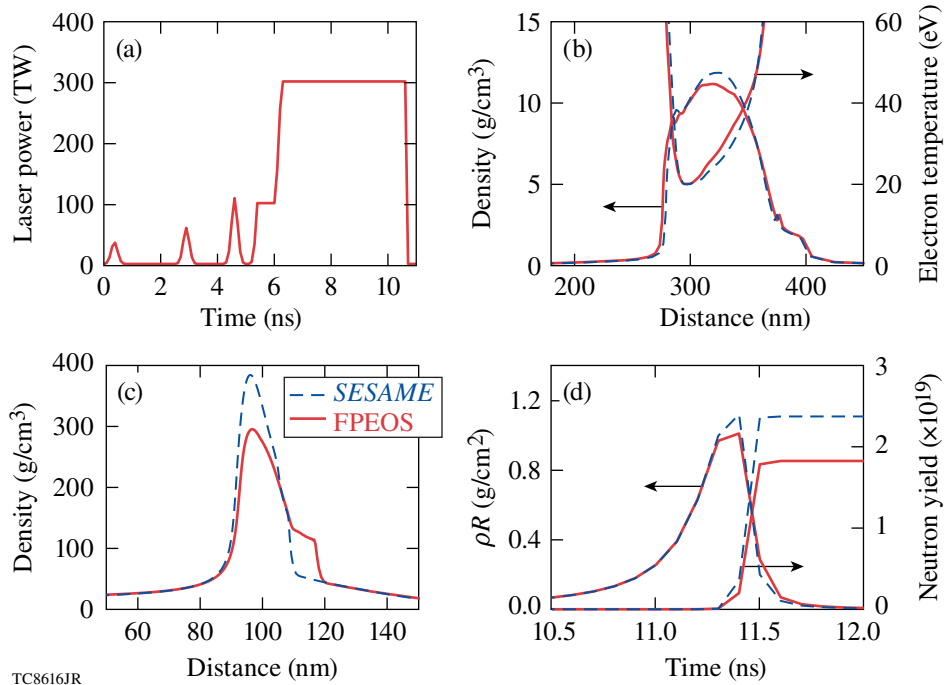
With our FPEOS table, we can now explore the implications of strong-coupling and degeneracy effects in ICF implosions using hydrocodes. Results are shown in Figs. 121.37 and 121.38, respectively, for a cryogenic  $\text{D}_2$  implosion ( $\alpha \simeq 2.5$ ) on the OMEGA Laser System and a direct-drive DT design on the NIF. We have used the 1-D radiative hydrocode *LILAC*<sup>46</sup> to



TC8726JR

Figure 121.37

The hydrocode simulations of a cryogenic D<sub>2</sub> implosion on OMEGA using the FPEOS table (solid red line) and the *SESAME* EOS table (dashed blue line): (a) the laser pulse shape; (b) the density and temperature profiles of the imploding D<sub>2</sub> shell at the end of laser pulse ( $t = 3.6$  ns); (c) the density profile at peak compression; and (d) the areal density ( $\rho R$ ) and neutron yield as functions of time.



TC8616JR

Figure 121.38

Similar to Fig. 121.37 but for a NIF direct-drive-ignition design.

perform these simulations. In Fig. 121.37(a), we plot the pulse shape used to implode a cryogenic  $D_2$  target (877- $\mu\text{m}$  diameter) with a 10- $\mu\text{m}$  CD ablator and 95  $\mu\text{m}$  of  $D_2$  ice. Figure 121.37(b) shows the density and temperature profiles at the end of the laser pulse ( $t = 3.6$  ns) from both the FPEOS and *SESAME* simulations. The shell's peak density and average temperature were  $\rho_p \sim 5 \text{ g/cm}^3$  and  $T \sim 15 \text{ eV}$ , which correspond to the strongly coupled and degenerate regime with  $\Gamma \simeq 1.7$  and  $\theta \simeq 0.3$ . It is shown that the FPEOS simulation predicted  $\sim 10\%$ -lower  $\rho_p$  but higher temperature relative to the *SESAME* prediction. As the Hugoniot comparison indicated in Fig. 121.36(a), the FPEOS is slightly stiffer than *SESAME* in this temperature range, which explains the lower  $\rho_p$ . The slightly higher temperature in the FPEOS case originated from the lower internal energy [see Fig. 121.36(c)]. Since the laser ablation does the work/energy to the shell compression and its kinetic motion, a lower internal energy in FPEOS means more energy is partitioned to heat the shell, thereby resulting in a slightly higher temperature. Such a temperature increase and density drop can have consequences in the implosion performance. At the stagnation stage (peak compression), Fig. 121.37(c) shows that the peak density is  $\sim 30\%$  lower according to FPEOS ( $\rho_p \simeq 90 \text{ g/cm}^3$ ) compared to *SESAME* ( $\rho_p \simeq 130 \text{ g/cm}^3$ ). The peak areal density  $(\rho R)_{\text{peak}}$  and neutron yield were also reduced by  $\sim 10\%$  to  $20\%$  as shown in Fig. 121.37(d). The neutron-averaged areal density  $\langle \rho R \rangle_n$  predicted with FPEOS was  $\sim 198 \text{ mg/cm}^2$ , which is in better agreement with the experimental measured  $\langle \rho R \rangle_n = 202 \pm 7 \text{ mg/cm}^2$  (Ref. 47), in contrast to the *SESAME* prediction of  $\langle \rho R \rangle_n = 247 \text{ mg/cm}^2$ . Nonuniformities cannot account for the large discrepancy between measurements and *SESAME* predictions, as we have noted that certain perturbations in experiments can reduce the neutron yield<sup>48</sup> but hardly affect the compression  $\rho R$ .

A similar effect was seen for the NIF designs. Figure 121.38 shows an example for a NIF target ( $\phi = 3.37 \text{ mm}$ ) having a 37- $\mu\text{m}$  CH ablator and 150  $\mu\text{m}$  of DT ice. At the end of the laser pulse [ $t = 10.7$  ns in Fig. 121.38(b)], we also found a decrease in  $\rho_p$  and a temperature increase for the FPEOS relative to *SESAME* simulations. The peak density near the stagnation dropped from  $\rho_p = 383 \text{ g/cm}^3$  (*SESAME*) to  $\rho_p = 294 \text{ g/cm}^3$  (FPEOS), as is indicated by Fig. 121.38(c). The resulting  $\rho R$  and neutron yield as a function of time are plotted in Fig. 121.38(d). The peak  $\rho R$  dropped from  $1.1 \text{ g/cm}^2$  (*SESAME*) to  $1.0 \text{ g/cm}^2$  (FPEOS), while the yield dropped from the *SESAME*-predicted value of  $Y = 2.4 \times 10^{19}$  to  $1.8 \times 10^{19}$  for the FPEOS simulation. Consequently, the energy gain dramatically decreased from 45 (*SESAME*) to 34 (FPEOS).

In summary, we have derived a first-principles equation-of-state table of deuterium for ICF applications from PIMC calculations. The FPEOS table covers the typical fuel density and temperature conditions in ICF implosions. In comparison with the *SESAME* table, the FPEOS predicts  $\sim 10\%$ -lower internal energy but comparable pressure (within few percent) for strongly coupled and degenerate plasma conditions. Hydrosimulations using the FPEOS table indicate significant decreases in the predicted peak density ( $\sim 30\%$  to  $40\%$ ). The results also show a reduction in the peak areal density  $\rho R$  ( $\sim 10\%$ ) and the neutron yield (energy gain) by  $\sim 20\%$  with respect to the corresponding *SESAME* simulations. The compression ( $\rho R$ ) predicted from FPEOS agrees better with experiments. The FPEOS table will become more important for even lower adiabat ( $\alpha \simeq 1$  to  $2$ ) ICF target designs since one expects strong coupling and degeneracy effects to increase in such plasmas.

#### ACKNOWLEDGMENT

This work was supported by U.S. Department of Energy Office of Inertial Confinement Fusion under Cooperative Agreement No. DE-FC52-08NA28302, the University of Rochester, and New York State Energy Research and Development Authority. S. X. Hu thanks the National Science Foundation for its support under the NSF-TeraGrid grant PHY090093. A portion of this research was carried out on the NICS' Kraken Supercomputer. B. Militzer acknowledges support from UC's laboratory research program, NSF, and NASA.

#### REFERENCES

1. S. Atzeni and J. Meyer-ter-Vehn, *The Physics of Inertial Fusion: Beam Plasma Interaction, Hydrodynamics, Hot Dense Matter*, International Series of Monographs on Physics (Clarendon Press, Oxford, 2004).
2. R. L. McCrory, D. D. Meyerhofer, R. Betti, R. S. Craxton, J. A. Delettrez, D. H. Edgell, V. Yu Glebov, V. N. Goncharov, D. R. Harding, D. W. Jacobs-Perkins, J. P. Knauer, F. J. Marshall, P. W. McKenty, P. B. Radha, S. P. Regan, T. C. Sangster, W. Seka, R. W. Short, S. Skupsky, V. A. Smalyuk, J. M. Soares, C. Stoeckl, B. Yaakobi, D. Shvarts, J. A. Frenje, C. K. Li, R. D. Petrasso, and F. H. Séguin, *Phys. Plasmas* **15**, 055503 (2008).
3. J. D. Lindl, *Phys. Plasmas* **2**, 3933 (1995).
4. S. X. Hu, V. A. Smalyuk, V. N. Goncharov, J. P. Knauer, P. B. Radha, I. V. Igumenshchev, J. A. Marozas, C. Stoeckl, B. Yaakobi, D. Shvarts, T. C. Sangster, P. W. McKenty, D. D. Meyerhofer, S. Skupsky, and R. L. McCrory, *Phys. Rev. Lett.* **100**, 185003 (2008).
5. S. X. Hu, V. A. Smalyuk, V. N. Goncharov, S. Skupsky, T. C. Sangster, D. D. Meyerhofer, and D. Shvarts, *Phys. Rev. Lett.* **101**, 055002 (2008).
6. T. R. Boehly, D. L. Brown, R. S. Craxton, R. L. Keck, J. P. Knauer, J. H. Kelly, T. J. Kessler, S. A. Kumpan, S. J. Loucks, S. A. Letzring, F. J. Marshall, R. L. McCrory, S. F. B. Morse, W. Seka, J. M. Soares, and C. P. Verdon, *Opt. Commun.* **133**, 495 (1997).

7. J. Paisner *et al.*, *Laser Focus World* **30**, 75 (1994).
8. M. S. Murillo and M. W. C. Dharma-wardana, *Phys. Rev. Lett.* **100**, 205005 (2008); M. W. C. Dharma-wardana, *Phys. Rev. Lett.* **101**, 035002 (2008); B. Jeon *et al.*, *Phys. Rev. E* **78**, 036403 (2008); G. Dimonte and J. Daligault, *Phys. Rev. Lett.* **101**, 135001 (2008); J. N. Glosli *et al.*, *Phys. Rev. E* **78**, 025401 (R) (2008); L. X. Benedict *et al.*, *Phys. Rev. Lett.* **102**, 205004 (2009).
9. V. Recoules *et al.*, *Phys. Rev. Lett.* **102**, 075002 (2009).
10. E. L. Pollock and B. Militzer, *Phys. Rev. Lett.* **92**, 021101 (2004).
11. L. B. Da Silva *et al.*, *Phys. Rev. Lett.* **78**, 483 (1997).
12. G. W. Collins *et al.*, *Science* **281**, 1178 (1998).
13. G. W. Collins *et al.*, *Phys. Plasmas* **5**, 1864 (1998).
14. A. N. Mostovych *et al.*, *Phys. Rev. Lett.* **85**, 3870 (2000); A. N. Mostovych *et al.*, *Phys. Plasmas* **8**, 2281 (2001).
15. T. R. Boehly, D. G. Hicks, P. M. Celliers, T. J. B. Collins, R. Earley, J. H. Eggert, D. Jacobs-Perkins, S. J. Moon, E. Vianello, D. D. Meyerhofer, and G. W. Collins, *Phys. Plasmas* **11**, L49 (2004).
16. D. G. Hicks, T. R. Boehly, P. M. Celliers, J. H. Eggert, S. J. Moon, D. D. Meyerhofer, and G. W. Collins, *Phys. Rev. B* **79**, 014112 (2009).
17. M. D. Knudson *et al.*, *Phys. Rev. Lett.* **87**, 225501 (2001); M. D. Knudson *et al.*, *Phys. Rev. Lett.* **90**, 035505 (2003).
18. M. D. Knudson *et al.*, *Phys. Rev. B* **69**, 144209 (2004).
19. S. I. Belov *et al.*, *JETP Lett.* **76**, 433 (2002).
20. V. E. Fortov *et al.*, *Phys. Rev. Lett.* **99**, 185001 (2007).
21. G. I. Kerley, *Phys. Earth Planet. Inter.* **6**, 78 (1972).
22. G. I. Kerley, Sandia National Laboratory, Albuquerque, NM, Report SAND2003-3613 (2003).
23. L. Collins *et al.*, *Phys. Rev. E* **52**, 6202 (1995).
24. T. J. Lenosky *et al.*, *Phys. Rev. B* **61**, 1 (2000).
25. G. Galli *et al.*, *Phys. Rev. B* **61**, 909 (2000).
26. L. A. Collins *et al.*, *Phys. Rev. B* **63**, 184110 (2001).
27. J. Cl rouin and J.-F. Dufr che, *Phys. Rev. E* **64**, 066406 (2001).
28. M. P. Desjarlais, *Phys. Rev. B* **68**, 064204 (2003).
29. S. A. Bonev, B. Militzer, and G. Galli, *Phys. Rev. B* **69**, 014101 (2004).
30. S. A. Bonev *et al.*, *Nature* **431**, 669 (2004).
31. C. Pierleoni *et al.*, *Phys. Rev. Lett.* **73**, 2145 (1994).
32. W. R. Magro *et al.*, *Phys. Rev. Lett.* **76**, 1240 (1996).
33. B. Militzer and D. M. Ceperley, *Phys. Rev. Lett.* **85**, 1890 (2000).
34. B. Militzer *et al.*, *Phys. Rev. Lett.* **87**, 275502 (2001).
35. V. Bezukrovnyy *et al.*, *Phys. Rev. E* **70**, 057401 (2004); V. S. Filinov *et al.*, *Plasma Phys. Rep.* **31**, 700 (2005).
36. D. Saumon and G. Chabrier, *Phys. Rev. A* **46**, 2084 (1992).
37. M. Ross, *Phys. Rev. B* **58**, 669 (1998).
38. F. J. Rogers, *Contrib. Plasma Phys.* **41**, 179 (2001).
39. H. Juranek, R. Redmer, and Y. Rosenfeld, *J. Chem. Phys.* **117**, 1768 (2002).
40. L. A. Collins, Los Alamos National Laboratory, private communication (2009).
41. D. M. Ceperley, *Rev. Mod. Phys.* **67**, 279 (1995).
42. B. Militzer, "Path Integral Monte Carlo Simulations of Hot Dense Hydrogen," Ph.D. thesis, University of Illinois at Urbana-Champaign, 2000.
43. B. Militzer, "Computation of the High Temperature Coulomb Density Matrix in Periodic Boundary Conditions," to be published in *Physical Review E*.
44. M. D. Knudson and M. P. Desjarlais, *Phys. Rev. Lett.* **103**, 225501 (2009).
45. B. Militzer, *Phys. Rev. Lett.* **97**, 175501 (2006).
46. J. Delettrez, R. Epstein, M. C. Richardson, P. A. Jaanimagi, and B. L. Henke, *Phys. Rev. A* **36**, 3926 (1987).
47. T. C. Sangster, V. N. Goncharov, P. B. Radha, V. A. Smalyuk, R. Betti, R. S. Craxton, J. A. Delettrez, D. H. Edgell, V. Yu. Glebov, D. R. Harding, D. Jacobs-Perkins, J. P. Knauer, F. J. Marshall, R. L. McCrory, P. W. McKenty, D. D. Meyerhofer, S. P. Regan, W. Seka, R. W. Short, S. Skupsky, J. M. Soures, C. Stoeckl, B. Yaakobi, D. Shvarts, J. A. Frenje, C. K. Li, R. D. Petrasso, and F. H. S guin, *Phys. Rev. Lett.* **100**, 185006 (2008).
48. S. X. Hu, P. B. Radha, J. A. Marozas, R. Betti, T. J. B. Collins, R. S. Craxton, J. A. Delettrez, D. H. Edgell, R. Epstein, V. N. Goncharov, I. V. Igumenshchev, F. J. Marshall, R. L. McCrory, D. D. Meyerhofer, S. P. Regan, T. C. Sangster, S. Skupsky, V. A. Smalyuk, Y. Elbaz, and D. Shvarts, *Phys. Plasmas* **16**, 112706 (2009).

---

# Neutron-Induced Nucleation Inside Bubble Chambers Using Freon 115 as the Active Medium

## Introduction

The vast majority of controlled fusion experiments worldwide involve deuterium–tritium (DT) or deuterium–deuterium (DD) mixtures.<sup>1</sup> Nuclear diagnostics provide a direct measurement of the DD or DT fusion burn within a compressed inertial confinement fusion (ICF) target.<sup>2</sup> These diagnostics are used to infer the fuel areal density, neutron yield, fuel-ion temperature, and bang time.<sup>2</sup> Neutrons are a primary fusion-reaction product that can provide an image of the fusion burn region. Neutron imaging (NI) can be used to determine failure modes of ICF ignition capsules, such as poor implosion symmetry or improper laser pulse shaping.<sup>3,4</sup> NI has been used on OMEGA<sup>5</sup> to measure the core symmetry of gas-filled plastic shells and cryogenic target implosions.<sup>6</sup> NI systems use extended pinholes or penumbral apertures (with annular apertures as a particular case) to capture images on a neutron-sensitive detector.<sup>4</sup> They are sensitive to both alignment and fabrication errors of the apertures used.<sup>7</sup>

A neutron image provides a direct measurement of the spatial extent of the fusion burn area for an ICF implosion, drawn from the physical characteristics of the neutrons that exit the plasma core as primary or secondary products of the fusion reactions.<sup>4</sup> The core image is obtained by placing an appropriate aperture in front of a spatially sensitive neutron detector. The apertures are typically coded.<sup>4</sup> The neutrons are detected by a plastic scintillator<sup>6</sup> array or a bubble chamber.<sup>8</sup>

In NI systems, the coded image must be deconvolved to produce an accurate representation of the neutron source. This process requires precise knowledge of the aperture point-spread function (PSF) and the flat-field response of the imaging detector.<sup>3</sup> Both pinhole and penumbral apertures are used.<sup>7</sup> For both pinholes and penumbral apertures, uncertainties in the exact shape (caused by finite fabrication tolerances) lead to errors in the reconstructed image because of uncertainties in the calculated PSF. A computational study<sup>7</sup> previously investigated the influences of various parameters from the NI system on the quality of the reconstructed image.

The required spatial resolution for an imaging system can be determined from numerical simulations.<sup>2</sup> A resolution of about  $10\ \mu\text{m}$  appears to provide sufficient information to validate implosion models, but a resolution of  $5\ \mu\text{m}$  may be necessary to see details in the implosion structure.<sup>2</sup> Previous studies<sup>8</sup> have already shown that bubble chambers have the potential to obtain higher-resolution images of the targets for a shorter source–target distance than typical scintillator arrays and could be used for the very high neutron yields ( $\geq 10^{16}$ ) expected to be measured at the National Ignition Facility (NIF).

This article discusses the mechanism of neutron-induced bubble formation inside Freon 115 and the influence of the critical radius size on the neutron detection sensitivity. Two forthcoming publications will focus on the design of the liquid Freon bubble chamber used on OMEGA and the data recorded with the detector, respectively.<sup>9,10</sup>

## Interactions of Neutrons with Freon 115— A Simplified Model

Freon 115 (chloropentafluoroethane,  $\text{C}_2\text{F}_5\text{Cl}$ ) has been used as the active medium in bubble chambers for high-energy-physics experiments at the European Organization for Nuclear Research (CERN) since the early 1980s.<sup>11</sup> It is nonflammable, inexpensive, safe to operate, and easy to store in compressed gas tanks. A Freon 115 bubble chamber does not need cryogenic cooling and can be operated at around  $50^\circ\text{C}$ .

### 1. Thermodynamic Conditions for Bubble Formation

A bubble chamber is initially pressurized with its active medium in a liquid state. Several milliseconds before the incident particles enter the chamber, the pressure is quickly decreased and the liquid enters a superheated, metastable phase. The temperature becomes higher than its standard boiling point, without actually boiling. Deposition of small quantities of energy by incident particles or by any heterogeneous nucleation sites such as gas pockets or impurities disturbs the energy balance in the liquid and locally vaporizes the liquid. Because the vapor pressure is higher than the surrounding liquid pressure, the

newly formed bubble tends to expand, but the expansion force is counterbalanced by the surface tension force at the gas–liquid boundary.<sup>12</sup> Other factors influencing the bubble growth are the viscosity force that slows down the bubble expansion and the force transmitted to the bubble growth from the bubble/wall interaction. If the radius of the generated bubble is greater than a certain critical value  $R_c$ , the force balance is dominated by the vapor pressure and the bubble continues to grow (otherwise the bubble is reabsorbed into the liquid). As a fraction of the chamber volume vaporizes through the nucleation process, the liquid pressure inside the active medium increases until a balance is reached for a bubble radius of macroscopic size. After a short interval of time (usually a few tens of milliseconds), the bubbles fill the chamber and the boiling spreads to the whole liquid volume.<sup>12</sup> The chamber has to be repressurized to clean the gas pockets resulting from boiling and then decompressed again to take a new set of data. For the particular case of a gel detector, the active medium is represented by tiny pressurized liquid drops suspended in a transparent gel. Due to the higher pressure, these drops are in a superheated state and each of them behaves as a miniature bubble chamber.<sup>12</sup> The mechanism of bubble formation works in the same way as a liquid bubble chamber.<sup>8</sup>

The minimum energy  $E_b$  necessary for the formation of a bubble of critical radius  $R_c$  is described by<sup>13,14</sup>

$$E_b = W_b + H + E_{\text{wall}} + E_{\text{visc}}, \quad (1)$$

where  $W_b$  is the minimum reversible work required for bubble formation,  $H$  is the vaporization energy,  $E_{\text{wall}}$  is the kinetic energy transmitted to the liquid during the growth process, and  $E_{\text{visc}}$  is the energy lost during the bubble growth by viscous forces.<sup>15</sup>  $E_{\text{wall}}$  and  $E_{\text{visc}}$  can be neglected in this work.<sup>16,17</sup> During the nucleation process, the bubble forms so rapidly that there is no time for energy exchange to take place between the bubble and the surrounding liquid.<sup>14</sup> Once the bubble is initiated, the energy required to maintain it is given by the minimal reversible work  $W_b$  expressed as

$$W_b = 4\pi r^2 \gamma(T) - \frac{4}{3}\pi r^3 (p_v - p_0), \quad (2)$$

where  $\gamma(T)$  is the liquid–vapor interfacial tension (temperature dependent),  $p_v$  is the vapor pressure of the superheated liquid, and  $p_0$  is the ambient liquid pressure. The difference  $p_v - p_0$  is called the degree of superheat of a given liquid.  $W_b$  is minimized for a critical radius

$$R_c = \frac{2\gamma(T)}{p_v - p_0}. \quad (3)$$

When a bubble reaches its critical radius, its vapor pressure is greater than its surface tension force. It becomes thermodynamically unstable and grows quickly. Once the liquid has vaporized locally, the minimum amount of energy  $W_b$  needed to form a vapor bubble of critical size  $R_c$ , as given by Gibbs (1875)<sup>13</sup> from reversible thermodynamics, is

$$W_b = \frac{16\pi\gamma^3(T)}{3(p_v - p_0)^2}. \quad (4)$$

The vaporization energy can be expressed as<sup>14,18</sup>

$$H = \frac{4}{3}\pi R_c^3 \rho_v H_v \quad (5)$$

with  $\rho$  the vapor density and  $H_v$  the latent heat of vaporization. Replacing Eqs. (4) and (5) in Eq. (1) and neglecting the kinetic and viscous energies, the minimum energy necessary to produce a bubble can be expressed as

$$E_b = \frac{16\pi\gamma^3(T)}{3(p_v - p_0)^2} + \frac{4}{3}\pi R_c^3 \rho_v H_v. \quad (6)$$

Equation (6) can be rewritten as

$$E_b = W_b \left( 1 + \frac{\rho_v H_v}{p_v - p_0} \right). \quad (7)$$

Equation (7) accounts for the conversion efficiency ( $\eta$ ) of heat to work, described by the relation

$$\eta = \frac{W_b}{E_b}. \quad (8)$$

For typical superheated liquids (Freon 12, Freon 115, Freon 134a), the value of  $\eta$  ranges from 2% to 6%.<sup>19</sup> The energy necessary to create a bubble,  $E_b$ , is supplied through the energy deposition per unit length  $dE/dx$  by the electrons ejected by the recoil nuclei.<sup>18</sup> The bubble nucleation requirements for a superheated medium are satisfied if the incident particle deposits enough energy to create a bubble within a specified length  $L$ , given by

$$L = k_b \cdot R_c, \quad (9)$$

where  $k_b$  is a constant that may vary between 2 and 13, in most cases being approximated as 2 (Refs. 16 and 19). The nucleation requirement is satisfied if [cf. Eq. (8) and (9)]

$$\frac{dE}{dx} \geq \frac{E_b}{k_b \cdot R_c} = \frac{W_b}{\eta \cdot k_b \cdot R_c}. \quad (10)$$

The condition necessary to create a bubble can be expressed as a minimum energy density  $\rho_E$  deposited over a sphere of radius  $R_c$ :

$$\rho_E \geq \frac{3E_b}{4\pi R_c^3}. \quad (11)$$

Replacing the values for the Freon 115 bubble chamber at 50°C (Ref. 20) (the operating temperature of the OMEGA bubble detector<sup>9,10</sup>) in Eq. (6), the critical radius is  $R_c = 7.5 \times 10^{-9}$  m and the minimum energy necessary to generate a bubble is  $E_b = 107$  eV.

Bubble chambers operate at a quasi-constant temperature and therefore behave as isothermal systems.  $W_b$  can be obtained from the difference between the liquid pressure in the superheated state and the pressure of the foam limit.<sup>21,22</sup> A bubble chamber is sensitive to particle detection only in its superheated state. The conditions necessary to reach this state depend on the thermodynamic-phase diagram of the liquid used as the active medium. Figure 121.39 shows the phase diagram for Freon 115.<sup>22</sup> The medium is in the liquid state above the vapor pressure line, gaseous below the foam limit line, and in a metastable coexistence state in the middle. During the bubble chamber operation the temperature is held constant while the pressure decreases quickly from a point on the upper curve (start/stable) to a value close to the lower curve (working unstable), where it is ready to record any interactions with the incident particles. The detector sensitivity and the bubble growth speed depend on temperature. Measurements made at CERN in the 1980s found that the bubble density for Freon 115 reaches maximum at 48°C (Ref. 22). For the bubble detector used on OMEGA,<sup>9,10</sup> the position of the piston during the decompression and the quantity of the Freon inside the chamber suggested that an operating temperature of 50°C was optimal.

The lines of constant bubble density come closer to the foam limit at higher temperatures. For a different active medium, the nominal values described in Fig. 121.39 may vary widely, but all liquid bubble chambers operate with the same principle. The foam limit is reached at the pressure  $p^*(T)$ , which is estimated, according to Bugg,<sup>23</sup> to be

$$p^*(T) = P_v - K \sqrt{\frac{k_L T}{\gamma^3}}, \quad (12)$$

where  $p_v$  and  $\gamma$  are the vapor pressure and surface tension, respectively, at the temperature  $T$ ,  $k_L$  is the thermal conductivity of the liquid, and  $K$  is a numerical proportionality constant determined experimentally (in most cases close to 1).

The bubble growth rate can be estimated from the formula deduced by Plesset and Zwick:<sup>24</sup>

$$r = A \sqrt{t} \quad (13)$$

with

$$A = 2 \sqrt{\frac{3}{\pi}} \sqrt{k_L \rho c_l (T_\infty - T_b)} / H_v \rho', \quad (14)$$

where  $k_L$  is the thermal conductivity of the liquid,  $\rho$  is its density,  $c_l$  is the specific heat,  $H_v$  is the heat of vaporization,  $\rho'$  is the density of the gas,  $T_\infty$  is the temperature of the liquid, and  $T_b$  is the temperature of the bubble (at the same pressure). The difference,  $T_\infty - T_b$ , decreases as the temperature increases. Equation (14) shows that the bubble growth rate decreases with increasing temperature. The effect of bubble movement caused by buoyancy forces and the effect of the spatial variation of the pressure during the bubble chamber cycle have been neglected during the bubble growth process.<sup>22</sup> Table 121.X, adapted from Ref. 22, shows the change of  $A$  as a function of temperature.

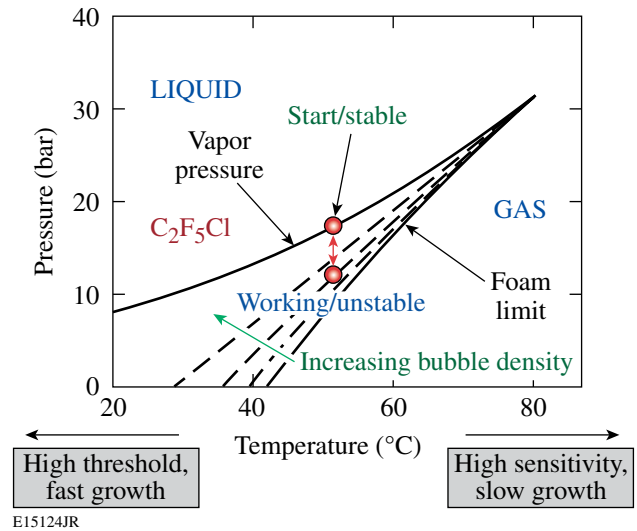


Figure 121.39

Bubble production as a function of pressure and temperature in a Freon 115 bubble chamber. The working region is the area between the vapor pressure line and the foam limit line. The dashed lines represent lines of constant bubble density (adapted from Ref. 20).

Table 121.X: Heat content and bubble growth rate for Freon 115 and hydrogen as functions of temperature (from Ref. 19).

Liquid	Temperature	$A(\text{cm}/\sqrt{\text{s}})$	Heat content (cal)
$\text{C}_2\text{F}_5\text{Cl}$	48°C	0.35	$1.2 \times 10^{-5}$
	55°C	0.10	$5.0 \times 10^{-7}$
	60°C	0.046	$5.9 \times 10^{-8}$
	65°C	0.023	$8.6 \times 10^{-9}$
$\text{H}_2$	29 K	0.095	$9.3 \times 10^{-8}$

Equations (13) and (14) show that the development of an average bubble radius depends on both the temperature and time after initiation as shown in Fig. 121.40. From the temperature fluctuations inside the chamber, an active medium (Freon 115) variation range for parameter  $A$  was estimated. A temperature difference of 0.2°C between two Freon regions inside the chamber induces a 2% difference in the bubble-growth speed.

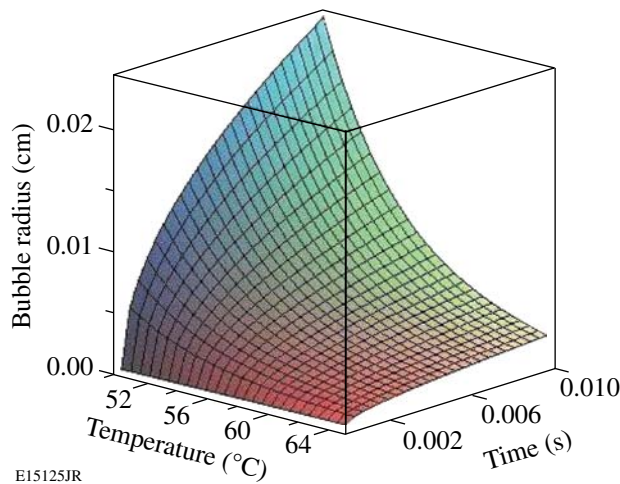


Figure 121.40  
The average bubble radius as a function of temperature and time for Freon 115.

## 2. The Thermodynamic Mechanism of Bubble Formation in Freon 115

The mechanism of bubble generation inside a bubble chamber depends on the production of highly localized regions where heat is released (“temperature spikes”) within the active medium. These areas quickly expand into bubbles larger than the critical radius  $R_c$  [described by Eq. (3)] and grow through the evaporation of the superheated liquid.<sup>18</sup>

An incident neutron will interact with the sensitive medium inside a bubble chamber as follows:<sup>18</sup>

1. A percentage of the neutrons that reach the liquid scatter elastically off the nuclei of the constituent molecules. During this interaction, the neutrons eject charged nuclei from these molecules (C, F, Cl for Freon 115).
2. The ejected nuclei interact with molecules of the active medium, freeing nuclei or electrons from the medium atoms or moving the bound electrons to excited states.
3. The ejected electrons lose their energy inside the medium over a distance proportional to their initial velocity, ejecting more electrons. The recombination of the free electrons and ions/nuclei or the return of the electrons from their excited states to stable energy levels release energy that behaves as a “temperature spike.” When these processes occur in a quasi-spherical zone of volume  $\sim R_c^3$ , a bubble is generated.

The number of bubbles produced inside a neutron detector depends on the neutron path inside the active medium (directly related to the bubble chamber’s size), the neutron yield, the geometry of the experiment (the distance from the neutron source to the detector influences the solid angle), and the efficiency of the bubble creation mechanism by the incident neutrons. From previous experimental measurements, the total neutron-scattering cross sections are known to be  $S_C = 1.30$  barn for carbon,  $S_{Cl} = 2.0$  barn for chlorine, and  $S_F = 0.053$  barn for fluorine.<sup>25</sup> The total cross section is  $S_t = 4.865$  barn for a Freon molecule (8 atoms) that has a mass of  $M = 154.5$  atomic units. The total cross section of the medium can be estimated from the detector volume. By taking the ratio between the total cross section and the detector cross section, the fraction of the incident neutrons interacting with the medium is determined.

To create a bubble, the energy released by the neutron has to reach the value  $E_b$  described in Eq. (5). Elastic collisions are described by a set of equations describing the conservation of momentum and energy:

$$m_n v_n + m_i v_i = m_n v'_n + m_i v'_i \tag{15}$$

$$\frac{m_n v_n^2}{2} + \frac{m_i v_i^2}{2} = \frac{m_n v'^2_n}{2} + \frac{m_i v'^2_i}{2},$$

where  $m$  and  $v$  represent the mass and velocity, with the indices “n” and “i” standing for the neutron and the recoil ion, respectively, and the prime annotation indicating the particles after interaction. The Freon molecules are at rest compared with the

high velocity of the incident neutrons,  $v_i = 0$ , and the maximum velocity of the recoil ion is (for a  $180^\circ$  scattering angle)

$$v_i' = \frac{2m_n v_n}{m_n + m_i}. \quad (16)$$

A fraction of the incident neutrons will interact with the Freon and eject nuclei from its molecules. Based on the 14.1-MeV initial energy of the neutrons and the dynamics of the elastic scattering, the final kinetic energy of the ejected nuclei can range from 0 MeV to  $\sim 4$  MeV for the carbon ions (the lightest components from the Freon molecule). It takes 2 keV to 5 keV to completely ionize an atom of C, Cl, or F (only 11 to 17 eV to singly ionize it, depending on the atom species), so, for a first approximation, the ionization energies can be neglected.

The stopping power for heavy-charged particles in the classical regime (with  $E \ll m_0 c^2$ ) is described by the Bethe–Bloch equation<sup>26,27</sup>

$$S_i = \frac{Zz^2 e^4 N_A m_i}{8\pi \epsilon_0^2 m_e E_{\text{kin}} M_A} \cdot \rho \cdot \ln \left( \frac{3m_e E_{\text{kin}}}{2\bar{T} m_i} \right), \quad (17)$$

where the stopping power is expressed in MeV/cm,  $Z$  is the atomic number of target atoms,  $z$  is the atomic number of the charged particle,  $N_A$  is Avogadro's constant ( $\text{mol}^{-1}$ ),  $m_e$  is the rest mass of the electron (kg),  $\epsilon_0$  is the electric permittivity of free space ( $C \cdot V^{-1} \cdot m^{-1}$ ),  $E_{\text{kin}}$  is the kinetic energy of the particle (J),  $M_A$  is the molar mass of the target ( $\text{g/mol}$ ),  $\bar{T}$  is the mean ionization energy (J),  $\rho$  is the medium density ( $\text{kg/m}^3$ ), and  $e$  is the electron charge.

Using the SRIM software designed by James Ziegler (<http://www.srim.org>, based on the Bethe–Bloch equation and experimental data from many sources), the scattered ion range was found to be between  $\sim 0 \mu\text{m}$  and  $9 \mu\text{m}$ , depending on the atom type and recoil ion energy. Each bubble produced inside the active medium expands from a very small volume associated with the transfer of the threshold energy  $E_b$  to either an electron or a nucleus from the incident particle as a result of Rutherford scattering.

The case where a recoil ion ejects further nuclei from the active medium molecules deserves a quick analysis. The cross section  $\sigma_p$  for ejecting a nucleus varies with  $1/E_c$  in the Rutherford range, where  $E_c$  is the kinetic energy of the incident particle.<sup>18</sup> For a given energy  $E \geq E_b$ , a simple calculation of

the ratio of the cross sections necessary to eject a nucleus and an electron is given by<sup>18</sup>

$$\frac{\sigma_p}{\sigma_e} = \frac{n_m m_e}{Z_e M_n}, \quad (18)$$

where  $n_m$  is the number of nuclei per molecule,  $m_e$  is the electron mass,  $Z_e$  is the number of electrons per molecule (the sum of the component atomic numbers), and  $M_n$  is the mass of the nucleus. The average mass for the nucleus of a Freon 115 molecule is  $M_n = 19.3$  and  $Z_e = 74$ . Replacing all the values in Eq. (6), the obtained interaction cross-section ratio is  $\sigma_p/\sigma_e \cong 3 \times 10^{-6}$ . The fraction of the ejected nuclei that produce bubbles is only  $3 \times 10^{-6}$  of the number of electrons creating bubbles, so it can be neglected. Essentially all the bubbles generated by incident neutrons originate from free electrons ejected by recoil ions.

To measure the energy transferred to electrons by an ejected nucleus, one has to know the stopping power for a particle moving inside a medium. This is defined as the differential energy loss  $dE$  along the path element  $dx$ :<sup>27</sup>

$$S = -\frac{dE}{dx}. \quad (19)$$

Using data obtained from simulations with the SRIM software, the stopping power's dependence on the ion energy has been plotted in Fig. 121.41.

To satisfy the minimum nucleation conditions, Eq. (9) must be true for the ion energy loss inside the superheated medium. If minimum energy loss/distance to create a bubble is written as  $L_b$  and the energy loss/distance for the recoil ion as  $L_i$ , the nucleation condition is satisfied for  $L_i \geq L_b$ . When this is satisfied, it does not mean that a bubble is created since bubble formation requires the electrons resulting from the recoil ion collision with the medium molecule electronic layers to have both the minimum nucleation energy and the minimum range, while the nucleation centers are too close to each other and will fuse quickly into a single visible bubble. In most cases, however,  $L_i \leq L_b$  and the nucleation occurs with a probability depending on the energy loss per volume since Eq. (10) also needs to be satisfied. For the case of ions with low energies (valid for the case of 14-MeV neutron detection inside Freon 115), the number of bubbles generated by a recoil ion moving over a distance equal to the critical diameter can be expressed as

$$N_i = \alpha \cdot \left(\frac{L_i}{L_b}\right)^3, \quad (20)$$

where the third power is due to the volumes' ratio and  $\alpha$  is a proportionality coefficient representing the energy conversion efficiency from the free electrons to the medium. Based on previous literature,<sup>12,14</sup> this conversion efficiency is close to 1 and the bubbles' density depends on the energy loss of the ejected ions inside the superheated medium.

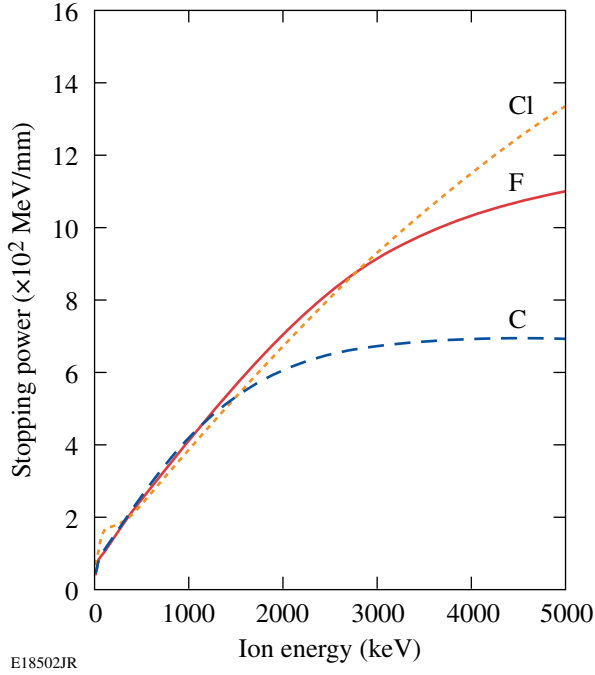


Figure 121.41  
The total stopping power derived from SRIM simulations for ions of carbon, fluorine, and chlorine inside Freon 115.

### 3. The Stopping Power for Electrons Inside Freon 115

For electrons, the stopping power is calculated using the adapted Bethe–Bloch formula and expressed in MeV/mm (Ref. 27):

$$S_e = \frac{Ze^4 N_A}{8\pi\epsilon_0^2 m_e v^2 M_A} \cdot \rho \cdot \ln \left[ \frac{m_e v^2 E_{kin}}{\bar{I}^2 (1 - \beta^2)} \right] + f(\beta), \quad (21)$$

where  $Z$  is the atomic number of the target atom,  $N_A$  is the Avogadro's constant ( $\text{mol}^{-1}$ ),  $m_e$  is the rest mass of the electron (kg),  $\epsilon_0$  is the electric permittivity of free space ( $C \cdot V^{-1} \cdot m^{-1}$ ),  $E_{kin}$  is the kinetic energy of the electron (J),  $M_A$  is the molar mass of the target (g/mol),  $\bar{I}$  is the mean ionization

energy (J),  $v$  is the electron velocity (m/s),  $\rho$  is the medium density ( $\text{kg}/\text{m}^3$ ),  $e$  is the electron charge,  $\beta = v/c$  with  $c$  the speed of light, and  $f(\beta)$  is a relativistic correction function.

Using the ESTAR program designed by the National Institute of Standards and Technology (NIST) (<http://physics.nist.gov>), based on Eq. (21) and experimental measurements, the electron range  $r_e$  is multiplied by the density to give an areal density and is calculated by ESTAR in a similar way and displayed in Fig. 121.42(a). This value can be misleading since the electrons interact with the medium and do not move on straight trajectories. The actual range is about 30% less than that calculated by ESTAR. The electron stopping power inside Freon 115, normalized to the medium density, was calculated as shown in Fig. 121.42(b).

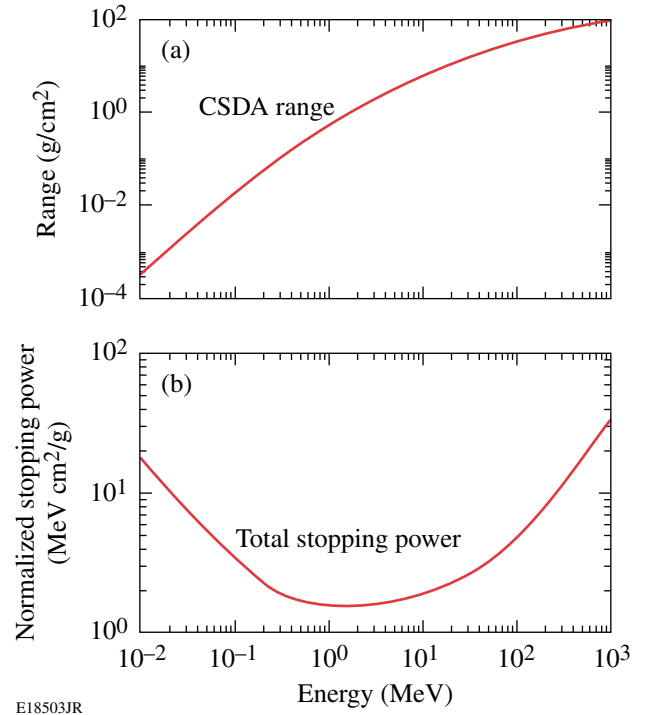


Figure 121.42  
(a) The electron range multiplied by density inside Freon 115 and (b) the total stopping power for electrons inside Freon 115, normalized to the medium density.

The expression for the cross section (in  $\text{cm}^2$ ) for an interaction between a nucleus and an electron (derived from the Rutherford formula) is (adapted from Ref. 18)

$$\sigma_{e,m} = 18.74 \times 10^{21} \frac{Z_e R_h}{E_b \beta^2} (\text{cm}^2), \quad (22)$$

where  $Z_e$  is the number of electrons/molecule,  $R_h$  is the Rydberg energy (13.6 eV),  $E_b$  is the threshold energy to create a bubble, and  $\beta$  is the ratio between the velocity of the incident particle (recoil ion)  $v$  and the speed of light  $c$ . As expressed by Eq. (22),  $\sigma_{e,m}$  decreases with the recoil ion velocity.

Cross section, molecule concentration, and average molecular radius can be calculated from the medium density and molar mass. The fraction of electrons with energies high enough to cross a distance equal to the critical bubble diameter can be then expressed as

$$\alpha = \frac{\sigma_{e,m}}{\sigma_{\text{mol}}} \cdot \frac{r_d}{2R_c}, \quad (23)$$

where  $\sigma_{\text{mol}}$  is the molecule cross section,  $r_d$  is the ion recoil distance, and  $R_c$  is the bubble's critical radius. Combining Eqs. (20) and (23), the number of bubbles generated by a recoil ion becomes

$$N_i = \frac{\sigma_{e,m}}{\sigma_{\text{mol}}} \cdot \frac{r_d}{2R_c} \cdot \left( \frac{L_i}{\beta L_b} \right)^3. \quad (24)$$

Extending the calculations for a neutron detector, the sensitivity of a bubble chamber to neutrons can be expressed as

$$\begin{aligned} \frac{N_{\text{bubbles}}}{n_{\text{source}}} &= F_n \cdot N_i \cdot d\Omega \\ &= F_n \cdot \frac{\sigma_{e,m}}{\sigma_{\text{mol}}} \cdot \frac{r_d}{2R_c} \cdot \left( \frac{L_i}{\beta L_b} \right)^3 d\Omega, \end{aligned} \quad (25)$$

where  $F_n$  is the fraction of the incident neutrons interacting with the active medium and  $d\Omega$  is the detector's solid angle. If this mechanism of bubble formation is valid, the value of  $N_{\text{bubbles}}/N_{\text{source}}$  can range between  $10^{-5}$  for a gel detector and  $10^{-3}$  for a liquid detector. Unfortunately, as shown below, Eqs. (24) and (25) work only for a gel detector and for some liquid detectors. Freon 115 has a very small critical radius so the energy density required to generate a bubble cannot be reached based on the stopping power of the electrons ejected by the recoil ions.

### The Mechanism of Bubble Formation for a Small Critical Radius

For nucleation to occur, the operating conditions must be in the thermodynamic limit, with critical radii in the range of

20 nm or larger and bubble threshold energies in the range of 1 keV or higher. An electron ejected by an incident particle ejects other electrons with relatively low energies. The incoming electron interacts with the orbital electrons in the medium, producing multiple new electrons (and ions) with lesser energy; each of these then interacts in the same way—a process that continues until many low-energy particles are produced. These are then stopped in the medium and absorbed. This process is known as a particle shower.

For very small critical radii, the volume of the critical bubble encloses only a few tens of molecules and the thermodynamic equations of bubble formation do not describe the nucleation process accurately. For example, for the case of Freon 115 at 50°C, the critical radius for bubble formation is 7 nm. Although the threshold energy for bubble generation decreases to ~100 eV for this volume, an electron with such a low energy has a range that is much less than the critical diameter. Its energy is transmitted to the medium over a range much smaller than the critical radius, and the bubble will collapse before it can nucleate. Even though an electron with a higher energy (500 eV) has a recoil range comparable to a critical bubble diameter, most of its energy will be lost while ejecting a small number of low-energy electrons that are immediately absorbed.

The software package CASINO (Monte Carlo simulation of electrons in solids, available for download at <http://www.srim.org/SREM.htm>), designed by Raynald Gauvin (Université de Sherbrooke, Québec, Canada), was used to calculate the electron ranges in Freon 115 at low energies. The average range of the electrons is ~14 nm (i.e., twice the critical radius). Electrons with energies higher than 500 eV will dissipate their energies over radii larger than the critical radius, while electrons with energies lower than 500 eV will not have enough energy to generate a shower of secondary particles that could fill the volume of a critical-radius bubble. For this reason, any generated micro bubble will quickly collapse before it can be observed. The mechanism of bubble formation based on the ejected electrons' stopping power does not work for media with a small critical radius, such as Freon 115.

For high-energy recoil ions, the dominant process that generates bubbles consists in the excitation of active medium molecules' electronic levels. This happens for energy values in excess of<sup>18</sup>

$$E_{\text{ex}} = \frac{M_i Z_i E_e}{m_e}, \quad (26)$$

where  $M_i$  is the mass of the incident particle (recoil ion),  $Z_i$  is the particle charge, and  $E_e$  is the first electronic excitation energy (13.6 eV). The excitation of the electronic levels releases energy quite uniformly inside a volume of a sphere of critical radius, and the distance between successive excited molecules will be less than the molecular mean free path. The nucleation process can be affected by the thermal motion since the growing bubble can break apart and collapse because of the random movement of molecules over the nucleation region. As shown in Eq. (22), the probability that a particle will eject a high-energy electron decreases with its energy. For very high energy particles, the probability of ejecting an electron drops to practically zero while the excitation of the electronic levels becomes the main mechanism for energy loss.<sup>18</sup> Consequently, even for small critical radii, nucleation is possible for energies of the incident particles within the MeV range.

The probability of bubble generation for a recoil nucleus can be estimated from the ratio of the cross section for the first electronic-level excitation energy to the cross section of a critical radius bubble (as in this case where the energy is transmitted through the excitation of the electronic levels) and the nuclear recoil distance. The cross section for the first electronic-level excitation energy is difficult to estimate. It can be approximated using Eq. (26) to calculate the cross section to generate energies higher than the excitation level and subtracting from it the cross section for energies close to the  $E_b$  value (the energy necessary to create a bubble), which will generate more-energetic electrons that produce ionization in the medium and induce nucleation. Based on this approximation, the following equation provides a general estimate for the number of bubbles created by a recoil ion rather than an exact value:

$$N_{\text{ieex}} = \eta \left( \frac{\sigma_{\text{ex}} - \sigma_{\text{eject}}}{\pi R_c^2} \cdot n_{i,n} \right)^{\frac{E_b}{E_e}} \cdot \frac{r_d}{2R_c}, \quad (27)$$

where  $\eta$  is a correction coefficient that depends on the thermal influence for the bubble formation and must be determined experimentally,  $\sigma_{\text{ex}}$  is the cross section for a recoil ion to transmit the excitation energy  $E_e$  to an electron,  $\sigma_{\text{eject}}$  is the cross section for a recoil ion to eject an electron,  $R_c$  is the critical radius,  $E_e$  is the first electronic excitation energy,  $n_{i,n}$  is the average number of interactions for which an electron of energy  $E_e$  is generated,  $E_b$  is the energy necessary to create a bubble, and  $r_d$  is the recoil ion range.

Adapting the calculations to a neutron detector, the bubble chamber's sensitivity to neutrons can be expressed as

$$\begin{aligned} \frac{N_{\text{bubbles}}}{n_{\text{source}}} &= F_n F_{\text{ex}} N_{\text{ieex}} d\Omega \\ &= F_n F_{\text{ex}} \eta \left( \frac{\sigma_{\text{ex}} - \sigma_{\text{eject}}}{\sigma R_c} \cdot n_{i,n} \right)^{\frac{E_b}{E_e}} \cdot \frac{r_d}{2R_c} d\Omega, \end{aligned} \quad (28)$$

where  $F_n$  is the fraction of the incident neutrons interacting with the active medium,  $F_{\text{ex}}$  is the fraction of carbon nuclei that can generate bubbles by exciting the electronic systems of the active medium,  $\eta$  is a thermal coefficient that must be determined experimentally, and  $d\Omega$  is the detector's solid angle. With the exception of  $\eta$ , all of the factors can be estimated from theoretical calculations.

### Calculation of the Thermal Coefficient $\eta$ Based on Data from a Freon 115 Bubble Chamber Used at CERN

Bubble tracks were recorded by a Freon 115 detector designed and built at CERN in 1981.<sup>28</sup> The nucleations were generated by incident 360-GeV/c protons inside an externally induced magnetic field. The recorded bubble density along the charged-particle tracks was in the range of 160 bubbles/cm at 50°C, decreasing with temperature. Based on the SRIM simulations, the stopping power for charged particles decreases with increasing energy. For protons, it reaches a minimum of 0.2 MeV/mm at 2.75 GeV and increases slowly, reaching 0.3 MeV/mm at energies over 100 GeV/c (Ref. 29). For the operating conditions of the CERN bubble chamber, the pressure difference was in the range of 10 bar, with a critical bubble radius  $R_c = 4.3$  nm at 50°C and  $R_c = 2.6$  nm at 60°C. At high energies, the only possible interactions are those that excite the electronic levels (the interaction time is very short), and the interaction efficiency is close to 1. Equation (21) for the number of bubbles generated by a recoil ion can be rewritten as

$$N_i = \frac{r_d}{2R_c} \cdot \left( \frac{L_i}{L_b} \right)^3, \quad (29)$$

where  $r_d$  is the ion recoil distance,  $R_c$  is the critical bubble radius,  $L_b$  is the minimum energy loss/distance to create a bubble, and  $L_i$  is the energy loss/distance for the recoil ion. Using Eq. (29) the linear bubble density should be 429 bubbles/cm at 50°C and 155 bubbles/cm at 60°C.

The qualitative explanation is that the very small bubble radius and the thermal motion inside the liquid may disrupt and prevent the bubbles from nucleating. Using the data provided by Okada *et al.*,<sup>20</sup> describing the dependence of the Freon surface tension for Freon 115 as a function of temperature and

knowing the pressure drop during the chamber decompression, the critical radius for the bubble formation can be calculated using Eq. (3). Correlating the bubble's critical radius with the observed number of bubbles, a linear dependence of  $\eta$  with critical bubble radius was determined, as shown in Fig. 121.43. The  $\eta$  factor explains the discrepancies between the calculated and experimentally measured values.

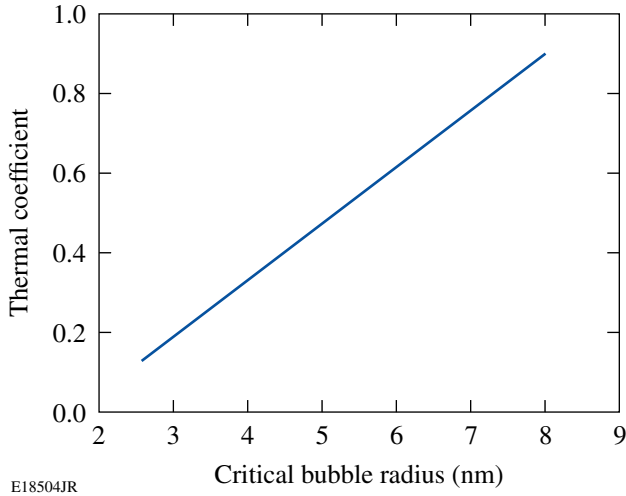


Figure 121.43  
The thermal coefficient as a function of the critical bubble radius inside Freon 115.

For the experimental conditions encountered on OMEGA, the critical radius was in the range of 7 nm, so the thermal coefficient has a value of  $\eta = 0.75$ . In conclusion, the thermal motion affects bubble formation even for the mechanism of bubble formation involving the excitation of the electronic levels, and the bubble density decreases linearly with the increasing temperature.

### Numerical Estimate for the Number of Nucleations Generated by 14.1-MeV Incident Neutrons Inside Freon 115

For Freon 115, the value of  $E_{\text{ex}}$  is 1.8 MeV for carbon, 4.2 MeV for fluorine, and 15.9 MeV for chlorine. Based on the recoil ion energies achieved from the elastic interactions with the incident 14.1-MeV neutrons, the maximum recoil energy is 4 MeV for carbon, 2.7 MeV for fluorine, and 1.5 MeV for chlorine. Equation (26) indicates that only the carbon recoil nuclei (ions) may have enough energy to generate nucleation inside Freon 115 by exciting the electronic system of the active medium molecules. The carbon recoil nuclei have an energy of 1.8 MeV or greater at a scattering angle of  $50^\circ$ .

Using the differential cross section for 14.1-MeV neutron elastic scattering on carbon shown in Fig. 121.44,<sup>30</sup> the fraction of carbon nuclei that can generate bubbles,  $F_{\text{ex}}$ , through the mechanism of exciting the electronic systems of the active medium can be estimated to be about 10% of the nuclei with which the incident 14.1-MeV neutrons interact.

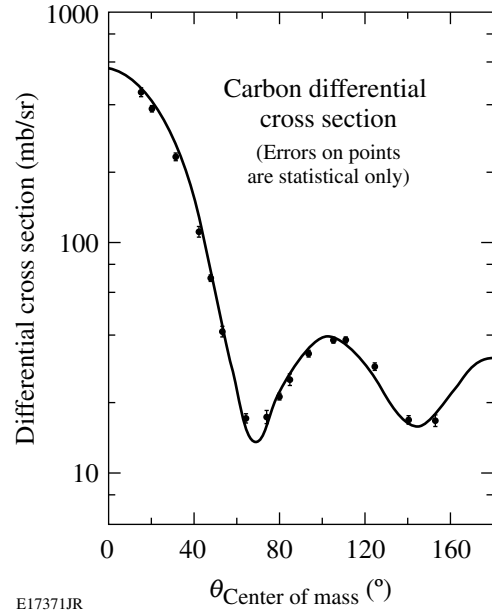


Figure 121.44  
The differential cross section for 14-MeV neutron elastic scattering on carbon. About 98% of the recoil ions have energies greater than the threshold energy  $E_b$  necessary to generate a bubble (from Ref. 27).

The neutron-carbon cross section  $F_C$  represents 53% of the total cross section of Freon 115. Multiplying this value by  $F_n$ , one obtains the fraction of the incident neutrons interacting with the active medium that can theoretically generate bubbles inside Freon 115.

Based on Freon 115's density ( $1.15 \text{ g/cm}^3$ ) and molecular mass ( $M = 154.5$  atomic units), the concentration of Freon molecules per  $\text{cm}^3$  is  $N_f = 4.99 \times 10^{21}$ . This gives an average distance between molecules of  $d_{\text{mol}} = 5.8 \times 10^{-8} \text{ cm}$  and a cross section for the volume occupied by a molecule of  $\sigma_{\text{mol}} = 2.689 \times 10^{-15} \text{ cm}^2$  from Eq. (29).

The value of  $d_{\text{mol}}$  is used to estimate the factor

$$\left( \frac{\sigma_{\text{ex}} - \sigma_{\text{eject}}}{\sigma R_c} \cdot n_{i,n} \right)^{\frac{E_b}{E_e}} \approx 6.4 \times 10^{-8}.$$

The average recoil distance for carbon at energies between 1.8 MeV and 4 MeV is around  $7 \mu\text{m}$  and  $r_d/2R_c \approx 500$ . With the thermal coefficient  $\eta = 0.75$ , the number of bubbles generated by a neutron that interacts with the medium and shape equivalent to that of the prototype detector used for neutron detection on OMEGA is

$$\frac{N_{\text{bubbles}}}{n_{\text{interact}}} = F_C F_{\text{ex}} N_{\text{icx}} = 5.8 \times 10^{-6}. \quad (30)$$

The detector is a 3.5-cm-diam, 10-cm-long cylinder. As specified in the previous section, the total cross section for the 14-MeV neutrons scattering on Freon is  $S_t = 4.8$  barn (the Freon molecular mass is  $M_{\text{Fr}} = 154.5$  atm). By knowing the active medium density, one can calculate the total cross section of the liquid. Freon has a density of  $1.15 \text{ g/cm}^3$  at  $50^\circ\text{C}$ , so the corresponding mass for the volume is  $m_f = 110$  g. As already shown, the fraction of the neutrons interacting with the Freon inside the detector is  $\approx 0.22$  and the solid angle of the detector is  $d\Omega = 1.2 \times 10^{-6}$ .

Substituting these values in Eq. (28), one obtains the estimated number of bubbles per source neutron  $N_{\text{bubbles}}/n_{\text{source}} = 1.5 \times 10^{-12}$  or for the number of bubbles expected to be observed inside the detector,  $N_{\text{det}} \approx 15$  for a neutron yield of  $10^{13}$ . This low value for the number of bubbles created inside Freon 115 indicates that the Freon bubble chamber is not sensitive enough for neutron imaging for the yields achieved on OMEGA but may be appropriate for the higher yields produced at the NIF, where the neutron yield is expected to approach  $10^{19}$ . These calculations were tested against experimental measurements with a Freon 115 bubble chamber. The experimentally observed values of  $N_{\text{meas}} \approx 11$  to 14 bubbles agreed with these theoretically calculated values.<sup>10</sup> If it were possible to use a liquid bubble chamber with Freon 115 at room temperature, the critical radius described by Eq. (4) would increase to  $\sim 20$  nm and the ejected electrons would become dominant for bubble formation, as described previously. The number of observed bubbles should reach much higher values when calculated by Eq. (30) ( $\sim 10^6$  bubbles). Unfortunately, for temperatures lower than  $48^\circ\text{C}$ , foaming occurs inside Freon 115 before any useful data can be recorded.<sup>11</sup>

### Numerical Estimate for the Number of Nucleations Generated by 14.1-MeV Incident Neutrons Inside a Gel Detector

Freon gel detectors were used to record 14.1-MeV neutrons on OMEGA in 2001.<sup>8</sup> Disk-shaped gel bubble detectors,

8.5 cm in diameter and 1 cm thick, were installed behind the penumbral neutron aperture and close to the outside edge of the OMEGA target chamber. The detectors consisted of  $10^5$  droplets, approximately  $3 \mu\text{m}$  in diameter, of a superheated liquid (Freon) suspended in an elastic polymer matrix support gel.<sup>8</sup> The gel material has no effect on bubble generation.<sup>31</sup> The neutron-imaging system's aperture was biconical, with a 0.75-mm inner diameter. The target-to-detector distance was 362 cm and the target-to-aperture distance was 8 cm, with a system magnification  $M \approx 45$  (Ref. 8). The neutron yield was  $6 \times 10^{13}$  (Ref. 8).

Depending on the Freon type used, the calculated critical radius  $R_c$  at  $22^\circ\text{C}$  to  $23^\circ\text{C}$  can range from 20 nm to 40 nm with the energy necessary to create a bubble in the range of 1 keV to 5 keV. At these energies, the mean free path of the electrons ejected by the recoil nuclei inside the gas is about 20 nm to 40 nm, and the distance between two consecutive ejected electrons is shorter than the molecular mean free path of 1 nm to 3 nm, filling the critical bubble volume continuously with heat spikes resulting from the subsequent recombination of ions and electrons. As a result, the heat is released in a volume comparable to the volume of the critical radius for bubble formation  $R_c$ , the mechanism of bubble creation is valid, and Eq. (24) can be used.

The stopping power calculated for the recoil ions generated by incident 14.1-MeV neutrons inside Freon using the SRIM software is in the range of 400 MeV/mm, while the energy necessary to create a bubble along the particle trajectory is significantly lower, at 50 to 90 MeV/mm. On the molecular scale, most of the recoil ions (nuclei) will generate many electrons that can fill a critical bubble volume with enough energy to induce nucleation along its path. Since the ions have recoil ranges up to  $9 \mu\text{m}$  (with an average value of  $2 \mu\text{m}$ ), they will create a continuous track of bubbles that will grow rapidly and fuse into larger bubbles. These bubbles will fill the  $3\text{-}\mu\text{m}$  superheated droplets and can be recorded.

The neutron-Freon interaction cross section is in the range of 4.2 barn for both Freon 12 and Freon 22. Using a similar calculation as for Freon 115, the neutron-detection efficiency per source neutron is estimated to be 0.021 for the 1-cm-thick gel detector, assuming it is filled entirely with Freon. Since only 0.1% of the detector's volume is actually filled with Freon, the detection efficiency is

$$\frac{N_{\text{bubbles}}}{n_{\text{source}}} = 2.1 \times 10^{-5} d\Omega. \quad (31)$$

Based on the geometry of the imaging system, the radius of the central maximum at the detector is  $r \approx 3$  cm. The number of neutrons reaching the detector can be calculated using the formula

$$N_i = \frac{y \cdot r^2}{4 \cdot R^2}, \quad (32)$$

where  $y$  is the neutron yield,  $r$  is the radius of the detector, and  $R$  is the distance between the neutron source and detector. Inserting the numerical values into Eq. (32), the number of the neutrons entering the Freon medium is  $N_i = 2.6 \times 10^8$ . The solid angle of the detector is  $d\Omega = 4.3 \times 10^{-6}$ . Multiplying  $N_i$  by the neutron-detection efficiency per source neutron, the estimated number of bubbles inside the central maximum area is

$$N_{\text{bubbles}} = N_i \cdot \frac{N_{\text{bubbles}}}{n_{\text{source}}} = 5.4 \times 10^3. \quad (33)$$

The testing of gel detectors on OMEGA in 2001 measured  $5.3 \times 10^3$  bubbles.<sup>8</sup>

## Conclusions

Based on the classical mechanism of bubble formation, the interaction between an incident neutron and the sensitive medium inside a bubble takes place in three steps: first, the medium nuclei are elastically scattered; second, the scattered nuclei generate free electrons; and, third, the free electrons recombine with the ions over a quasi-spherical volume to generate bubbles.

The efficiency of nucleation depends on both the size of the critical radius and the medium temperature. For some particular cases, as in the use of Freon 115 on OMEGA, the critical radius is shown to be too small for bubble generation through the mechanism of free electron-ion recombination. Some bubbles are generated, however, through the excitation of electronic levels by charged incident particles at relatively high energies (MeV range).

For a bubble chamber used on OMEGA, the estimated number of bubbles per source neutron is calculated to be  $N_{\text{bubbles}}/n_{\text{source}} = 1.5 \times 10^{-12}$ , or for the number of bubbles observed inside the detector (after subtracting the turbulence area), the expected value is  $N_{\text{det}} \approx 15$ . These values agree with the experimentally recorded  $N_{\text{meas}} \approx 11$  to 14 bubbles on OMEGA.<sup>10</sup> The expected number of bubbles for the experi-

mental conditions encountered on OMEGA is insufficient for neutron imaging, but the higher yields from the NIF will be able to create a high-enough bubble density for a useful diagnostic tool, provided a similar but improved system is used.

Because of the lower temperature and larger (20-nm) critical radius, a simplified model of bubble formation that does not take into account the size of the critical radius gives accurate results for gel detectors. The numerical predictions of this model agree with the results obtained on OMEGA in 2001.<sup>8</sup>

## ACKNOWLEDGMENT

This work was supported by the U.S. Department of Energy Office of Inertial Confinement Fusion under Cooperative Agreement No. DE-FC52-08NA28302, the University of Rochester, and the New York State Energy Research and Development Authority. The support of DOE does not constitute an endorsement by DOE of the views expressed in this article.

## REFERENCES

1. S. Pfalzner, *An Introduction to Inertial Confinement Fusion* (Taylor & Francis, New York, 2006).
2. T. J. Murphy, C. W. Barnes, R. R. Berggren, P. Bradley, S. E. Caldwell, R. E. Chrien, J. R. Faulkner, P. L. Gobby, N. M. Hoffman, J. L. Jimerson, K. A. Klare, C. L. Lee, J. M. Mack, G. L. Morgan, J. A. Oertel, F. J. Swenson, P. J. Walsh, R. B. Walton, R. G. Watt, M. D. Wilke, D. C. Wilson, C. S. Young, S. W. Haan, R. A. Lerche, M. J. Moran, T. W. Phillips, T. C. Sangster, R. J. Leeper, C. L. Ruiz, G. W. Cooper, L. Disdier, A. Rouyer, A. Fedotoff, V. Yu. Glebov, D. D. Meyerhofer, J. M. Soares, C. Stockl, J. A. Frenje, D. G. Hicks, C. K. Li, R. D. Petrasso, F. H. Séguin, K. Fletcher, S. Padalino, and R. K. Fisher, *Rev. Sci. Instrum.* **72**, 773 (2001).
3. D. Ress *et al.*, *Science* **241**, 956 (1988).
4. L. Disdier, A. Rouyer, I. Lantuéjoul, O. Landoas, J. L. Bourgade, T. C. Sangster, V. Yu. Glebov, and R. A. Lerche, *Phys. Plasmas* **13**, 056317 (2006).
5. T. R. Boehly, D. L. Brown, R. S. Craxton, R. L. Keck, J. P. Knauer, J. H. Kelly, T. J. Kessler, S. A. Kumpan, S. J. Loucks, S. A. Letzring, F. J. Marshall, R. L. McCrory, S. F. B. Morse, W. Seka, J. M. Soares, and C. P. Verdon, *Opt. Commun.* **133**, 495 (1997).
6. L. Disdier, A. Rouyer, A. Fedotoff, J.-L. Bourgade, F. J. Marshall, V. Yu. Glebov, and C. Stoeckl, *Rev. Sci. Instrum.* **74**, 1832 (2003).
7. M. C. Ghilea, T. C. Sangster, D. D. Meyerhofer, R. A. Lerche, and L. Disdier, *Rev. Sci. Instrum.* **79**, 023501 (2008).
8. R. K. Fisher, R. B. Stephens, L. Disdier, J. L. Bourgade, A. Rouyer, P. A. Jaanimagi, T. C. Sangster, R. A. Lerche, and N. Izumi, *Phys. Plasmas* **9**, 2182 (2002).
9. M. C. Ghilea, D. D. Meyerhofer, and T. C. Sangster, "A Freon-Filled Bubble Chamber for Neutron Detection in Inertial Confinement Fusion Experiments," to be submitted to *Review of Scientific Instruments*.

10. M. C. Ghilea, D. D. Meyerhofer, and T. C. Sangster, "Neutron Detection with Bubble Chambers for Inertial Confinement Fusion on OMEGA," to be submitted to Review of Scientific Instruments.
11. A. Herve *et al.*, Nucl. Instrum. Methods Phys. Res. **202**, 417 (1982).
12. M. Das *et al.*, Radiat. Meas. **30**, 35 (1999).
13. J. W. Gibbs, Connecticut Academy Transactions **3**, 108 (1875-7).
14. L. K. Pan, J. Radioanal. Nucl. Chem. **240**, 707 (1999).
15. C. R. Bell *et al.*, Nucl. Sci. Eng. **53**, 458 (1974).
16. A. Norman and P. Spiegler, Nucl. Sci. Eng. **16**, 213 (1963).
17. C. R. Bell, "Radiation Induced Nucleation of the Vapor Phase," Ph.D. thesis, Massachusetts Institute of Technology, 1970.
18. F. Seitz, Phys. Fluids **1**, 2 (1958).
19. R. E. Apfel and S. C. Roy, Radiat. Prot. Dosim. **10**, 327 (1985).
20. M. Okada *et al.*, J. Chem. Eng. Data **33**, 399 (1988).
21. R. K. Fisher *et al.*, Rev. Sci. Instrum. **72**, 796 (2001).
22. J. Benichou *et al.*, Nucl. Instrum. Methods Phys. Res. **214**, 245 (1983).
23. D. V. Bugg, in *Progress in Nuclear Physics* (Butterworths-Springer, London, 1959), Vol. 7, pp. 1-52.
24. M. S. Plesset and S. A. Zwick, J. Appl. Phys. **25**, 493 (1954).
25. D. Hughes and R. Schwartz, *Neutron Cross Sections*, 2nd. ed (Brookhaven National Laboratory, Upton, NY, 1958).
26. H. A. Bethe and J. Ashkin, in *Experimental Nuclear Physics*, edited by E. Sergrè (Wiley, New York, 1953), Vol. I, pp. 166-357.
27. W. Benenson *et al.*, eds. *Handbook of Physics* (Springer, New York, 2002).
28. M. Dykes *et al.*, Nucl. Instrum. Methods **179**, 487 (1981).
29. H. Tai, *Comparison of Stopping Power and Range Databases for Radiation Transport Study*, NASA Technical Paper (National Aeronautics and Space Administration, Langley Research Center, Hampton, VA, 1997).
30. A. J. Frasca *et al.*, Phys. Rev. **144**, 854 (1966).
31. T. P. Pandya, A. K. Saxena, and B. C. Srivastava, Rev. Sci. Instrum. **47**, 1299 (1976).



---

## Publications and Conference Presentations

---

### Publications

---

- G. P. Cox, K. L. Marshall, J. C. Lambropoulos, M. Leitch, C. Fromen, and S. D. Jacobs, "Modeling the Effects of Microencapsulation on the Electro-Optic Behavior of Polymer Cholesteric Liquid Crystal Flakes," *J. Appl. Phys.* **106**, 124911 (2009).
- A. S. Cross, D. Kochanowska, M. Witkowska-Baran, A. Mycielski, M. Mikulics, D. Grützmacher, and R. Sobolewski, "Femtosecond Electro-Optic Effect in (Cd,Mn)Te Single Crystals," *J. Phys. Conf. Series* **193**, 012057 (2009).
- D. French, C. Dorrer, and I. Jovanovic, "Two-Beam SPIDER for Dual-Pulse Single-Shot Characterization," *Opt. Lett.* **34**, 3415 (2009).
- E. Glowacki, C. W. Tang, and K. L. Marshall, "Photoswitchable Gas Permeation Membranes Based on Azobenzene-Doped Liquid Crystals," in *Liquid Crystals XIII*, edited by I. C. Khoo (SPIE, Bellingham, WA, 2009), Vol. 7414, p. 74140H (invited).
- O. V. Gotchev, P. Y. Chang, J. P. Knauer, D. D. Meyerhofer, O. Polomarov, J. Frenje, C. K. Li, M. J.-E. Manuel, R. D. Petrasso, J. R. Rygg, F. H. Séguin, and R. Betti, "Laser-Driven Magnetic-Flux Compression in High-Energy-Density Plasmas," *Phys. Rev. Lett.* **103**, 215004 (2009).
- W. Guan and J. R. Marciante, "Single-Frequency 1 W Hybrid Brillouin/Ytterbium Fiber Laser," *Opt. Lett.* **34**, 3131 (2009).
- S. X. Hu, P. B. Radha, J. A. Marozas, R. Betti, T. J. B. Collins, R. S. Craxton, J. A. Delettrez, D. H. Edgell, R. Epstein, V. N. Goncharov, I. V. Igumenshchev, F. J. Marshall, R. L. McCrory, D. D. Meyerhofer, S. P. Regan, T. C. Sangster, S. Skupsky, V. A. Smalyuk, Y. Elbaz, and D. Shvarts, "Neutron Yield Study of Direct-Drive, Low-Adiabatic Cryogenic D<sub>2</sub> Implosions on OMEGA Laser System," *Phys. Plasmas* **16**, 112706 (2009).
- H. Irie and R. Sobolewski, "Picosecond Electric Pulse Excitation of Three-Branch Ballistic Nanodevices," *J. Phys. Conf. Series* **193**, 012097 (2009).
- V. Kaushal, M. Margala, Q. Yu, P. Ampadu, G. Guarino, and R. Sobolewski, "Current Transport Modeling and Experimental Study of THz Room Temperature Ballistic Deflection Transistors," *J. Phys. Conf. Series* **193**, 012092 (2009).
- C. Miao, J. C. Lambropoulos, H. Romanofsky, S. N. Shafrir, and S. D. Jacobs, "Contributions of Nanodiamond Abrasives and Deionized Water in Magnetorheological Finishing of Aluminum Oxynitride," in *Optical Manufacturing and Testing VIII*, edited by J. H. Burge, O. W. Föhnle, and R. Williamson (SPIE, Bellingham, WA, 2009), Vol. 7426, p. 74260D.
- C. Miao, S. N. Shafrir, J. C. Lambropoulos, and S. D. Jacobs, "Normal Force and Drag Force in Magnetorheological Finishing," in *Optical Manufacturing and Testing VIII*, edited by J. H. Burge, O. W. Föhnle, and R. Williamson (SPIE, Bellingham, WA, 2009), Vol. 7426, p. 74260C.
- P. M. Nilson, S. P. D. Mangles, L. Willingale, M. C. Kaluza, A. G. R. Thomas, M. Tatarakis, Z. Najmudin, R. J. Clarke, K. L. Lancaster, S. Karsch, J. Schreiber, R. G. Evans, A. E. Dangor, and K. Krushelnick, "Generation of Ultrahigh-Velocity Ionizing Shocks with Petawatt-Class Laser Pulses," *Phys. Rev. Lett.* **103**, 255001 (2009).
- P. M. Nilson, W. Theobald, J. F. Myatt, C. Stoeckl, J. D. Zuegel, R. Betti, D. D. Meyerhofer, and T. C. Sangster, "X-Ray Spectroscopy of Solid-Density Plasmas in High-Intensity Laser Interactions," in *Atomic Processes in Plasmas*, edited by K. B. Fournier (American Institute of Physics, New York, NY, 2009), Vol. CP1161, pp. 17–23.

G. P. Pepe, L. Parlato, N. Marrocco, V. Pagliarulo, G. Peluso, A. Barone, F. Tafuri, U. Scotti di Uccio, F. Miletto, M. Radovic, D. Pan, and R. Sobolewski, "Novel Superconducting Proximized Heterostructures for Ultrafast Photodetection," *Cryogenics* **49**, 660 (2009).

S. P. Regan, B. Yaakobi, T. R. Boehly, R. Epstein, J. A. Delettrez, V. Yu. Glebov, V. N. Goncharov, P. A. Jaanimagi, J. P. Knauer, F. J. Marshall, R. L. McCrory, D. D. Meyerhofer, P. B. Radha, T. C. Sangster, V. A. Smalyuk, J. Soures, C. Stoeckl, R. C. Mancini, D. A. Haynes, Jr., L. Welser-Sherrill, J. A. Koch, R. Tommasini, and H. Sawada, "Applied Plasma Spectroscopy: Laser-Fusion Experiments," *High Energy Density Phys.* **5**, 234 (2009).

S. N. Shafrir, H. J. Romanofsky, M. Skarlinski, M. Wang, C. Miao, S. Salzman, T. Chartier, J. Mici, J. C. Lambropoulos, R. Shen, H. Yang, and S. D. Jacobs, "Zirconia Coated Carbonyl Iron Particle-Based Magnetorheological Fluid for Polishing," in *Optical Manufacturing and Testing VIII*, edited by J. H. Burge, O. W. Föhnle, and R. Williamson (SPIE, Bellingham, WA, 2009), Vol. 7426, p. 74260B.

S. N. Shafrir, H. J. Romanofsky, M. Skarlinski, M. Wang, C. Miao, S. Salzman, T. Chartier, J. Mici, J. C. Lambropoulos, R. Shen, H. Yang, and S. D. Jacobs, "Zirconia-Coated Carbonyl-Iron-Particle-Based Magnetorheological Fluid for Polishing Optical Glasses and Ceramics," *Appl. Opt.* **48**, 6797 (2009).

V. A. Smalyuk, S. X. Hu, J. D. Hager, J. A. Delettrez, D. D. Meyerhofer, T. C. Sangster, and D. Shvarts, "Spherical Rayleigh–Taylor Growth of Three-Dimensional Broadband Perturbations on OMEGA," *Phys. Plasmas* **16**, 112701 (2009).

W. Theobald, K. S. Anderson, R. Betti, R. S. Craxton, J. A. Delettrez, J. A. Frenje, V. Yu. Glebov, O. V. Gotchev, J. H. Kelly, C. K. Li, A. J. Mackinnon, F. J. Marshall, R. L. McCrory, D. D. Meyerhofer, J. F. Myatt, P. A. Norreys, P. M. Nilson, P. K. Patel, R. D. Petrasso, P. B. Radha, C. Ren, T. C. Sangster, W. Seka, V. A. Smalyuk, A. A. Solodov, R. B. Stephens, C. Stoeckl, and B. Yaakobi, "Advanced-Ignition-Concept Exploration on OMEGA," *Plasma Phys. Control. Fusion* **51**, 124052 (2009).

B. Yaakobi, O. V. Gotchev, R. Betti, and C. Stoeckl, "Study of Fast-Electron Transport in Laser-Illuminated Spherical Targets," *Phys. Plasmas* **16**, 102703 (2009).

L. Zeng, T. Y.-H. Lee, P. B. Merkel, and S. H. Chen, "A New Class of Non-Conjugated Bipolar Hybrid Hosts for Phosphorescent Organic Light-Emitting Diodes," *J. Mater. Chem.* **19**, 8772 (2009).

J. Zhang, A. Belousov, J. Karpinski, B. Batlogg, and R. Sobolewski, "Femtosecond Optical Spectroscopy Studies of High-Pressure-Grown (Al,Ga)N Single Crystals," *J. Phys. Conf. Series* **193**, 012058 (2009).

### Forthcoming Publications

J. Bromage, C. Dorrer, J. R. Marciante, M. J. Shoup III, and J. D. Zuegel, "Modal Measurement of a Large-Mode-Area Photonic-Crystal Fiber Amplifier Using Spatially Resolved Spectral Interferometry," to be published in *Solid State Diode Laser Technology Review*.

W. R. Donaldson, J. R. Marciante, and R. G. Roides, "An Optical Replicator for Single-Shot Measurements at 10 GHz with a Dynamic Range of 1800:1," to be published in the *IEEE Journal of Quantum Electronics*.

R. Florido, R. C. Mancini, T. Nagayama, R. Tommasini, J. A. Delettrez, S. P. Regan, V. A. Smalyuk, R. Rodríguez, and J. M. Gil, "Argon *K*-Shell and Bound-Free Emission from OMEGA Direct-Drive Implosion Cores," to be published in *High Energy Density Physics*.

W. Guan and J. R. Marciante, "Power Scaling of Single-Frequency Hybrid Brillouin/Ytterbium Fiber Lasers," to be published in *IEEE Journal of Quantum Electronics*.

J. Kitaygorsky, R. Shouten, S. Dorenbos, E. Reiger, V. Zwiller, and R. Sobolewski, "Resolving Dark Pulses from Photon Pulses in NbN Superconducting Single-Photon Detectors," to be published in the *Journal of Modern Optics*.

P. W. McKenty, R. S. Craxton, F. J. Marshall, T. C. Sangster, J. A. Marozas, A. M. Cok, M. J. Bonino, D. R. Harding, D. D. Meyerhofer, R. L. McCrory, J. D. Kilkenny, A. Nikroo, J. Fooks, M. Hoppe, J. M. Edwards, A. J. MacKinnon, D. H. Munro, and R. J. Wallace, "Design of High-Neutron-Yield Polar-Drive Targets for Diagnostic Activation Experiments on the NIF," to be published in the *Journal of Physics: Conference Series*.

A. V. Okishev, "Optical Differentiation and Multimillijoule ~150-ps Pulse Generation in a Regenerative Amplifier with a Temperature-Tuned Intracavity Volume Bragg Grating," to be published in *Applied Optics*.

H. F. Robey, T. R. Boehly, R. E. Olson, A. Nikroo, P. M. Celliers, O. L. Landen, and D. D. Meyerhofer, "Experimental Validation of a Diagnostic Technique for Tuning the Fourth Shock Timing on National Ignition Facility," to be published in *Physics of Plasmas*.

J. E. Schoenly, W. Seka, and P. Rechmann, "Investigation into the Optimum Beam Shape and Fluence for Selective Ablation of Dental Calculus at  $\lambda = 400$  nm," to be published in *Lasers in Surgery and Medicine*.

R. Shen, S. N. Shafir, C. Miao, M. Wang, J. C. Lambropoulos, S. D. Jacobs, and H. Yang, "Synthesis and Corrosion Study of Zirconia Coated Carbonyl Iron Particles," to be published in the *Journal of Colloid and Interface Science*.

L. Sun, S. Jiang, and J. R. Marciante, "All-Fiber Optical Magnetic-Field Sensor Based on Faraday Rotation in Highly Terbium-Doped Fiber," to be published in *Optics Express*.

L. Sun, S. Jiang, J. D. Zuegel, and J. R. Marciante, "All-Fiber Optical Isolator Based on Faraday Rotation in Highly Terbium-Doped Fiber," to be published in *Optics Letters*.

---

### Conference Presentations

---

The following presentations were made at *Frontiers in Optics 2009*, San Jose, CA, 11–15 October 2009:

W. Guan and J. R. Marciante, "Power Scaling of Single-Frequency Hybrid Brillouin/Ytterbium Fiber Lasers."

J. R. Marciante, "Spatial-Filtering Properties of Large-Mode-Area Fibers with Confined Gain Dopants."

L. Sun, S. Jiang, J. D. Zuegel, and J. R. Marciante, "All-Fiber Isolator Based on Faraday Rotation."

---

C. Dorrer, "Signal Reconstruction Techniques for Optical Pulse Characterization," *Signal Recovery and Synthesis*, San Jose, CA, 13–14 October 2009.

---

The following presentations were made at the 51st Annual Meeting of the APS Division of Plasma Physics, Atlanta, GA, 2–6 November 2009:

K. S. Anderson, R. Betti, P. Y. Chang, R. Nora, M. Fatenejad, and D. Shvarts, "Single- and Multidimensional Robustness Studies of the NIF Ignition Point Design."

M. A. Barrios, D. G. Hicks, T. R. Boehly, D. E. Fratanduono, J. H. Eggert, P. M. Celliers, G. W. Collins, and D. D. Meyerhofer, "High-Precision Measurements of the Equation of State (EOS) of Hydrocarbons at 1 to 10 Mbar Using Laser-Driven Shock Waves" (invited).

R. Betti, K. S. Anderson, P. Y. Chang, R. Nora, C. D. Zhou, B. Spears, J. Edwards, S. W. Haan, and J. Lindl, "ICF Ignition, the Lawson Criterion, and Comparison with MFE Ignition" (invited).

T. R. Boehly, V. N. Goncharov, W. Seka, D. E. Fratanduono, M. A. Barrios, S. X. Hu, J. A. Marozas, T. C. Sangster, D. D. Meyerhofer, D. G. Hicks, and P. M. Celliers, "Shock-Timing Measurements in Directly Driven Spherical Inertial Confinement Fusion Targets."

P. Y. Chang, R. Betti, K. S. Anderson, R. Nora, B. Spears, M. Fatenejad, and D. Shvarts, "A Measurable Three-Dimensional Ignition Criterion for Inertial Confinement Fusion."

T. J. B. Collins, P. W. McKenty, K. S. Anderson, M. M. Marinak, M. A. Barrios, D. G. Braun, T. R. Boehly, and P. M. Celliers, "Simulations of the Direct-Drive NIF Shock-Timing Diagnostic Commissioning Experiments."

R. S. Craxton, W. Theobald, W. Seka, S. Ivancic, G. Li, C. Ren, and D. Weiner, "Hydrodynamic Simulations and Optical

Diagnosis of a Long-Scale-Length Channeling Experiment on OMEGA EP.”

J. A. Delettrez, J. P. Knauer, V. N. Goncharov, P. B. Radha, C. Stoeckl, A. V. Maximov, J. A. Frenje, and D. Shvarts, “Analysis of the Effect of a High-Z-Doped CH Ablator and Glass Ablators on Preheat and Hard X-Ray Radiation from Two-Plasmon Decay Electrons.”

D. H. Edgell, W. Seka, J. A. Delettrez, R. S. Craxton, V. N. Goncharov, I. V. Igumenshchev, J. F. Myatt, A. V. Maximov, R. W. Short, T. C. Sangster, and R. E. Bahr, “Cross-Beam Energy Transport in Direct-Drive-Implosion Experiments.”

R. Epstein, J. A. Delettrez, V. N. Goncharov, P. W. McKenty, F. J. Marshall, D. D. Meyerhofer, P. B. Radha, S. P. Regan, T. C. Sangster, V. A. Smalyuk, and W. Theobald, “Simulation and Analysis of Backlit Images of Cryogenic Implosions on OMEGA.”

D. E. Fratanduono, M. A. Barrios, T. R. Boehly, D. D. Meyerhofer, R. Smith, J. H. Eggert, D. G. Hicks, P. M. Celliers, G. W. Collins, and R. Rygg, “Measurements of Strain-Induced Refractive Index Changes in LiF Using Direct-Drive Ramp Compression.”

V. Yu. Glebov, C. Stoeckl, W. Theobald, T. C. Sangster, K. L. Marshall, M. Cruz, M. J. Shoup III, T. Buczek, A. Pruyne, M. Fox, T. Duffy, M. J. Moran, and R. Lauck, “Development of Scintillator Detectors for Fast-Ignition Experiments and Down-Scattered Neutron Measurements.”

V. N. Goncharov, T. C. Sangster, T. R. Boehly, R. L. McCrory, D. D. Meyerhofer, P. B. Radha, V. A. Smalyuk, S. Skupsky, J. A. Frenje, and R. D. Petrasso, “Multiple-Picket Cryogenic Target Designs and Performance for OMEGA and the National Ignition Facility.”

J. D. Hager, J. P. Knauer, S. X. Hu, D. D. Meyerhofer, T. C. Sangster, and V. A. Smalyuk, “Rayleigh–Taylor Measurements in Planar CH and SiO<sub>2</sub> Foils on OMEGA.”

S. X. Hu, B. Militzer, V. N. Goncharov, T. R. Boehly, P. B. Radha, and S. Skupsky, “Theoretical Investigation of Strong Coupling and Degeneracy Effects in ICF Implosions.”

I. V. Igumenshchev, D. H. Edgell, V. N. Goncharov, W. Seka, J. F. Myatt, A. V. Maximov, A. Shvydsky, and J. A. Delettrez,

“Modeling Crossed-Beam Energy Transfer in Implosion Experiments on OMEGA.”

J. P. Knauer, O. V. Gotchev, P. Y. Chang, D. D. Meyerhofer, A. Polomarov, R. Betti, J. A. Frenje, C. K. Li, M. J.-E. Manuel, R. D. Petrasso, J. R. Rygg, and F. H. Séguin, “Compressing Magnetic Fields with High-Energy Lasers” (invited).

J. A. Marozas, T. J. B. Collins, and J. D. Zuegel, “2-D Simulations of a 1-MJ CH-Foam Ignition Target on the NIF with 0.5 THz of 1-D Multi-FM SSD Bandwidth Using an Analytic Model.”

F. J. Marshall, R. S. Craxton, R. Epstein, V. Yu. Glebov, V. N. Goncharov, J. P. Knauer, P. W. McKenty, P. B. Radha, A. Shvydsky, J. A. Frenje, C. K. Li, R. D. Petrasso, and F. H. Séguin, “Polar-Driven Implosions on OMEGA: Observations and Simulations of Low-Mode Perturbations in the Main Fuel Layer and Hot Spot.”

A. V. Maximov, J. F. Myatt, R. W. Short, W. Seka, J. A. Delettrez, and C. Stoeckl, “Growth and Saturation of Two-Plasmon-Decay Instability Driven by Crossing Laser Beams in OMEGA Plasmas.”

P. W. McKenty, R. S. Craxton, J. A. Marozas, A. M. Cok, M. J. Bonino, D. R. Harding, D. D. Meyerhofer, R. L. McCrory, J. D. Kilkenny, A. Nikroo, J. Fooks, M. L. Hoppe, M. J. Edwards, A. J. MacKinnon, D. H. Munro, and R. J. Wallace, “Design of High-Neutron-Yield, Polar-Drive Targets for Diagnostic Activation Experiments on the NIF.”

D. D. Meyerhofer, R. Betti, T. R. Boehly, J. H. Kelly, S. J. Loucks, R. L. McCrory, S. F. B. Morse, P. M. Nilson, S. P. Regan, T. C. Sangster, V. A. Smalyuk, C. Stoeckl, W. Theobald, and L. J. Waxer, “Initial Results from the OMEGA EP Laser System.”

J. F. Myatt, J. A. Delettrez, A. V. Maximov, R. W. Short, D. H. Edgell, W. Seka, D. F. DuBois, D. A. Russell, and H. X. Vu, “Extended Zakharov Modeling of Preheat Caused by the Two-Plasmon Decay Instability in Direct-Drive ICF Plasmas.”

P. M. Nilson, W. Theobald, J. F. Myatt, L. Gao, C. Stoeckl, P. A. Jaanimagi, J. A. Delettrez, B. Yaakobi, J. D. Zuegel, R. Betti, D. D. Meyerhofer, T. C. Sangster, A. J. MacKinnon, P. K. Patel, and K. Akli, “Fast-Electron Generation with Multi-kJ Pulses on OMEGA EP.”

- O. Polomarov, P. Y. Chang, O. V. Gotchev, and R. Betti, "Effects of External and Self-Generated Magnetic Fields on Laser-Driven Implosions."
- P. B. Radha, C. Stoeckl, V. N. Goncharov, J. A. Delettrez, T. C. Sangster, R. Betti, R. L. McCrory, D. D. Meyerhofer, S. P. Regan, W. Seka, D. Shvarts, S. Skupsky, and V. A. Smalyuk, "Intensity Dependence of Target Performance in Low-Adiabatic Warm Implosions on OMEGA."
- S. P. Regan, P. B. Radha, T. R. Boehly, V. N. Goncharov, R. L. McCrory, D. D. Meyerhofer, T. C. Sangster, V. A. Smalyuk, K. Falk, G. Gregori, T. Doeppner, S. H. Glenzer, and O. L. Landen, "Inferring Electron Temperature of Shocked Liquid Deuterium Using Inelastic X-Ray Scattering."
- T. C. Sangster, V. N. Goncharov, R. Betti, T. R. Boehly, D. T. Casey, T. J. B. Collins, R. S. Craxton, J. A. Delettrez, D. H. Edgell, R. Epstein, K. A. Fletcher, J. A. Frenje, V. Yu. Glebov, D. R. Harding, S. X. Hu, I. V. Igumenshchev, J. P. Knauer, S. J. Loucks, C. K. Li, J. A. Marozas, F. J. Marshall, R. L. McCrory, P. W. McKenty, D. D. Meyerhofer, P. M. Nilson, S. P. Padalino, R. D. Petrasso, P. B. Radha, S. P. Regan, F. H. Séguin, W. Seka, R. W. Short, D. Shvarts, S. Skupsky, V. A. Smalyuk, J. M. Soures, C. Stoeckl, W. Theobald, and B. Yaakobi, "Shock-Tuned Cryogenic DT-Implosion Performance on OMEGA" (invited).
- W. Seka, D. H. Edgell, J. F. Myatt, A. V. Maximov, R. W. Short, R. S. Craxton, D. Russell, D. F. DuBois, and H. X. Vu, "Mitigation of Fast-Electron Production by the Two-Plasmon-Decay Instability in Directly Driven Targets."
- R. W. Short, "Anisotropy and Angular Dependence of Two-Plasmon Decay Driven by Multiple Overlapping Laser Beams in Direct-Drive Geometry."
- A. Shvydky, P. W. McKenty, J. A. Delettrez, I. V. Igumenshchev, D. H. Edgell, S. Skupsky, and R. L. McCrory, "Numerical Investigation of the Effects of Cross-Beam Energy Transfer on the Drive Uniformity of OMEGA Implosions."
- A. A. Solodov, M. Storm, J. F. Myatt, R. Betti, D. D. Meyerhofer, P. M. Nilson, W. Theobald, and C. Stoeckl, "Simulations of Electron-Beam Transport in Solid-Density Targets and the Role of Magnetic Collimation."
- C. Stoeckl, W. Theobald, R. Betti, R. S. Craxton, J. A. Delettrez, O. V. Gotchev, V. Yu. Glebov, F. J. Marshall, D. D. Meyerhofer, W. Seka, T. C. Sangster, C. D. Zhou, J. A. Frenje, and R. D. Petrasso, "Shock-Ignition Experiments on OMEGA at NIF-Relevant Intensities."
- W. Theobald, C. Stoeckl, V. Yu. Glebov, F. J. Marshall, K. L. Marshall, K. S. Anderson, R. Betti, R. S. Craxton, D. D. Meyerhofer, P. M. Nilson, T. C. Sangster, A. A. Solodov, J. A. Frenje, N. Sinenian, R. D. Petrasso, P. A. Norreys, D. Hey, M. H. Key, P. K. Patel, R. Lauck, and R. B. Stephens, "Integrated Fast-Ignition Experiments on OMEGA."
- J.-H. Yang and R. S. Craxton, "An Empirical Model for the Interaction of Ultra-Intense Laser Pulses with Fully Ionized Plasmas Including Electrostatic Effects."



